Synthesis, Morphology and Luminescent Properties of Rare Earth doped Visible Up-Conversion Nanophosphors for Bio-Imaging Applications

Thesis

Submitted to

DELHI TECHNOLOGICAL UNIVERSITY

for the partial fulfillment of the requirements for the degree of

DOCTOR OF PHILOSOPHY

in

Applied Physics

by

Aman Prasad
(2K15/PhD/AP/03)

Under the joint supervision of

Prof. A.S. Rao
Department of Applied Physics
Delhi Technological University
Delhi-110042

Prof. G. Vijaya Prakash
Department of Physics
Indian Institute of Technology
New Delhi-110016

May 2020

Dedicated to the love and

hope of my family and friends

that has steered and guided me

throughout

DELHI TECHNOLOGICAL UNIVERSITY

Formerly Delhi College of Engineering

(under Delhi Act 6 of 2009, Govt. of NCT Delhi)

Shahabad Daulatpur, Main Bawana Road, Delhi- 110042

CERTIFICATE

This is to certify that the work, embodied in the thesis entitled *"***Synthesis, Morphology and Luminescent Properties of Rare Earth doped Visible Up-Conversion Nanophosphors for Bio-Imaging Applications"** done by **Aman Prasad,** Roll no. **2K15/PhD/AP/03**, as a full time Ph.D. scholar in the Department of Applied Physics, Delhi Technological University, Delhi is an authentic and bona fide work carried out by him.

This work is based on original research and the matter embodied in this thesis has not been submitted earlier for the award of any degree or diploma to the best of our knowledge and belief.

Prof. A.S. Rao

Department of Applied Physics

Delhi Technological University

Delhi- 110042

Prof. G.V. Prakash

Department of Physics

Indian Institute of Technology

New Delhi-110016

ACKNOWLEDGEMENTS

Pursuing a Ph.D. degree has been as exciting as it has been challenging. Unlike undergraduate and post-graduate courses, research is not someone's sole prerogative. It not only involves the efforts of the research scholar to carry out his work but it also demands effort, time and support of many other people and institutions alike throughout the course of this degree.

First and foremost, I would like to thank my **parents** and my **family** who have been the sole reason of my mental, physical, monetary and emotional sustenance throughput my pursuance of this degree. It is very difficult to put my thoughts into words because I owe so much to them. While writing this thesis I cannot help but remember my late grandfathers **Prof. Rajeshwar Prasad** and **Prof. Shankar Sahai Srivastava**, who, since my childhood, instilled in me a proclivity to learn and made me aspire for an impeccable academic record. I cannot thank them enough for making me imbibe such great values.

Research needs impeccable guidance and I have been fortunate enough to be under the watchful eyes of two towering personalities in the field of material sciences. I wish to thank my research supervisors, **Prof. A.S. Rao**, Department of Applied Physics, Delhi Technological University and **Prof. G.V. Prakash**, Department of Physics, Indian Institute of Technology, Delhi for laying out for me a research prospect that made me learn so much about the field of nanoscience and bio-imaging. It was a sheer privilege for me to spend so many fruitful years with them that made me delve deeper into the realms of material science, be more analytical and realise my true strengths as a young inquisitive researcher. They have made me realise that knowledge and results emanating from that go hand in hand. For inculcating this attitude in me, I am indebted towards them forever.

I wish to thank the Head of the Department, **Prof. Rinku Sharma** for always being a pillar of support during my pursuance of Ph.D. degree. I am deeply grateful to **Prof. S.C. Sharma**, Dean Academics (PG), Delhi Technological University and DRC Chairman, for his constant blessings and suggestions throughout the course of this degree. I thank **Dr. Jayasimhadri** for all the suggestions, corrections and discussions that helped me understand the subject better. I also thank **Dr. Rishu Chaujhar**, Associate Dean Academics (PG) and **Mr. Anil Kumar**, former Deputy Registrar, Academics (PG) for providing all the help and support to get me going throughout the duration of this degree. I would also like to appreciate all the help and suggestions that were given to me by the SRC and DRC members along with other faculty members of the Department of Applied Physics, Delhi Technological University. Lastly, I would also thank **Dr. Aurangzeb Khurram Hafiz**, Officiating Director, Centre for Nanoscience and Nanotechnology, Jamia Millia Islamia, New Delhi for his regular suggestions, help and guidance in the course of this research.

It would be unwise on my part to not remember all the help that was provided by all the technical and non-teaching staff in various departments of Delhi Technological University. It was their timely support and management that made the administrative journey of my degree as smooth as possible. I would like to especially thank **Mr. Vikrant**, **Mrs. Sujata**, **Mr. Krishna**, **Mrs. Babita**, **Mrs. Manisha** and **Mrs. Meena** for all their support.

An endearing research environment is a must to successfully complete the task at hand. I am glad that my fellow research scholars provided me with that ambience. It was always easy for me to ask for any help, suggestions and corrections from my colleagues throughout the course of my Ph.D. degree. With this thought in mind, I would to thank my seniors **Dr. Nisha Deopa**, **Dr. Sumandeep Kaur**, **Dr. Ritu Sharma**, **Dr. Kanika**, **Dr. Arti**, **Dr. Suman Shakya, Dr. Mohini Gupta**, **Dr. Amit Vishwakarma**, **Dr. Kaushal Jha**, **Dr. Ravi Gupta**, **Mr. Bineet Kumar** and fellow research scholars, **Mr. Rajat Bajaj**, **Ms. Umang Sharma**, **Ms. Anshu**

Dahiya, **Mr. Ankur Shandilya**, **Mr. Adnan**, **Mrs. Ravita Pilania**, **Ms. Pooja Rohilla**, **Mrs. Shristy Malik, Ms. Harpreet Kaur**, **Mr. Mukesh Sahu**, **Ms. Deepali** and **Mr. Vikas**.

Nothing successful comes without its fair share of failures and drawbacks. In such times, there are certain people who can lessen the mental fatigue and stress and subsequently guide us and take the pressure off our backs. Being true to this, I would like to thank **Mr. Harsh Singh**, **Mr. Angad Yuvraj** and **Ms. Radhika Batra** from the bottom of my heart for keeping my head at the right place when things didn't go as I wanted them to go. Your presence was a much needed relief for me.

Lastly, I would like to gratefully acknowledge the Junior Research Fellowship (JRF) and Senior Research Fellowship (SRF) provided to me by the **Department of Science and Technology (DST)**, Government of India under the **INSPIRE Programme** for carrying out this research work. Subsequently, I thank the officials and staff of **Central Research Facility (CRF)**, Indian Institute of Technology, Delhi (IIT-D), **Advanced Instrumentation Research Facility (AIRF)**, Jawaharlal Nehru University (JNU), Delhi, **Central Instrumentation Facility (CIF)**, Jamia Millia Islamia (JMI), Delhi and **Sophisticated Analytical Instrumentation Facility (SAIF)**, AIIMS, Delhi for providing access to their research facilities for characterisation of the samples.

Aman Prasad

2K15/PhD/AP/03

LIST OF FIGURES WITH PAGE NUMBER

LIST OF TABLES WITH PAGE NUMBER

LIST OF PUBLICATIONS

- **International**

1. Nisha Deopa, Mukesh Sahu, Sumandeep Kaur, **Aman Prasad**, K. Swapna, A.S. Rao, **Spectral studies of Er^{3+} ions doped lithium lead alumino borate glasses for visible and 1.5 μm photonic applications, Journal of Rare Earths (2020)**
2. **Aman Prasad,** A.S. Rao, G.V. Prakash**, Up-conversion luminescence and EPR properties of $KGdF_4:Yb^{3+}/Tm^{3+}$ nanophosphors, Optik, 208 (2020) 164538**
3. **Aman Prasad**, A.S. Rao, G.V. Prakash**, A study on up-conversion and energy transfer kinetics of $KGdF_4:Yb^{3+}/Er^{3+}$ nanophosphors, Journal of Molecular Structure 1205 (2020) 127647**
4. Ritu Sharma, **Aman Prasad**, Nisha Deopa, Sumandeep Kaur, Rekha Rani Pokam, M. Venkateshwarlu, A.S. Rao, **Spectroscopic properties of deep red emitting Tm3+ doped ZnPbWTe glasses for optoelectronic and laser applications , Journal of Non-Crystalline Solids 516 (2019) 82-88**
5. Nisha Deopa, Shubham Saini, Sumandeep Kaur, **Aman Prasad**, A.S. Rao**, Spectroscopic investigations on Dy^{3+} ions doped zinc lead alumino borate glasses for photonic device applications, Journal of Rare Earths**, **37 (2019) 52-59**
6. Haruka George, Nisha Deopa, Sumandeep Kaur, **Aman Prasad**, M. Sreenivasulu, M. Jayasimahdri, A.S.Rao**, Judd-Ofelt parametrization and radiative analysis of Dy^{3+} ions doped Sodium Bismuth Strontium Phosphate Glasses, Journal of Luminescence, 215 (2019) 116693**
7. **Aman Prasad,** A. S. Rao, Mohini Gupta, G. Vijay Prakash, **Morphological and luminescence studies on $KGdF_4:Yb^{3+}$ / Tb^{3+} up-conversion nanophosphors**, **Materials Chemistry and Physics 219 (2018) 13-21**
8. Nisha Deopa, Sumandeep Kaur, **Aman Prasad**, Bipin Joshi, A.S. Rao, **Spectral studies of Eu^{3+} doped lithium lead alumina borate glasses for visible photonic applications, Optics and Laser Technology 108 (2018) 434-440**
9. Sumandeep Kaur, Nisha Deopa, **Aman Prasad**, Rajat Bajaj, A.S. Rao, **Intense green emission from Tb^{3+} ions doped zinc lead alumina borate glasses for laser and w-LEDs applications, Optical Materials 84 (2018) 318-323**
10. Sumandeep Kaur, Amit K. Vishwakarma, Nisha Deopa, **Aman Prasad**, M. Jayasimhadri,

A.S. Rao**, Spectroscopic studies of Dy^{3+} doped borate glasses for cool white light generation, Materials Research Bulletin 104 (2018) 77-82**

- **Publications: National**

1. **Aman Prasad**, **Nano-Science and Quality of Life , FUSION 13 (2018) 10-21**

LIST OF CONTENTS

ABSTRACT

RE doped cubic phase $KGdF_4$ up-conversion nanoparticles (UCNPs) have been synthesised by a wet chemical synthesis procedure. The phase confirmation was achieved via XRD analysis. The morphology and size distribution of the UCNPs was analysed through HR-TEM technique. From Debye-Scherrer and HR-TEM calculations, the size of the particles was found out to be in the range of 6-8nm. These morphological characterisations revealed a high degree of crystallinity in the host lattice. EDAX analysis was conducted to confirm the presence and corresponding weight percentages of precursor elements in the host lattice.

The as prepared UCNPs exhibit the property of up-conversion as was evident after conducting UC studies on the samples. Under 980nm CW laser excitation, the samples emit strong emission in the visible region and the intensity of which increases with increase in the concentration of sensitizer (Yb^{3+}) ion. In-depth analysis of energy transfer mechanisms in the UCNP lattice under NIR excitation was conducted. Cooperative energy transfer (CET), energy transfer up-conversion (ETU) and excited/ground state absorptions (ESA/GSA) were established as the main UC mechanisms in the $KGdF_4$ lattice depending upon the sensitizer-activator combination. Inokuti-Hirayama (IH) model was also applied to establish the nature of energy transfer between sensitizer and activator ions as dipole-dipole in nature. Decay kinetics revealed high lifetimes for these samples for the visible emission under NIR excitation. EPR studies were conducted to study the effects of paramagnetic gadolinium ion on the lattice symmetry of $KGdF_4$. The calculated g values from the EPR spectra correspond to the "U" spectrum of gadolinium and match well with the reported values.

These UCNPs have sizes well within the cellular range. Along with the ability to exhibit up-conversion and having high lifetimes, these UCNPs can be easily used as alternatives to

conventional dyes and quantum dots for bio-imaging and other solid state lighting (SSL)/ w-LEDs applications.

Chapter 1: General Introduction

This chapter discusses the fundamentals of up-conversion process. It deals with the science behind the synthesis, morphology, luminescence and applications of up-conversion nanoparticles (UCNPs) in the field of bio-imaging. This chapter highlights the fundamental flaws in the usage of organic dyes and quantum dots that have been conventionally used as imaging probes and illustrates why UCNPs are a way forward as more efficient and favourable probes for bio-imaging. Lastly, it highlights the objectives of this research work.

1.1 What is Up-conversion?

The science of up-conversion was developed by N. Bloembergen in 1959 when he advanced a theory of a device known as "infrared quantum counter" [1]. According to his theory, ions having multiple energy levels could absorb photons of low energy thereby getting excited to intermediate excited states and even further to higher excited states only to finally emit a photon of higher energy. This process was termed as up-conversion. In other words, up-conversion can be defined as a nonlinear optical process involving subsequent absorption of two or more photons of low energy via intermediate long-lived energy states followed by emission of a photon of shorter wavelength than the pump one [2,3].

1.2 Difference between up-conversion and down-conversion

Both up-conversion and down-conversion are nonlinear optical processes. But as the names suggest, in up-conversion, a material is excited by multiple low energy photons only to emit photons of higher energy whereas in down-conversion, the material is excited by high energy photons, which subsequently emits photons of low energy [4–6]. Also, since the intermediate energy levels in up-conversion processes are real as compared to the simultaneous multi-photon absorption processes where the intermediate levels are virtual, the UC processes exhibit higher luminescence efficiencies [1,7]

1.3 Types of up-conversion processes

Simultaneous two photon absorption (STPA), second harmonic generation (SHG) and up-conversion (UC) are common non-linear optical processes involving generation of short wavelength/high energy radiation from long wavelength/low energy excitation sources [8]. In STPA process, there exists only one real excited state and the incoming photon is immediately absorbed thereby exciting the ion from the ground to the excited state. There exists no

intermediate state between the ground and excited states. On the other hand, SHG gives rise to new frequencies via weak wavelength dependent hyperpolarizability of a substance. It is dependent on hyperactive Rayleigh scattering and not on photon absorption [7,9–12].

The UC process is different from STPA and SHG. In UC process, two or more low energy photons are sequentially absorbed resulting in the emission of high energy radiation. The sequential absorption of photons is made possible due to the presence of real metastable states. Thus UC is a two-step process involving sequential absorption of pump photons to multiple metastable excited states followed by luminescence in short wavelength region which can be described as an anti-Stokes mechanism. The emission depends on the excitation intensity, with higher intensities giving higher efficiencies of luminescence. The UC processes can be put into three categories [13]:

1.3.1 Excited State Absorption

Excited state absorption (ESA) was proposed by Bloembergen in 1959. It is a sequential two photon absorption process which has been established as the most acceptable form of UC process [7,13,14]. This process is based on sequential absorption of photons by a single ion. It can occur in lattices with low concentration of dopant ions. The ESA mechanism is shown in Fig.1.1. It can be seen from the figure that, the ions in the ground state absorbs a photon to get excited to an intermediate excited state. This is known as ground state absorption (GSA). Now, the ion in this state again absorbs a photon to get excited to a higher excited state. Transition from this state to the ground state gives rise to UC emission.

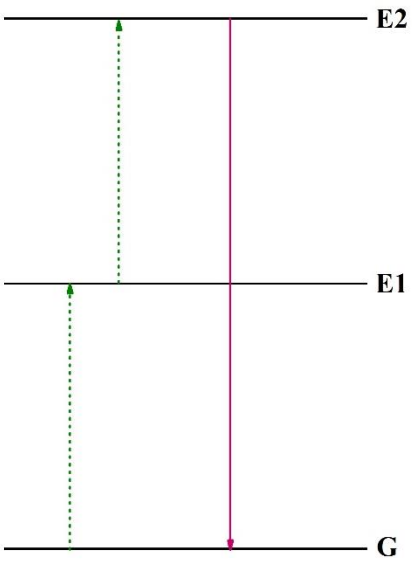

Fig. 1.1: Excited State Absorption

1.3.2 Energy Transfer Up-conversion

Energy transfer up-conversion (ETU) is the most efficient UC process in all the rare earth (RE) doped nanophosphors. It is also known as *addition de photon par transfers d'energies APTE effect* [2,3]. Radiative dipole-dipole interaction is the most dominant amongst all the energy transfer mechanisms. For higher luminescence efficiencies, the dopant ions are required to be in close proximity to each other. Thus, in the case of ETU, lattices which can accept higher dopant ion concentrations are required (even 20 mol% is admissible limit). The energy mechanism scheme is shown in Fig.1.2. From Fig. 1.2, it can be seen that two neighbouring ions successively absorb pump photons for excitation. These two ions can absorb the pump photon of same energy to get excited to intermediate level E_1. One ion again gets excited to an upper state E_2 through a non-radiative energy transfer process from the second ion which relaxes to the ground state. Now this excited ion in E_2 state releases a higher energy photon

while relaxing to the ground state. There are many different kinds of ET upconversion mechanisms:

a) ET followed by ESA, also known as EFE mechanism
b) Successive energy transfer (SET)
c) Cross Relaxation (CR)
d) Cooperative sensitization (CS)
e) Cooperative Luminescence (CL)

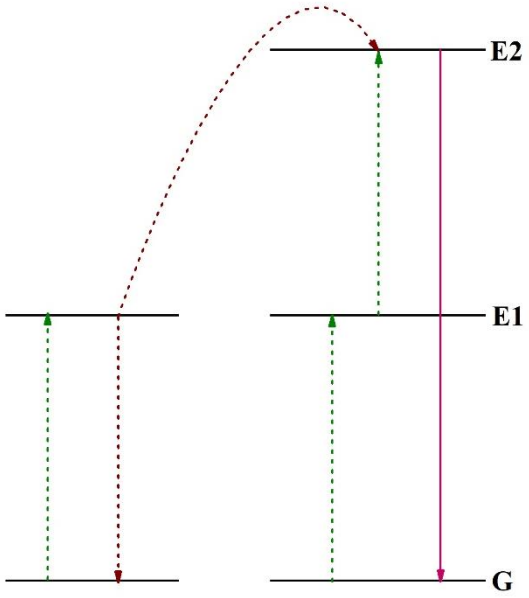

Fig. 1.2: Energy Transfer Up-Conversion

1.3.3 Photon Avalanche (PA)

This mechanism was discovered by Chivian in 1979 and has turned out to be one of the most efficient types of UC processes although it is rarely observed in all UC processes involving ESA and CR. [15]. Fig. 1.3 shows the mechanism in PA process during up-conversion. It can be seen that, ion 1 in ground state is promoted to state E1 by GSA. Now through ESA, another

pump photon can excite it to state E2. Now this ion in E2 can interact with ions in the ground state to produce two ions in state E2. These two ions can subsequently produce four ions which can produce eight and so on. Clearly, state E2 acts as an energy reservoir so that a requisite population of ions for an avalanche can be sustained easily.

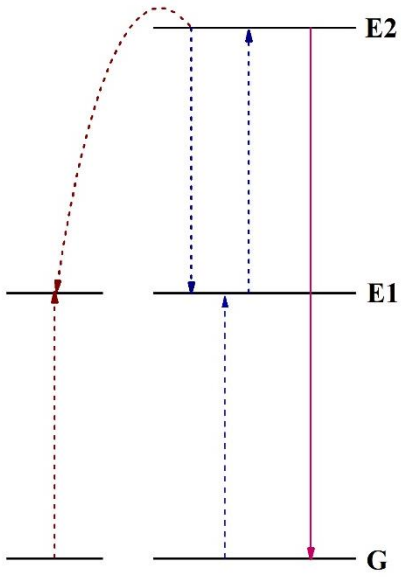

Fig. 1.3: Photon Avalanche

1.4 Definition of Bio-imaging

Bio-imaging is defined as a non-invasive technique of visualizing a biological activity for a specific period of time. There is neither a physical interference nor any inhibition of any bodily process like respiration, movement etc. Clear 3D structural images of subcellular structures and tissues in an organism can be reported using this technique[16–18].

There has been tremendous advancement in image processing technologies since the last six decades especially during the 1980s and 1990s. Use of computers to visualise objects and processes has replaced human vision and has made many scientific discoveries possible in this field. Fig. 1.4 shows the various developments that have taken place in the area of optical

imaging in the last many years. These techniques help segregate and localise the cellular and imaging components due to the development of many high resolution imaging technologies and advanced imaging equipment [19–21].

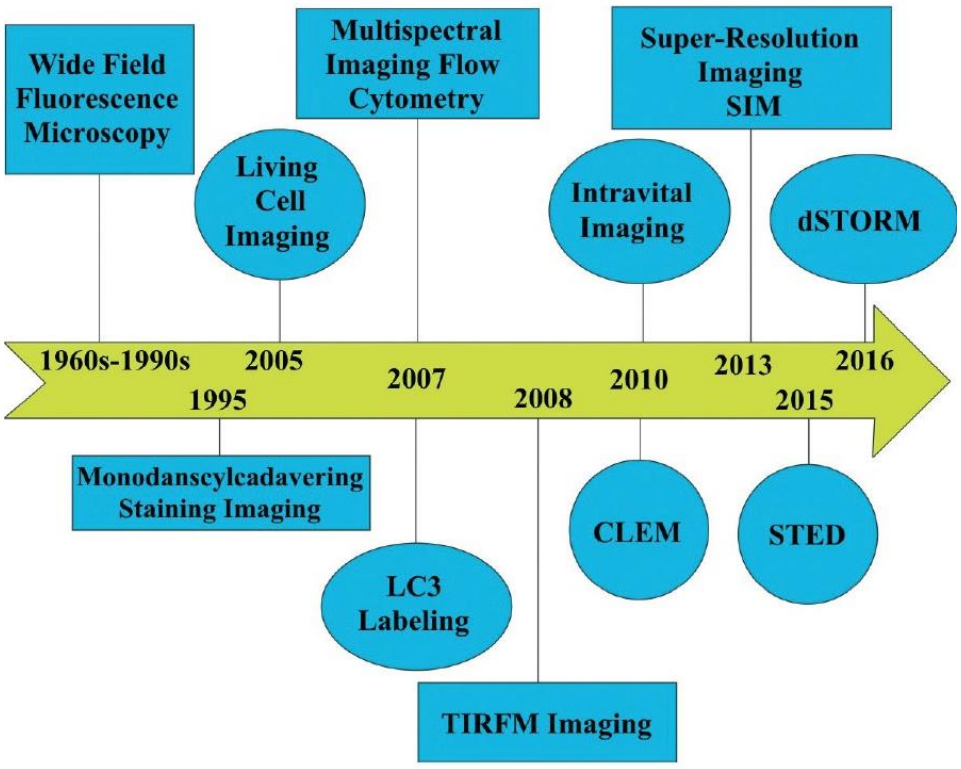

Fig. 1.4: Development of techniques in optical imaging [21]

Many different bio-imaging techniques like thermal imaging, X-ray, X-ray computed tomography (CT), hyperspectral imaging and magnetic resonance imaging (MRI) have seen many developments in the last three decades. All these techniques are based on a different operating principle and have different technologies and instruments [19,22–26]. The basic operating components in all these techniques are nearly equivalent. In general, a bio-imaging setup involves usage of a camera, an illumination source, a frame grabber and image processing hardware and software [19,20]. The image of the biological phenomenon is captured by the camera and a charge-coupled device (CCD), X-ray, X-ray CT, MRI etc. are used to determine specific properties and characteristics like shape, size, color, texture etc. The most commonly

used sensor is CCD only for such purposes[27]. The analog signal is then converted into a digital signal via a digitization process. This is done by using the frame grabber. The obtained digital signal has to be then processed by the hardware and software tools via processes like image acquisition, image pre-processing, enhancement, segmentation, representation and description for the desired output and further analysis.

1.5 Bio-imaging using Nanoparticles or Nano Bio-imaging

Despite all the advances in the techniques that have been made in the field of bio-imaging, the problem of higher resolution of images for better assessment still persists [19]. Super resolution microscopy has been developed to address some of the resolution issues to provide a certain level of advancement in the area of biomedicine; but it also faces certain equipment requirements which makes it hard to use and less efficient [28–30]. Biologists though are of the idea that application of one single technique to the sample does not translate into good results and information about the biological sample [31]. A study conducted by Hauser et al. shows that usage of two or more techniques on one single biological sample leads to good analytical results thereby overcoming the shortcomings of earlier techniques. By employing a correlative approach, one gets new dimensions in the output information, providing new opportunities in the area of super-resolution microscopy [32].

Structured Illumination Microscopy (SIM) was developed for further resolution enhancement. But in this case, expensive hardware and software tools for improving the super resolution of SIM are required. Ponsetto et al. have explained in their studies that these methods are a trade-off between speed, resolution, field of view, biocompatibility, sensitivity and experimental complexity [33,34]. Developments in the field of fluorescence microscopic techniques, stochastic reconstruction microscopy (STORM), photoactivated localization microscopy (PALM), stimulated emission depletion (STED) and SIM have been compared by So et al. in

their studies [35]. They have deduced that, conventional microscopy procedure can lead to new generation of nanoscopy if label free optical microscopic techniques originating from nanoscale structures like micro-curvilinear lenses, super-oscillatory and metamaterials are employed [35].

Nanotechnology indeed can solve the issue of high resolution image construction. The resolution of current techniques can be increased by employing nanotechnology [19,36]. Targeted imaging can be achieved using specifically designed nanoparticles [19]. As has been demonstrated by Goel et al., incorporating nanotechnology with positron emission tomography (PET) can indeed enhance the sensitivity and quantitative nature of PET thereby leading to mitigation of certain shortcomings associated with this field [37]. Fluorescence bio-imaging in the near infrared region (NIR-II, 1000-1700nm) provides advantages like large penetration depth and high spatial resolution due to low scattering of NIR light thereby enabling NIR-II quantum dots (QDs) to be used in many biomedical applications[37,38].

1.6 Shortcomings of conventional methods of bio-imaging

As has been discussed earlier, scientists have made great advances in the field of nanoscience by developing fluorescent nanoparticles for bio-imaging applications [13]. These nanoparticles are conjugated with certain biomolecules, which under suitable excitation, are able to emit detectable fluorescent signals for biological analysis and understanding. In order to achieve this, the fluorescent nanoprobe must be biocompatible, non-toxic, resistant to photobleaching and ultrasensitive. It should have impeccable physical and chemical stability along with a high luminescence efficiency [39–41].

Organic dyes and fluorescent proteins have been the most commonly used bio-imaging probes in the last decade. Traits like small sizes, high fluorescent intensity, good biocompatibility and easy surface modification for bioconjugation make these organic dyes better than other

fluorescent molecules [39]. But these dyes suffer from photobleaching, have narrow absorption and broad emission spectra and are susceptible to chemical instability which hamper their detection[13,42].

Quantum dots (QDs) have been developed with advances in nanotechnology as alternatives to conventional organic dyes. This is because they have certain advantages like good photoluminescence, good photo stability, size tunable emission and broad UV excitation and narrow emission [43]. However, QDs suffer from cytotoxicity and chemical instability [17,44]. Most importantly, the conventional tools for bio-imaging i.e., quantum dots, organic dyes, fluorescent proteins, require short wavelength/high energy or UV excitation for emission purposes. There are certain disadvantages associated with this technique [13,44,45]:

1) Usage of high energy or short wavelength radiation results in low penetration depth of the radiation.
2) High energy radiation can even cause irreparable or fatal damage to the biomolecules, area to be imaged in the body and the surrounding healthy tissues.
3) There is a significant amount of autofluorescence which leads to a low signal to noise ratio (SNR).

Thus a need was felt to develop a different class of fluorescent nanoprobes that would be capable of overcoming the above mentioned shortcomings of the conventional tools of bio-imaging.

1.7 Up-conversion Nanoparticles (UCNPs)

Up-conversion nanoparticles (UCNPs) find tremendous use in drug delivery, bio-imaging and therapy [46]. There are many reasons for this. Firstly, UCNPs work on the principle of up-conversion which is a nonlinear optical process involving sequential absorption of two or more

low energy pump photons resulting in the emission of photons of higher energy i.e., these UCNPs upon excitation by NIR radiation emit higher energy photons in UV or visible region [7]. This characteristic of UCNPs actually provides an edge over conventional imaging probes enabling the UCNPs to have minimum autofluorescence, narrow emission bandwidths, large anti-Stoke shifts, minimal photobleaching, minimum light scattering, non-blinking and deeper tissue penetration due to usage of low energy radiation for excitation purposes [47]. Due to high photostability, UCNPs have been employed for imaging and other therapeutics both in vitro and in vivo. UCNPs emitting in the visible region have been employed for multi-color cell imaging and imaging within shallow tissues [48].UCNPs utilising NIR radiation for both excitation and emission purposes are helpful for in vivo imaging in small animals because of deeper tissue penetration and less radiation scattering [46].

Secondly, UCNPs can be easily conjugated with therapeutic agents due to superior surface chemistry properties. Monodisperse UCNPs can be synthesised in various shapes and sizes thereby providing a large surface area for effective conjugation with organic ligands/drugs [49]. Such conjugation can take place via non-covalent or a covalent interaction between the UCNPs and the drug/ligand. Above all, UCNPs are nontoxic and biocompatible (devoid of cadmium, mercury, lead, selenium and arsenic) rendering them highly useful for biomedical applications.

1.7.1 Structure of UCNPs

Fig. 1.5 gives a basic structure and UC mechanism taking place in a UCNP. Primarily, lanthanide (Ln) doped UCNPs have emerged as the most promising alternatives to conventional imaging probes due to the superior optical and biological advantages they possess over the conventional fluorescent probes. The Ln doped UCNPs consist of three components: a host matrix, a sensitizer (i.e., absorber) and an activator (i.e., emitter) [12,13,41]. The sensitizer absorbs the incoming NIR radiation, rising to an upper excited state. After this, the

energy from the excited sensitizer is transferred to the activator ion in ground state raising it subsequently to a higher excited state leading to emission of higher energy or short wavelengths.

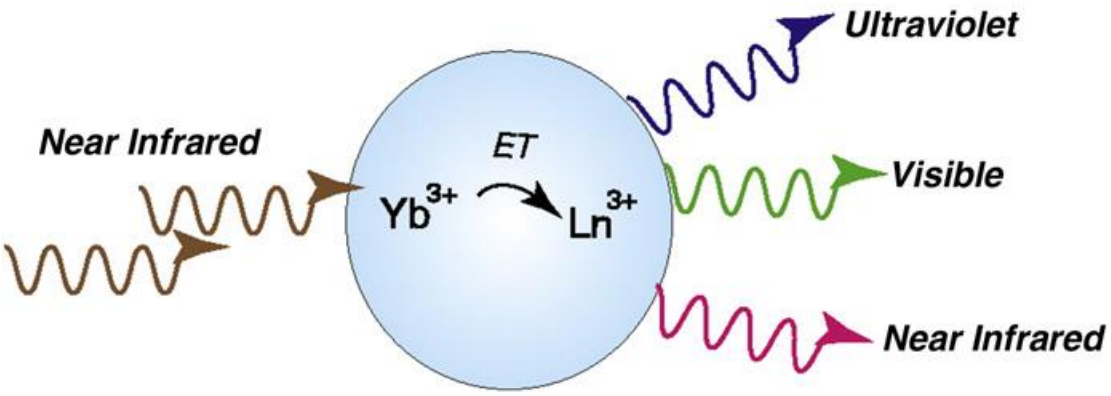

Fig. 1.5: Structure of UCNPs [46]

1.7.2 Activators

Lanthanides possess multiple metastable states which are a prerequisite for UC process thereby making them suitable as a component for UCNPs. The lanthanides primarily exist as trivalent ions (Ln^{3+}) which is their most stable state. The completely filled $5s^2$ and $5p^6$ sub-shells shield the 4f electrons in Ln^{3+} which results in weak electron-phonon coupling leading to sharp and narrow f-f transition bands. Also, since f-f transitions are Laporte forbidden, the transition probabilities are pretty low and excited states have a large lifetime (up to 0.1s) [7,12]. UC emission is ideally expected from most lanthanide ions as they generally have more than one excited 4f level (with the exception of La^{3+}, Ce^{3+}, Yb^{3+} and Lu^{3+}). But for efficient UC emission, the energy difference between each excited level and its lower lying intermediate level (ground level) should be nearly equivalent to allow photon absorption and energy transfer to take place in the UC process.

Rare earth ions like Er^{3+}, Tm^{3+}, Ho^{3+} are frequently used as activators in the UCNP lattice because they possess ladder like energy levels [50]. Fig.1.6 shows the energy level scheme of

these ions. It can be seen from the below figure that $^4I_{11/2}$ and $^4I_{15/2}$ are separated by nearly 10350 cm^{-1}. This energy difference is comparable with the energy difference between $^4F_{7/2}$ and $^4I_{11/2}$ (nearly 10370cm^{-1}) thereby making these energy levels eligible for UC process under 980 nm excitation. The Er^{3+} ion is not directly excited to the $^4F_{7/2}$ state. Rather, from the $^4I_{11/2}$ state it relaxes to the $^4I_{13/2}$ state followed by excitation to the $^4F_{9/2}$ state via phonon assisted energy transfer.

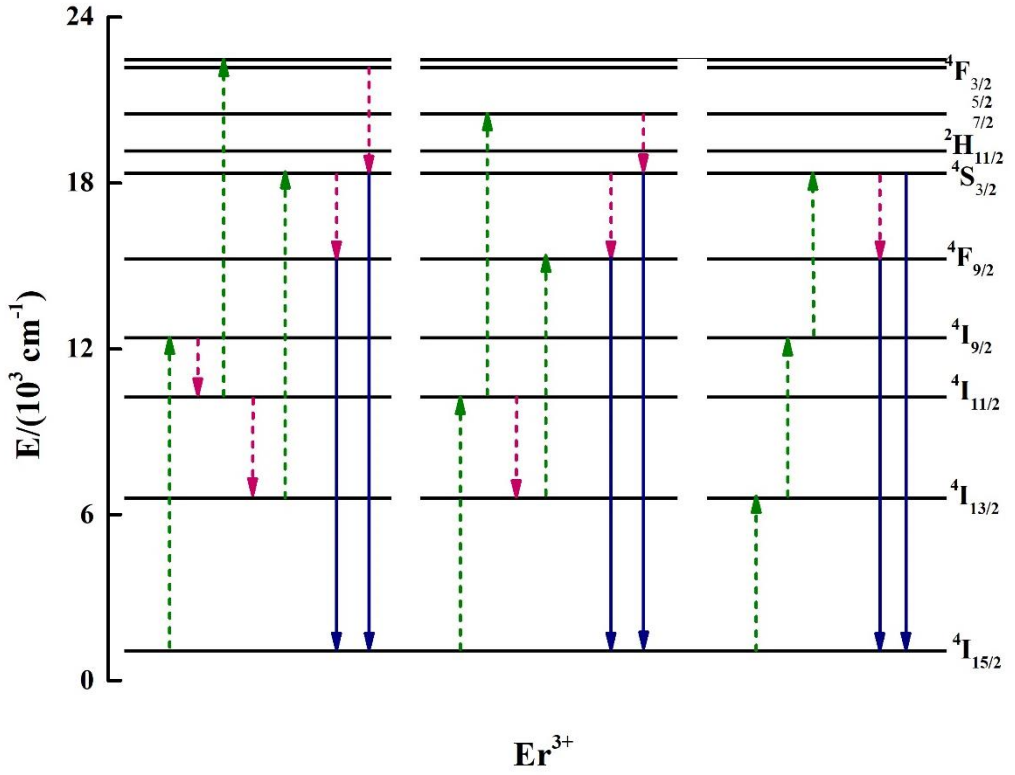

Fig. 1.6: Energy level scheme of activator ions

The efficiency of the UC process is further dependent on non-radiative multiphoton relaxation rates between different energy levels affecting the population of intermediate and emitting energy levels. For the lanthanide ions, the multiphoton relaxation rate constant k_{nr} for 4f levels of lanthanide ions is given as [51]:

$$k_{nr}\,\alpha\,\left(\frac{-2\pi\beta\Delta E}{\hbar\omega_{max}}\right) \qquad (1.1)$$

where β is the empirical constant of the host, ΔE is the enrgy difference between the populated level and next lower level in the lanthanide ion and $h\omega_{max}$ is the highest vibrational energy mode of the lattice. As is evident from Fig. 1.4, Er^{3+} and Tm^{3+} ions have low probability of non-radiative transitions between excited energy levels due to large energy gaps. Therefore, UCNP lattices with Er^{3+} and Tm^{3+} as activators are most efficient for UC process.

1.7.3 Sensitizers

Two parameters that affect the up-conversion process are distance between two neighbouring activator ions and their absorption cross-section in singly doped nanophosphors. Doping level of the activator ions should be kept low so as to avoid quenching of excitation energy [12,46]. Due to low absorption cross sections of activator ions, the UC efficiency of singly doped UCNPs is low.

For increasing luminescence efficiency of the UC process, the host UCNP lattice having an activator ion is codoped with a sensitizer ion. This sensitizer has a large enough absorption cross section in the NIR region facilitating the ETU process between sensitizer and activator [14]. As is evident from Fig. 1.7, Yb^{3+} is a trivalent ion possessing a simple energy level scheme with $^2F_{5/2}$ being the sole excited state [3,4]. Yb^{3+} ion has an absorption band located at 980nm because of the fact that absorption cross-section of $^2F_{7/2} \longrightarrow {}^2F_{5/2}$ transition is greater than other lanthanide ions. Also, this transition of Yb^{3+} ion corresponds to the f-f transition of many up-converting activators like Er^{3+} resulting in an efficient energy transfer from the sensitizer to the activator during the UC process. Yb^{3+} ion is therefore the most commonly used UC sensitizer. In the UCNP lattice, the concentration of the sensitizer is kept high (~20-30mol%) while the activator concentration is kept low (~2mol%) so as to minimise the cross relaxation energy loss [12,13,46].

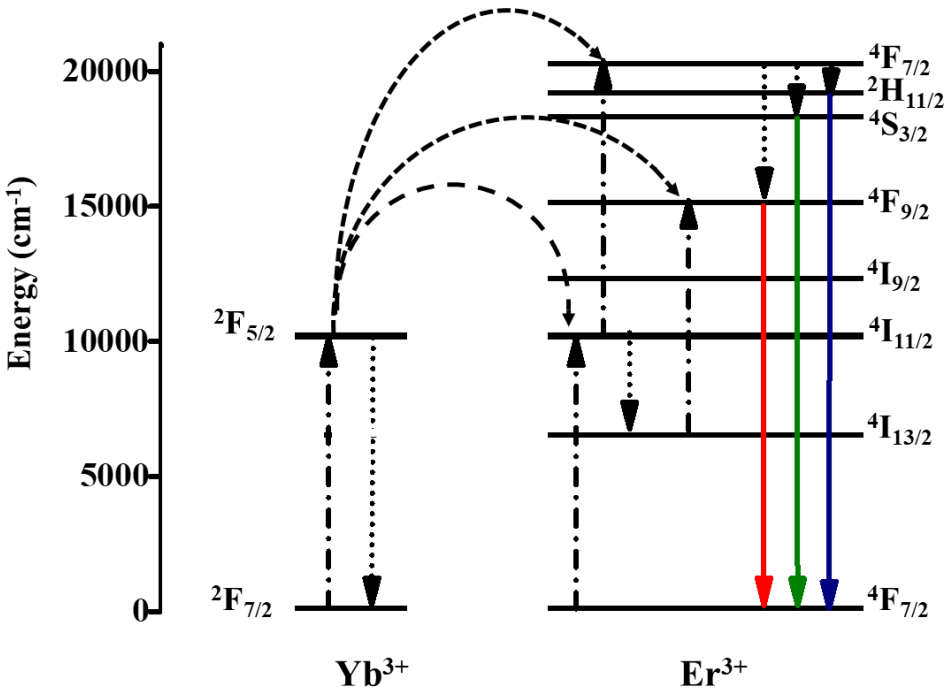

Fig. 1.7: Energy level scheme of sensitizer ion

1.7.4 Choice of host material

The selection of appropriate host material for synthesis of UCNP lattice is very important as it directly affects the UC process and efficiency. It is generally required that the host material should have relatively low phonon energies and should resemble the lattice structure of the dopant ions [12]. Low phonon energy is an essential requirement as it minimizes the non-radiative losses thereby maximising the radiative emission. Although heavy halides like chlorides, bromides and iodides have low phonon energies (less than 300cm^{-1}), they are hygroscopic which limits their function. Oxides are chemically stable but they have high phonon energies (greater than 500cm^{-1}) which again limits their use. Fluorides on the other hand have low phonon energies (nearly 350cm^{-1}) and are chemically stable as well. Thus fluorides have been widely used as an ideal UCNP host lattices [12,13].

The crystal structure of the host material can affect the luminescence efficiency during the UC process. It is well known that, hexagonal phase $NaYF_4$:Yb^{3+}/Er^{3+} UCNPs have better UC luminescence efficiency than the cubic phase of the same compound [52–54]. This property is due to different crystal fields around the trivalent lanthanide ions in lattices of different symmetries [12]. Lattices that have low symmetries generally exert a crystal field containing more uneven components around dopant ions as compared to lattices with high symmetries. This leads to enhanced electronic coupling between 4f energy levels and higher electronic levels thereby increasing the f-f transition probabilities of the activator-sensitizer ions [55]. Greater UC efficiency can also be achieved by decreasing the cation size or the unit cell volume of the host resulting in the crystal field strength around the dopant ions.

1.8 Status of research in the field of up-conversion nanoparticles

1.8.1 Synthesis Procedures

Several procedures to synthesize up-converting nanoparticles have been developed in the recent years. Co-precipitation, thermal decomposition, hydrothermal/solvothermal and sol-gel methods are some of the most commonly used methods to prepare UCNPs [6,46,56]. For the purpose of biological applications, the UCNPs must have a narrow size distribution and high dispersibility. To achieve this, wet chemical methods, especially hydrothermal/solvothermal methods and thermal decomposition methods are mostly used [12,46]. Some of the techniques used to synthesise the UCNPs are given below:

1.8.1.1 Co-precipitation Method

This method is one of the most easy and convenient methods to synthesize UCNPs. This is because of mild reaction conditions, low cost requirements, non-complex protocols and shorter reaction times [12,13]. It involves utilising a precipitation reaction between positive and

negative ions present in homogenous solution so as to get a uniform precipitation of UCNPs [14]. Guo et al. synthesised a series of $Lu_6O_5F_8$:20%Yb^{3+},1% Er^{3+}(Tm^{3+}) UCNPs having variable Li^+ concentration. It was reported by them that addition of Li^+ ion increased the UC, DC and CL intensities of the UCNPs [57]. Li et al used a modified high temperature (~305^{o}C) co-precipitation method to synthesize $NaLnF_4$ UCNPs. They were successful in controlling the size and phase of the UCNPs by addition of ions like Mg^{2+} and Co^{2+}. As a result, the UCNPs exhibited small sizes and hexagonal phase leading to increased luminescence efficiency [58]. Chow et al. were able to synthesize LaF_3 UCNPs with sizes of around 5nm from water soluble inorganic precursors. They used synthetic ammonium di-noctadecyldithiophosphate as a capping agent for controlling particle growth and to provide stability against agglomeration. These UCNPs could be easily dispersed in solutions thereby rendering them immensely helpful as luminescent probes for bioimaging applications [59]. Yi et al. synthesised $NaYF_4$:Yb^{3+},Er^{3+} UCNPs using a co-precipitation method utilising ethylenediamine tetraacetic acid (EDTA) in the process. RE-EDTA complex was injected quickly to a NaF solution under vigorous stirring resulting in the formation of cubic phase $NaYF_4$:Yb^{3+},Er^{3+} UCNPs through a homogenous nucleation process. The sizes of the UCNPs could be controlled by varying the molar ration of EDTA and RE ions. As is known, the fluorescence intensity of cubic phase UCNPs is too weak for any useful biological application, these UCNPs were subjected to annealing to change their phase from cubic to hexagonal. As a result, their luminescence intensity increased by 40 times [60].

The $NaYF_4$ UCNPs obtained from co-precipitation method require an annealing treatment in order to bring about a change in the phase of the particles leading to increase in UC luminescence intensity. But this leads to aggregation of the particles leading to increase in their sizes. Also, heating can lead to carbonization of capping agents like EDTA thereby decreasing their hydrophilicity. Further surface modifications are then required to make the UCNPs water

soluble. Thus, UCNPs prepared via co-precipitation method have a limited use in biological applications [13].

1.8.1.2 Thermal Decomposition Method

In this method, rare earth metal trifluoroacetates are used as raw materials. These are mixed at fixed proportions and then decomposed under high heating to form UCNPs. Although, the synthesis of the UCNPs is susceptible to change in temperature, pressure and additives, it still remains one of the most used methods for preparation of UCNPs [14].

Zhang et al. reported a novel synthesis of single crystalline and monodisperse LaF_3 triangular nanoplates via thermal decomposition of lanthanum trifluoroacetates ($La(CF_3COO)_3$). Since then, this method has become the most commonly used procedure to synthesize high quality RE doped $NaYF_4$ UCNPs[61]. Capobianco et al. synthesized $NaYF_4$ UCNPs doped with Yb and co-doped with Er and Tm via thermal decomposition of metal trifluoroacetate precursors in the presence of oleic acid and octadecene. Octodecene was chosen as a solvent due to its high boiling point (~315^oC) whereas oleic acid was used both as a solvent and as a capping agent to prevent agglomeration of the UCNPs [62]. Nigoghossian et al. prepared $NaGdF_4:Yb^{3+}/Er^{3+}$ UCNPs via two pot thermal decomposition process as core structure in the presence of oleic acid and 1-octadecence [63]. The UCNPs were synthesised at 310^oC, 315^oC and 320^oC with silica being used as a capping agent. Cubic phase of UCNPs was achieved at 310^oC and 315^oC whereas synthesis at 320^oC yielded hexagonal phase [63]. Mai et al. have reported a general synthesis technique of $NaREF_4$ (RE= Pr to Lu, Y) UCNPs with $Na(CF_3COO)$ and $RE(CF_3COO)$ as precursors; These UCNPs are of high quality i.e., they are monodisperse, single crystalline, well-shaped and phase pure. The reaction mixture consisted of a non-coordinating solvent (1-octadecene) and a coordinating solvent (oleic acid and oleyamine). Through their studies they showed that pure β-$NaYF_4$ could be synthesized from

the oleic acid-octadecene system under extreme conditions (high Na to RE ratio, high temperature and longer reaction time) whereas pure α-$NaYF_4$ could be prepared from oleic acid-oleyamine-octadecene complex under relatively mild conditions (low Na to RE ratio, short reaction times and low temperature) [56]. Despite being widely used to prepare UCNPs, this methods has its limitations such as requirements of harsh conditions, high costs of reagents, complex reaction steps and high toxicity [14].

1.8.1.3 Hydrothermal/Solvothermal Method

Hydrothermal/Solvothermal technique refers to a synthesis procedure in which reactants are placed under high temperature and pressure in a sealed environment. Generally, the temperature of the solvent is above its critical point. To provide a sealed reaction environment, specialised vessels known as autoclaves are used [13]. Sun et al. synthesized α-$NaYF_4$ and β-$NaYF_4$ UCNPs codoped with Yb^{3+}, Er^{3+} with RE-EDTA or RE-citrate complexes as precursors. EDTA and citrate were used as capping agents to control the size and morphology of the as prepared UCNPs. It was found that the particle size was dependent on nucleation rate which in turn is controllable by concentration of reactants, molar ratio of RE, capping ligands of NaF and choice of capping ligands [64]. Du et al. reported a series of $NaYF_4$ UCNPs codoped with Yb^{3+}/Er^{3+} prepared via hydrothermal method. They were able to control the phase and size of the UCNPs by controlling the synthesis temperature [65].

Wang et al. reported, for the first time, a one-step synthesis technique of biocompatible and water soluble polyethylenimine (PEI)-coated $NaYF_4$:Yb^{3+},Er^{3+}/Tm^{3+} UCNPs via solvothermal approach. PEI, being an organic polymer surfactant, was employed to control the particle size and prevent agglomeration. Apart from this, the presence of free amine groups on the surface of the UNCPs helps in binding to biomolecules thereby rendering these UCNPs usable in biological applications [66]. Another group, Wang et al., have reported two phase solvothermal

synthesis of $NaYF_4$:Yb^{3+},Er^{3+}/Tm^{3+}/Ho^{3+} UCNPs in a water-ethanol-OA system. In this study, RE stearate was used as a precursor. The same group also reported one step synthesis of $NaYF_4$:Yb^{3+},Er^{3+} UCNPs coated with various polymers like polyvinylpyrrolidone (PVP), polyethylene glycol (PEG), polyacrylic acid (PAA) and PEI. These capping polymers made the UCNPs hydrophilic and prevented aggregation [67,68].

There are many key advantages of employing a hydrothermal/solvothermal approach in the synthesis of UCNPs[13,69,70]:

1) Product purity is high
2) Size, structure and morphology of the UNCPS can be easily controlled
3) Lower reaction temperatures
4) Overall simple procedure

Disadvantages with this method are requirement of specialised vessels known as autoclaves and the inability to observe the UCNPs while are they synthesising [12].

1.8.1.4 Sol-gel method

Sol-gel process involves usage of metal compounds, metal alkoxides and inorganic salts as substrate. These are then subjected to hydrolysis and polycondensation processes to gel them together. Sintering or drying is done afterwards to obtain the UCNPs[14]. Park at al. were able to successfully synthesize $NaYF_4$ thin films and nanopatterns by sol-gel process and soft lithography. The light coupling output efficiency was enhanced by the nanopattern and the UC intensity was found to increase 2-3 folds [71]. Liang et al. were able to produce $NaYF_4$:Yb^{3+},Er^{3+} UCNPs via sol gel method. They varied the concentrations of Li^+ and K^+ in the UCNP lattice. They able to increase the luminescence intensity of the UCNPs without changing the shapes and sizes of the particles [72].

1.8.1.5 Microemulsion Method

This is a synthesis technique in which two immiscible solvents form an emulsion under the effect of a surfactant. Subsequent nucleation, agglomeration and heat treatment in microbubbles leads to the synthesis of UCNPs [14]. Qian et al. were able to prepare $NaYF_4$:Yb^{3+},Er^{3+}@Silica core@shell UCNPs via reverse microemulsion method. They used a combination of two surfactants polyoxyethylene (5) nonylphenylether and 1-hexanol. The particle size was in the range of 11.1 ± 1.3 nm [73].

1.8.2 Surface Modifications of UCNPs

It has been observed the UCNPs prepared via above methods are generally hydrophobic due to presence of organic ligands like oleic acid on their surface. If in any case, the UCNPs are water soluble then there are no proper functional groups present on the surface of the UCNPs which can facilitate their conjugation with biomolecules for usage in biological applications. Therefore, it becomes imperative to modify the surface of the as prepared UCNPs so that they are easily conjugated with required biomolecules and ligands. This modification can be done either by an inorganic shell/layer or by an organic ligand.

1.8.2.1 Using an Inorganic Shell Layer for Surface Modification

Surface silanization is the most commonly used surface modification technique for an inorganic capping of the UNCPs. Amorphous silica is coated on the surface of the UCNPs in this procedure. This is achieved by utilising STOBER technique involving hydrolysis and condensation of siloxane precursors like tetraethoxysilane (TEOS) in the presence of ammonia and ethanol[13,74].

Li et al. synthesized polyvinylpyrrolidone (PVP)-stabilized $NaYF_4$:Yb^{3+},Er^{3+}/Tm^{3+} UCNPs and coated them with a layer of silica through the STOBER procedure. The technique has been

represented in Fig.1.8. The thickness of silica in their UCNPs was 10nm which could be adjusted within 1-3 nm by controlling the amount of TEOS taken. This increases the stability of the as prepared UCNPs in water and they show a strong UC fluorescence [75].

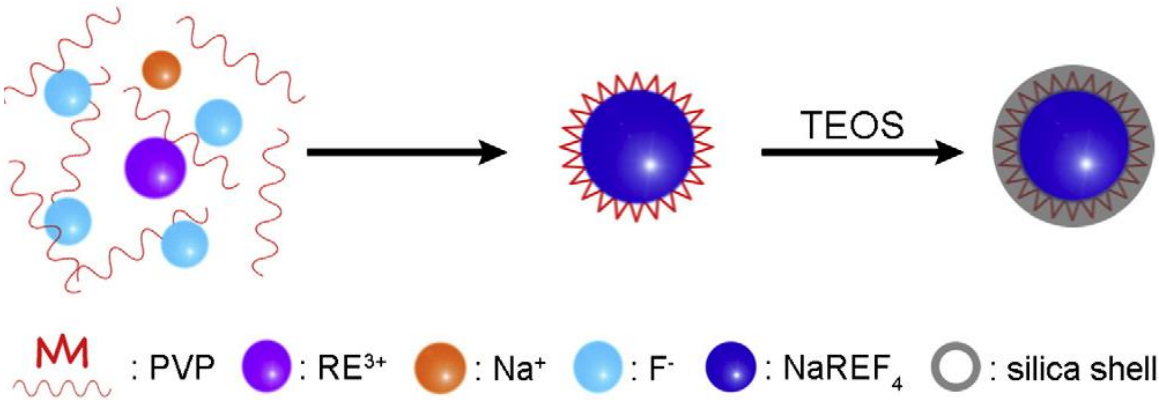

Fig. 1.8: Scheme showing surface silica coating of (PVP)-stabilized $NaYF_4$:Yb^{3+},Er^{3+}/Tm^{3+} UCNPs [75]

Coating with silica provides stability to the as prepared UCNPs but it doesn't provide functional groups on the surface for bioconjugation. To overcome this issue, hydrolysis of amino siloxanes like (3-aminopropyl) triethoxysilane (APS) is performed so as to provide functional amino groups on the surface of the UCNPs [13].

A novel surface modification technique to prepare silica coated multicolour UCNPs working on frequency resonance energy transfer (FRET) mechanism was reported by Li et al. In their studies, certain organic dyes or quantum dots were encapsulated with $NaYF_4$:Yb^{3+},Er^{3+} or $NaYF_4$:Yb^{3+},Tm^{3+} UCNPs respectively via STOBER bases microemulsion method. Under 980 nm excitation, the UC emission energy was transferred to the organic dyes or quantum dots via FRET mechanism generating different colours (depending on the organic dyes or quantum dots). These multicolour nanoparticles find immense usage in multiplexed bioassays [76]. The scheme of the mechanism has been illustrated in Fig.1.9.

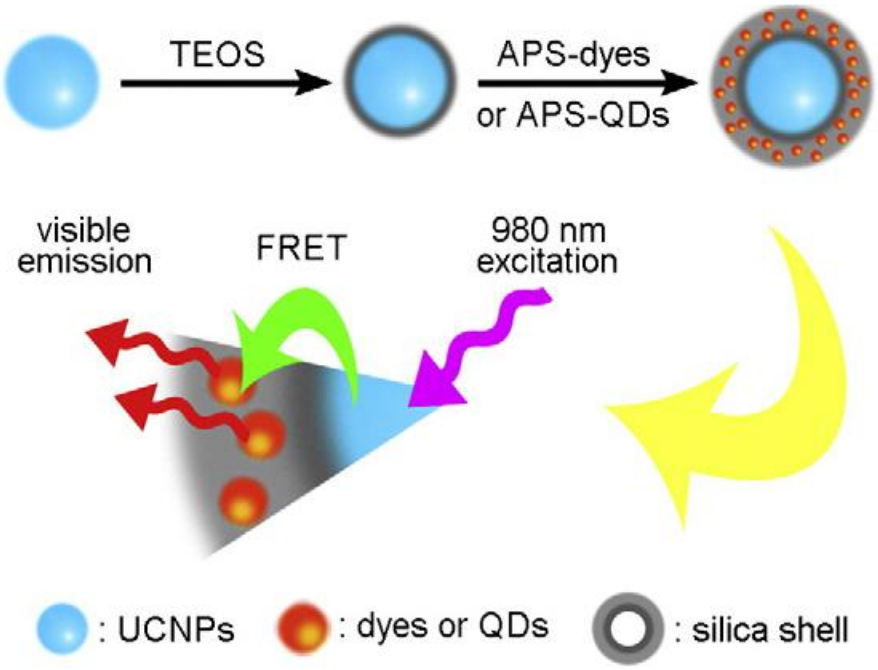

Fig. 1.9: Schematic illustration of FRET mechanism in multicolour UCNPs under 980nm excitation [13]

Lu et al. developed $NaYF_4:Yb^{3+},Er^{3+}$ core shell UCNPs keeping in mind the multifunctional aspects of UCNPs in biological applications. These UCNPs had magnetic, biological and fluorescent characteristics [77]. They used iron oxide nanoparticles as magnetic core and encapsulated them with $NaYF_4:Yb^{3+},Er^{3+}$ particles through a co-precipitation method. The particles were subjected to annealing which enhanced their luminescence intensity. Subsequently these UCNPs were then coated with silica and amine-functionalised by hydrolysis of TEOS and APS which made them water soluble and biocompatible as has been shown in Fig.1.10.

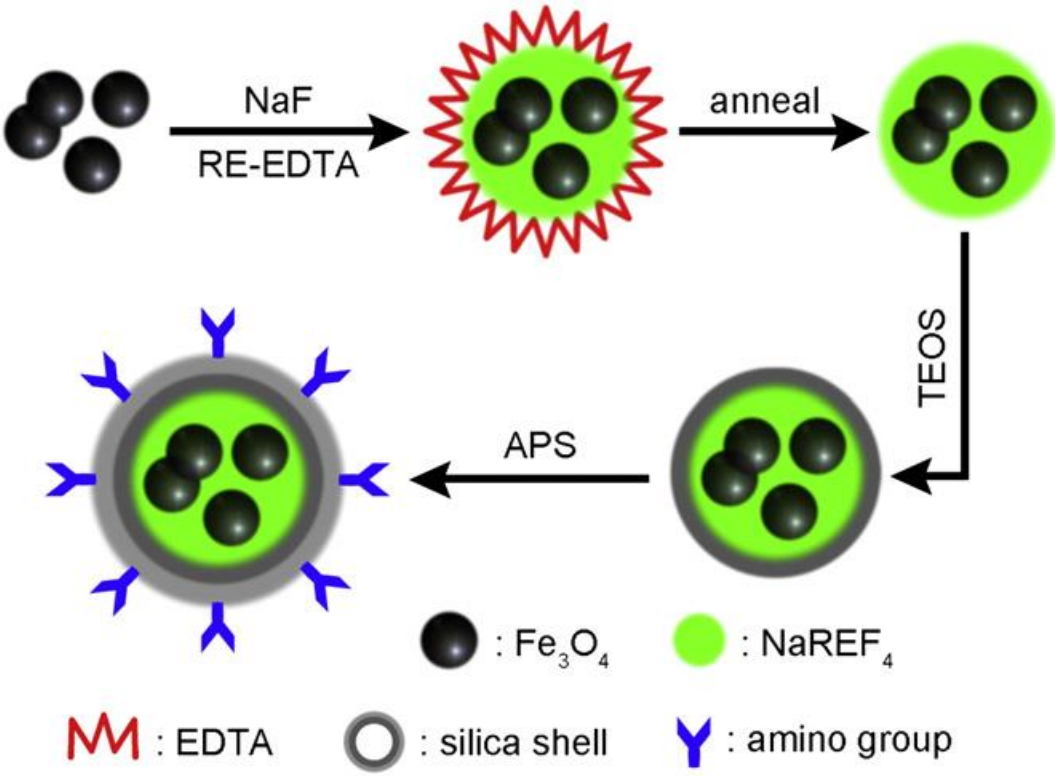

Fig. 1.10: Schematic illustration of surface modification of iron oxide based $NaYF_4:Yb^{3+}.Er^{3+}$ UCNPs [13]

Similarly, Mi et al. reported in their studies that functionalised $Fe_3O_4/NaYF_4:Yb^{3+},Er^{3+}$ magnetic-luminescent nanocomposites could be readily conjugated with antibodies for identification of mammalian cells. They were able to conjugate transferrin protein on the surface of these nanocomposites which in turn was able to recognize the over-expressed transferrin receptors on HeLa cells[78].

1.8.2.2 Surface Modification Using Organic Ligands

UCNPs should not only have high luminescence efficiency but they must also be compatible with biomolecules and other biomolecular assemblies like live cells if they are to be readily used for biological applications. Some techniques enumerating various methods of surface functionalisation through organic ligands are given below.

Chow et al. synthesised hydrophilic $NaYF_4:Yb^{3+},Er^{3+}$ UCNPs via ligand exchange technique(shown in Fig.1.11). These UCNPs were earlier stabilised with oleylamine ligands.

In this procedure, the main ligands are replaced by bifunctional organic molecules (polyethylene glycol 600 diacid) rendering the UCNPs water soluble. These UCNPs can also conjugate to biological assemblies through bioconjugate chemistry[79].

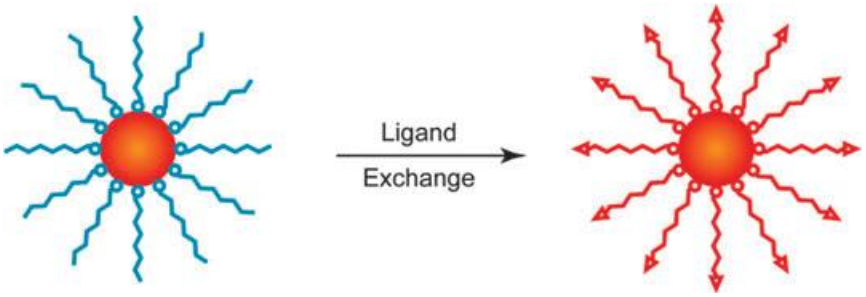

Fig. 1.11: Schematic illustration of ligand exchange process [12]

Ligand oxidation is another technique for surface functionalisation of UCNPs. Li et al. used Lemieux –von Rudloff reagent to convert OA stabilised hydrophobic $NaYF_4$:Yb^{3+},Er^{3+} UCNPs into hydrophilic nanoparticles. The monounsaturated carbon-carbon double bonds are oxidised into carboxylic acid groups. This is useful for bioconjugation of these UCNPs with other biomolecules [80]. Ligand oxidation is represented in Fig. 1.12.

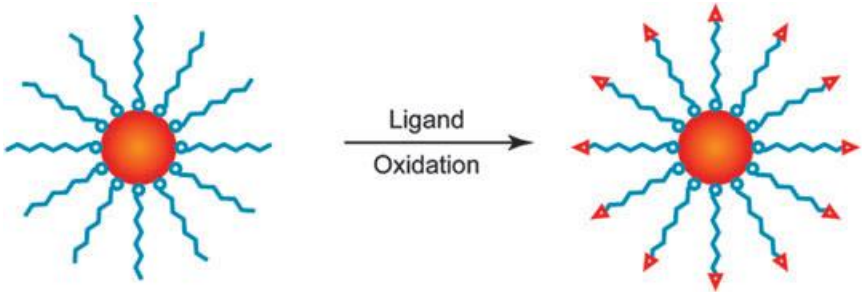

Fig. 1.12: Schematic illustration of ligand oxidation process [12]

It is possible to retain the original hydrophobic ligands on the surface of the UCNPs. This can be achieved by surface functionalisation via hydrophobic Van der Waals interactions with amphiphilic polymers. This ligand attraction scheme is given in Fig.1.13. Chow et al. coated core-shell $NaYF_4$:Yb^{3+},Er^{3+} UCNPs with carboxyl groups. Polyacrylic acid (PAA) modified with octylamine and isopropylamine was used as coating material. The UCNPs still have an

outer hydrophilic block that makes them water soluble and allows further functionalization [81].

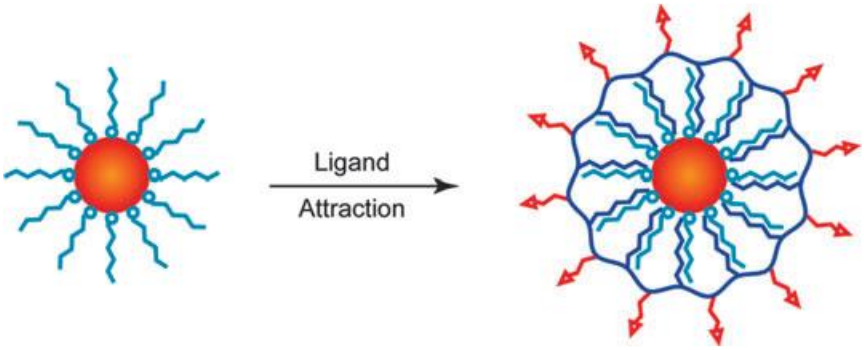

Fig. 1.13: Schematic illustration of ligand attraction process [12]

Li et al. were able to develop a layer-by-layer (LBL) assembly strategy for surface functionalisation. The schematic illustration of LBL technique is given in Fig.1.14. This method involves oppositely charged liner polyions that are used to generate hydrophilic UCNPs. They were able to successfully modify the surface of $NaYF_4:Yb^{3+},Er^{3+}$ UCNPs with stable amino rich shells via sequential adsorption of positively charged poly (allylamine hydrochloride) (PAH) and negatively charged poly (sodium 4-styrenesulfonate) (PSS). The prime advantage of this technique is high stability and biocompatibility that it offers to the UCNPs for various biological applications[82].

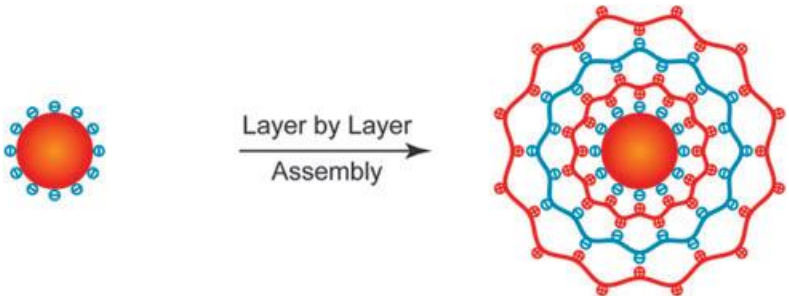

Fig. 1.14: Schematic illustration of LBL assembly process[12]

1.8.3 Examples of UCNPs used in biological applications

It has already been discussed that RE doped UCNPs require NIR radiation for excitation purposes. This has many advantages like 1) high signal to noise ratio (SNR) 2) larger penetration depth due to usage of long wavelength radiation 3) less damage to the tissue under NIR excitation. This makes RE doped UCNPs a better alternative to conventional dyes and quantum dots for in vitro cell and in vivo tissue imaging.

1.8.3.1 In vitro cell labelling and imaging

Chatterjee et al. first reported the use of $NaYF_4:Yb^{3+},Er^{3+}$ UCNPs in cellular imaging applications [83]. These UCNPs were first functionalised with PEI and then conjugated with folic acid (FA) to from FA modified $NaYF_4:Yb^{3+},Er^{3+}$ UCNPs. These particles were incubated with human HT29 adenocarcinoma cells and human OVCAR3 ovarian carcinoma cells for 24 hours. Since these cells have abnormally high levels of folate receptors, the FA-$NaYF_4$ UCNPs were able to selectively and specifically target these cancer cells. Under 980 nm excitation, the UCNPs were able to emit green luminescence as has been shown in Fig.1.15. This is one of the first examples of targeted imaging utilising surface modified UCNPs [83].

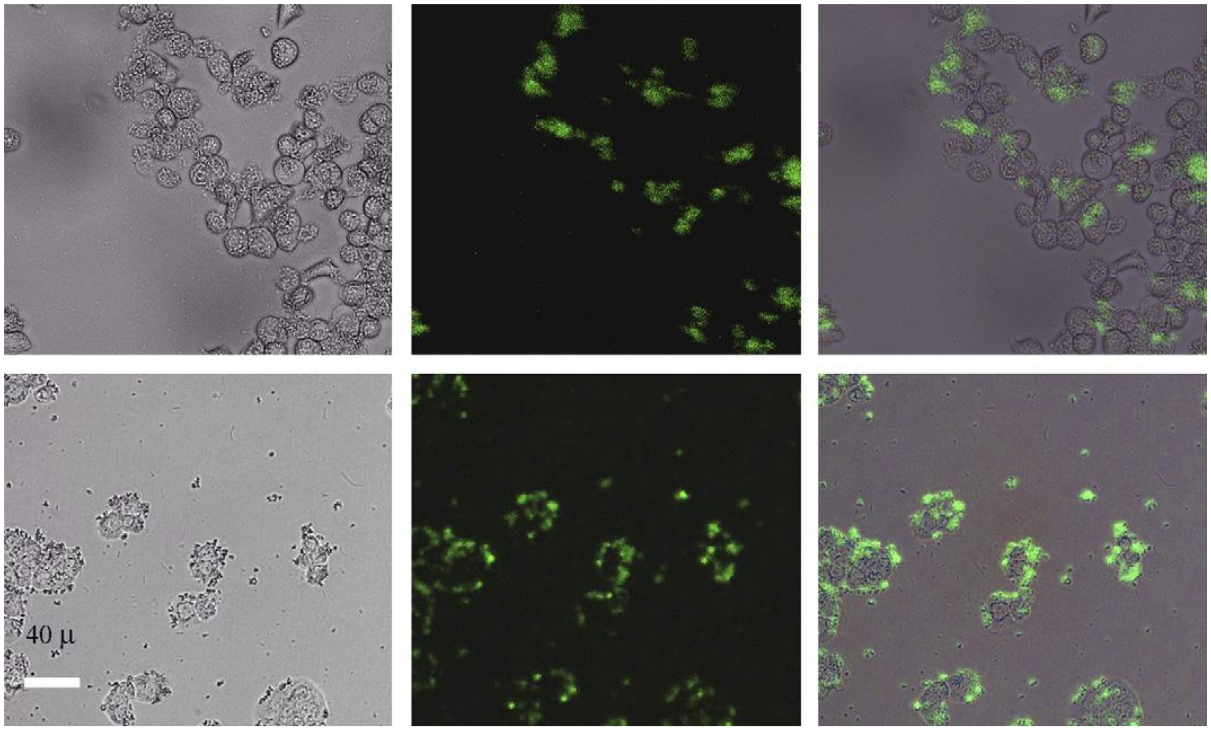

Fig. 1.15: Images showing targeted action of FA-$NaYF_4$:Yb^{3+},Er^{3+} UCNPs on live human ovarian carcinoma cells (OVCAR3, top row) and human colonic adenocarcinoma cells (HT29, bottom row).The left row shows images in bright field, the middle row shows images under confocal excitation and the right row shows an overlap of left and middle rows[83].

High contrast imaging of human pancreatic cancer cells (Panc 1) was reported by Nyk et al [27]. They first modified OA coated $NaYF_4$:Yb^{3+},Tm^{3+} UCNPs with 3-mercaptopropionic acid (MPA). This rendered the UCNPs water soluble. After this, the UCNPs were incubated with Panc 1 cells for 2 hours at 37^{o}C. Under 980nm excitation, the UCNPs attached to the surface of the cells were able to emit IR light at around 800nm as is shown in Fig.1.16. This imaging showed a high contrast, zero autofluorescence and inherent three dimensional localisation features. Moreover, these UCNPs were not toxic as assessed from cell viability assay[27].

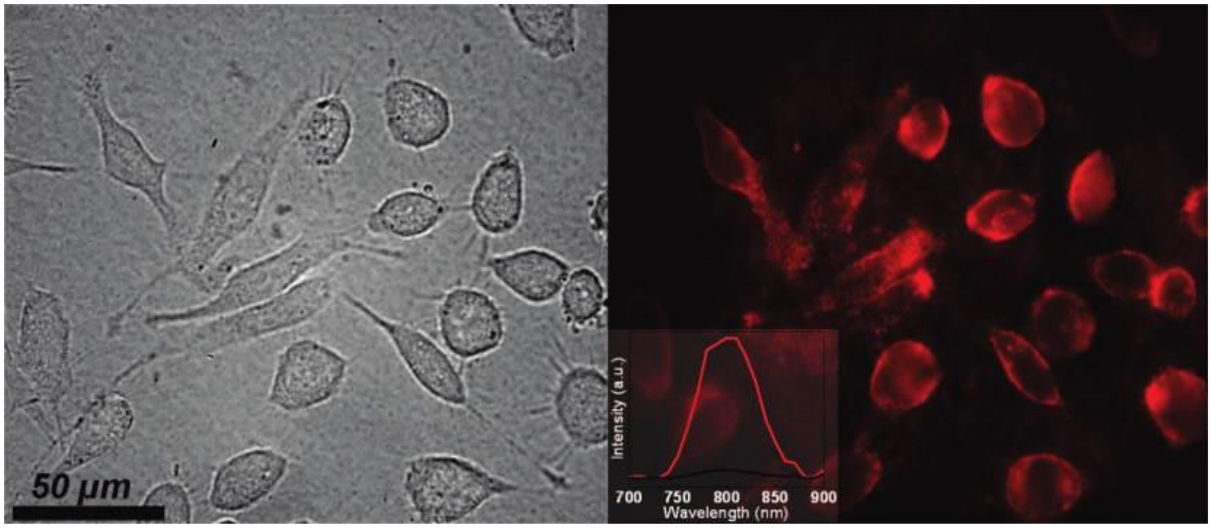

Fig. 1.16: Bright field (left) and fluorescence (right) images of Panc 1 cell incubated with $NaYF_4:Yb^{3+},Tm^{3+}$ UCNPs. The inset shows localised PL spectra under 980nm from cells (red) and background (black)[27]

1.8.3.2 In vivo tissue imaging

Lim et al. reported the use of $Y_2O_3:Yb^{3+},Er^{3+}$ UCNPs for visual imaging of digestive tract of C.elegans worm. The particles were of 50-150nm sizes and were inoculated into live C. elegans. Under 980 nm excitation, distribution of UCNPs in the intestines of the worms can be easily seen (Fig.1.17). Toxicity was not reported, the biocompatibility was good and the worms did not show any defects in their feeding patterns [84].

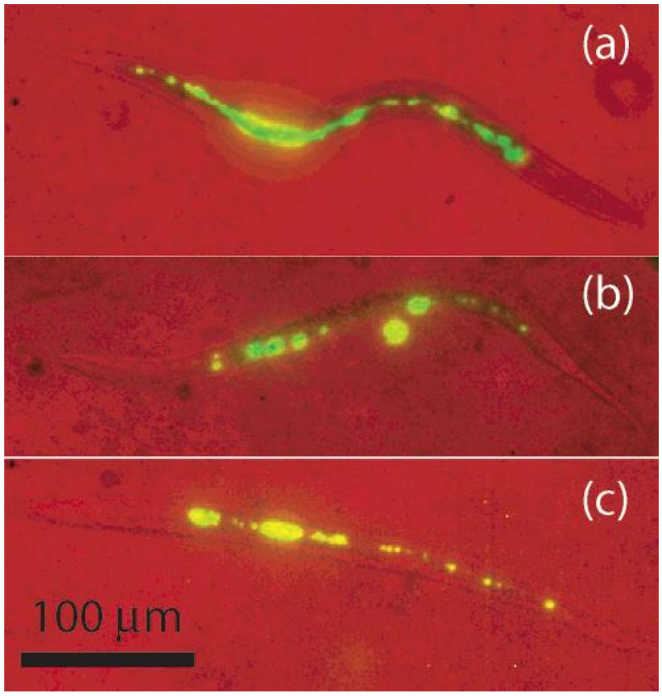

Fig. 1.17: False color two-photon images of C. elegans at 980 nm excitation with red representing the bright field and green for the phosphor emission. The worms were deprived of food over a period of 24 h, showing little or no change at (a) 0 h, (b) 4 h, and (c) 24 h.[84]

Zhang et al. demonstrated in vivo tissue imaging by injecting Wistar rats with 50nm $NaYF_4:Yb^{3+},Er^{3+}$ UCNPs. These UCNPs were injected under the skin in the groin and upper leg regions. It was observed that under 980nm excitation, the UCNPs were detected up to 10 mm beneath the skin which was far deeper than the conventional dots thereby providing new dimensions to tissue imaging at various depths [83]. The images of the procedure are shown in Fig.1.18.

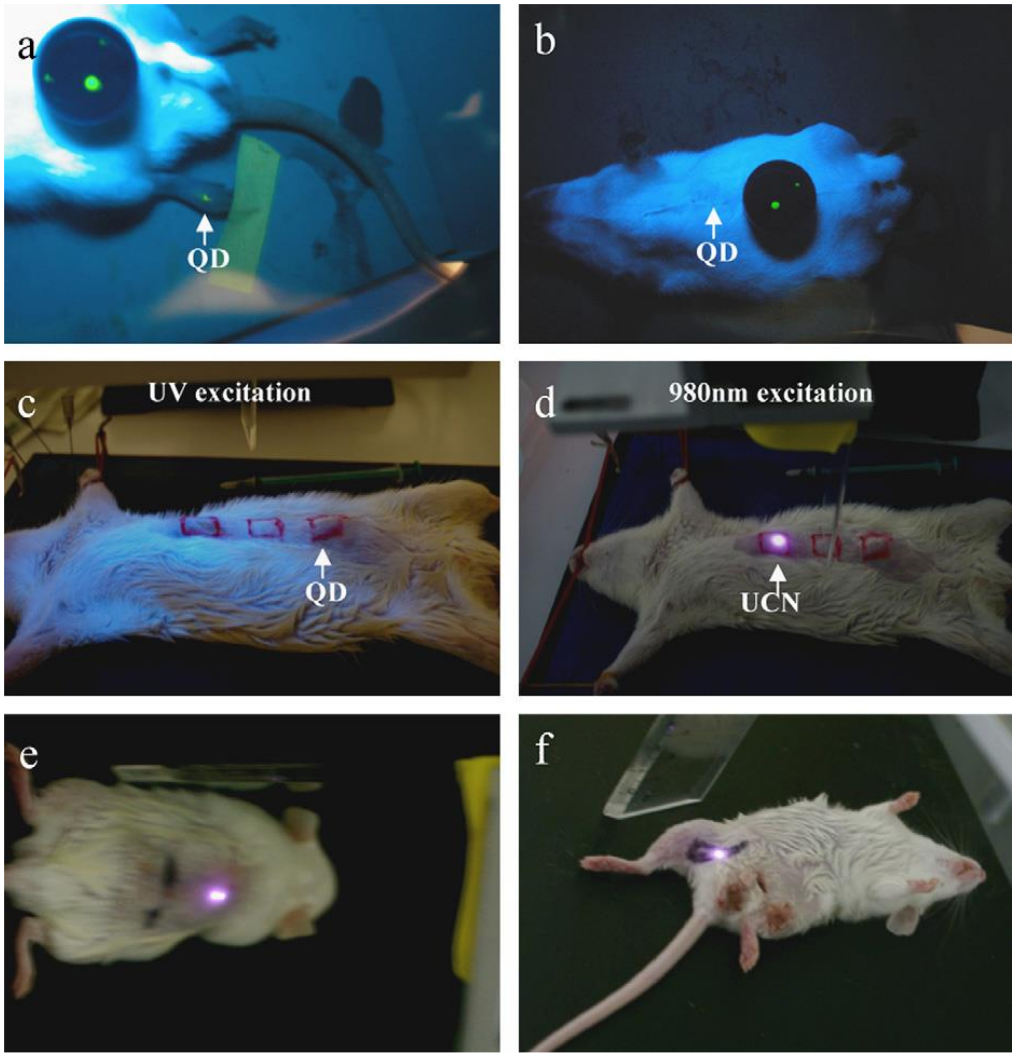

Fig. 1.18: In vivo imaging of rat: quantum dots (QDs) injected into translucent skin of foot (a) show fluorescence, but not through thicker skin of back (b) or abdomen (c); PEI/$NaYF_4$:Yb^{3+}, Er^{3+} nanoparticles injected below abdominal skin (d), thigh muscles (e), or below skin of back (f) show luminescence. QDs on a black disk in (a, b) are used as the control[83].

1.9 Objectives of the current research

- To synthesize RE doped $ALnF_4$ up-conversion nanoparticles ($A=K^+$, $Ln=Gd^{3+}$, $RE=Tb^{3+}$, Er^{3+}, Tm^{3+}) via wet chemical route i.e. RE doped $KGdF_4$ UCNPs
- To perform morphological, luminescent and magnetic studies on the as prepared UCNPs
- To study the energy transfer mechanisms in the UC processes between the sensitizer and activator ions in the UCNP lattice

- To utilise these UCNPs as alternatives to widely researched $NaYF_4$ for bioimaging applications

It is well known that, a host lattice with relatively less phonon energies can act as a good luminescent material. The researchers working in the field of luminescence are looking for new host lattices possessing relatively less phonon energies, low symmetry and high chemical stability. It is evident from the literature that a host lattice containing alkali metal ions are possessing the aforementioned properties and showing relatively good luminescence efficiency [85–87]. Among the alkali host lattices, the potassium systems are less explored when compared with sodium and lithium. This prompted us to take up the present investigation in which the host lattice contains potassium. The main aim behind it is to explore the possible usage of potassium lattice doped with different rare earth ions for better up-conversion luminescence applications.

In the fluoride system $ALnF_4$ [A= alkali ion (Na^+, K^+); Ln=neutral rare earth (Y^{3+}, Yb^{3+}, Gd^{3+})], the role of rare-earth (Ln in our case is Gd^{3+}) is essentially of a network former and most importantly, it allows to dissolve the dopant rare earths to the extremely high concentrations > 25wt%. As such the host Gadolinium (Gd^{3+}) does not play any specific role in the up-conversion and all the up-conversion process is between the dopants Yb^{3+} and activator ions (Er^{3+}, Tb^{3+}, Tm^{3+}). The presence of Gadolinium (Gd^{3+}), being paramagnetic ion, in this host lattice also adds a new dimension as nanoprobes for imaging purposes and shows immense scope for multi-purpose applications: both in up-conversion bio-imaging as well as in Magnetic Resonance Imaging (MRI) applications [88].

Chapter 2: Experimental, Synthesis and Characterisation Techniques

This chapter illustrates the synthesis procedure and the characterisation techniques that were employed to prepare and analyse the $KGdF_4$ UCNPs. To study the morphological, luminescent and magnetic properties of the as prepared nanoparticles, several characterisation procedures were utilised. This chapter highlights the details and working principles of such techniques. Also, details of chemicals and reagents used in the preparation of the UCNPs have also been provided.

2.1 Experimental

Highly pure cubic phase RE doped $KGdF_4$ UCNPs have been prepared via wet chemical route for the purpose of this research. The as prepared UCNPs were subjected to morphological studies to confirm their phase, nature, size and elemental content in the host lattice. Studies like x-ray diffraction (XRD), high resolution transmission electron microscopy (HR-TEM), field emission electron microscopy (FE-SEM) and energy dispersive x-ray analysis (EDAX) were performed for the aforementioned purposes. Luminescent studies like up-conversion and down-conversion were performed on the as prepared UCNPs. Under 980nm NIR excitation, the nanoparticles emit intense up-converted light in the visible region thereby exhibiting the property of up-conversion. Decay kinetics of the UCNPs for the visible emission under 980nm excitation was also studied. All the as prepared samples show high lifetimes thereby enabling their usage even in w-LEDs, lasers and solid state lighting (SSL) applications [89–91]. The samples are also capable of exhibiting the phenomenon of down-conversion as they were able to emit under UV excitation as well. Magnetic properties were studies via electron paramagnetic resonance technique. The presence of paramagnetic gadolinium makes it imperative to study the effect of having a paramagnetic ion in the host lattice.

2.2 Chemicals Used

For the synthesis of RE doped $KGdF_4$ UCNPs, certain highly pure chemicals were used during the synthesis procedure. The details are given in the following table.

Table 0.1: Details of the precursor used in the course of research

S. No.	Name	Chemical Formula	Purity	Company
1.	Potassium Fluoride	KF	99.80%	Fisher Scientific
2.	Gadolinium (III) Acetylacetonate Hydrate	$Gd(acac)_3$	99.99%	Alfa Aesar
3.	Erbium (III) Chloride Hexahydrate	$ErCl_3.6H_2O$	99.99%	Sigma Aldrich
4.	Terbium (III) Chloride Hexahydrate	$TbCl_3.6H_2O$	99.99%	Sigma Aldrich
5.	Thulium (III) Chloride Hexahydrate	$TmCl_3.6H_2O$	99.99%	Sigma Aldrich

The precursors were dissolved in methanol which was of analar grade supplied by Sisco Research Laboratories.

2.3 Synthesis Procedure

A simple wet chemical procedure was utilised to prepare RE doped $KGdF_4$ UCNPs. The chemical equation governing the lattice synthesis is given as:

$$4KF + Gd(acac)_3 \longrightarrow KGdF_4 + 3K(acac) \qquad (2.1)$$

The $KGdF_4$ UCNPs have been prepared by keeping the concentration of the activator ion constant (after optimisation studies) and varying the concentration of sensitizer in the host lattice.

For the purpose of synthesizing the $KGd_{100-x-y}F_4:Yb^{3+}(x\%)/RE^{3+}(y\%)$ UCNPs, gadolinium acetylacetonate [Alfa Aesar, 99.99%, 1 mol%] and potassium fluoride [Fisher Scientific, 4mol%] were used. Ytterbium chloride hexahydrate [x= 5, 10, 15 and 20mol%] [Sigma Aldrich, 99.99%] and RE (erbium/terbium/thulium) chloride hexahydrate [y mol%] [Sigma

Aldrich, 99.99%] were used as rare earth dopants. 10ml of methanol [Sisco research laboratories] was used as a solvent for each precursor. The Gd^{3+} solution and Yb^{3+}/RE^{3+} solutions were added to KF solution drop wise and then aged at 65^0C for three and a half hours under magnetic stirring. After centrifuging at 13,000rpm, the sample was then dried in a vaccum oven at 55^{o}C for 15 hours [92,93]. As a result, cubic phase RE doped $KGdF_4$ UCNPs were formed.

2.4 Characterisation Techniques

2.4.1 Morphological

2.4.1.1 X- Ray Diffraction (XRD)

X-ray diffraction is a standard procedure to determine the phase and crystal structure of the material. X-rays are short wavelength radiations (0.5-2.5Å) that are used as probes for structural analysis of the host material. It was discovered by Max von Laue in 1912 that crystalline materials act as three dimensional diffraction gratings for x-rays whose wavelengths are comparable with spacing of planes in the crystal lattice. Constructive interference between monochromatic X-rays and the crystalline sample gives the x-ray diffraction pattern. A cathode ray tube is utilised to generate monochromatic x-rays which are then collimated and concentrated on the sample. When the conditions of Bragg's law are satisfied, interaction with the sample produces constructive interference and a diffracted ray as is shown in Fig. 2.1

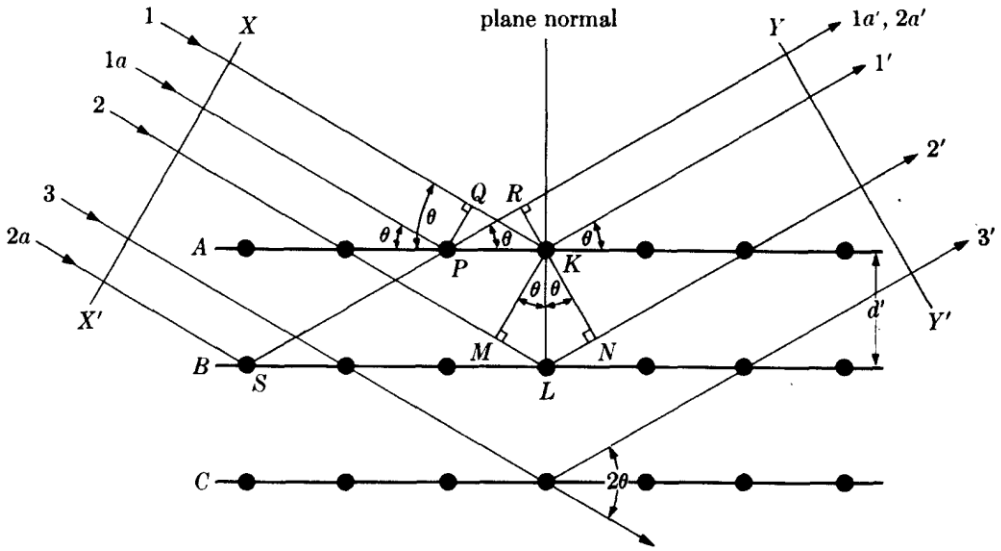

Fig. 2.1: Diffraction of X-Rays by a crystal [94]

Bragg's Law: In a crystalline structure, the atoms are arranged in such a way that they form parallel planes having interplanar spacing d. When the EM radiation is incident on the crystal at different angles, it gets reflected from the surface and from the planes inside the crystal. These reflected beams undergo constructive interference. As is evident from Fig. 2.1, the path difference between rays 1' and 2' scattered by atoms present at K and L is given by

$$ML+LN=d'\sin\theta +d'\sin\theta= 2d'\sin\theta$$

Where θ is the angle of incidence of the EM rays. In the present case, only those rays have been considered for whom the angle of incidence is equal to angle of reflection. Now if λ is the wavelength of the incident radiation then, for constructive interference, path difference is equal to nλ. Therefore,

$$2d'\sin\theta = n\lambda$$

This relation is known as Bragg's Law highlighting the relationship between wavelength of the EM radiation, diffraction angle and lattice spacing of the crystalline sample. The diffracted X-rays are detected, processed and counted. All possible diffraction directions of the lattice are

determined by scanning the sample for all possible 2θ angles due to random orientation of the sample material. The peaks in the diffraction spectra can be converted into d-spacing values which can be used to identify a particular material. This is because, each material has a specific set of d-spacings and this can be determined from standard reference patterns.

A typical x-ray diffractometer setup consists of an x-ray tube, a sample holder and an x-ray detector as is shown in Fig. 2.2. The x-ray tube generates x-rays by bombarding a material target with high energy electrons. A cathode ray tube uses a heating filament to generate electrons which are then accelerated towards a target by applying high potential. When these electrons strike the material target, they dislodge the inner shell electrons of the target thereby producing x-rays. These x-rays consist of K_α and K_β components. K_α in turn consists of $K_{\alpha1}$ and $K_{\alpha2}$ components where $K_{\alpha1}$ has a shorter wavelength than $K_{\alpha2}$ but is twice as intense. These wavelengths are specific to different target materials (Cu, Mo, Fe, Cr). Monochromators are used to produce monochromatic x-rays. Since the wavelengths of $K_{\alpha1}$ and $K_{\alpha2}$ are close to each other, weighted average of both is used. Copper is most commonly used target material with CuK_α=1.5418 Å. These x-rays are directed on the sample which is rotated and diffracted angles of the rays are recorded. When the Bragg's equation is satisfied by the particle geometry and the x-ray, peak in the intensity is recorded. This is recorded by the detector which converts this peak signal into a count rate that can be plotted on a computer. For a typical powder pattern, data is collected at 2θ from 5^o to 70^o.

The XRD analysis is used for:

- Determination of phase of the sample
- Determination of unit cell dimensions
- Determination of particle size and strain
- Determination of lattice parameters a,b and c

The crystallite size is determined using Debye-Scherrer formula:

$$D = \left(\frac{k}{\beta cos\theta}\right) \lambda$$

Where k is the shape factor (0.94), λ is the wavelength of the x-ray used, β is the full width at half maximum (FWHM), θ is the Bragg's angle and D is the crystallite size. It should be noted that crystallite size is not the same as particle size but become equivalent in the nanoscale.

Fig. 2.2: Bruker's X-ray Diffraction D8-Discover instrument

2.4.1.2 High Resolution Transmission Electron Microscopy (HR-TEM)

Tecnai G^2 20 is a highly advanced, state of the art transmission electron microscope offering high productivity, performance and versatility. It is shown in Fig. 2.3. It is best suited for analysing a wide range of advanced materials, soft matter, composites, hybrids, tissues and cellular compounds. The main advantage of TEM over other microscopes is that it can simultaneously give information in real space (imaging mode) and in reciprocal space (diffraction mode).

Fig. 2.3: A Tecnai G^2 20 Transmission Electron Microscope

Basic working principle of TEM is similar to an optical microscope. The only difference is that in a TEM, a focused beam of electrons is used to image and study the structure and composition of the material. An electron beam is produced by an electron gun that is accelerated towards the specimen by applying a positive electric potential. The stream is then focussed using

condenser lenses into a thin, focused and monochromatic beam. This beam strikes the specimen and some part of this beam is transmitted through it. This transmitted beam is again focused using objective lenses to form an image. This image is fed down the column through intermediate and projector lenses which enlarges the image depending upon the magnification. A phosphor screen is used to see the image. As the image strikes the screen, the screen is engendered enabling the user to see the image. The darker areas of the image show thicker or denser regions (from where fewer electrons were transmitted) and lighter areas of the image represent thinner or less dense areas (from where more electrons were transmitted) [95,96].

The main difference between HR-TEM and TEM is the magnification at which the atoms/particles can be resolved. The shape and size of the particles can be seen at lower magnifications but at higher magnifications (for particles having sizes in the range 10-20nm), shape along with lattice plane arrangement can also be seen.

2.4.1.3 Field Emission Scanning Electron Microscope (FE-SEM) and Energy Dispersive X-ray Analysis (EDAX)

ZEISS Evo18 and Oxford INCA 250 VEGA3 TESCAN field emission scanning electron microscopes were used to capture surface morphology and to conduct EDAX analysis on the as prepared samples. The image is provided in Fig. 2.4. This microscope use electrons liberated by a field emission source instead of light to capture the topographical details on the surface or on the entire specimen. Electrons produced from a field emission source are accelerated in a high electrical field gradient. Within the high vacuum column these primary electrons are focussed and deflected by electronic lenses thereby producing a narrow scan beam that strikes the object. The result of this is ejection of secondary electrons from each spot on the object. The angle and velocity of these secondary electrons is related to the surface structure of the object. A detector is used to capture the secondary electrons producing an electronic signal as

a result. This signal is amplified and transformed to a video scan-image that can be seen on a monitor or to a digital image that can be saved and processed further.

Fig. 2.4: ZEISS Evo18 field emission scanning electron microscope

EDAX Analysis in FESEM: It is well known that each atom has a unique number of electrons that reside in specific shells with discreet energies as is shown in Fig. 2.5. The generation of x-rays in a SEM model is a two step process. Firstly, the electron beam strikes the sample and transfers its energy to the atoms in the sample. The electrons in these atoms can utilise this energy to get excited to higher shells of the atom or be knocked off from the atom. Either way, a hole is left behind on the original position of the electron. Secondly, these positive holes then attract negatively charged electrons from the higher shells of the atom. When an atom from the higher shell falls into this shell of lower energy then the energy difference of this transition is released as X-rays. This X-ray has energy that is specific to the energy difference between two shells of the atom and this is unique to each element thus enabling the usage of these X-rays in identifying the elements that are present in the material.

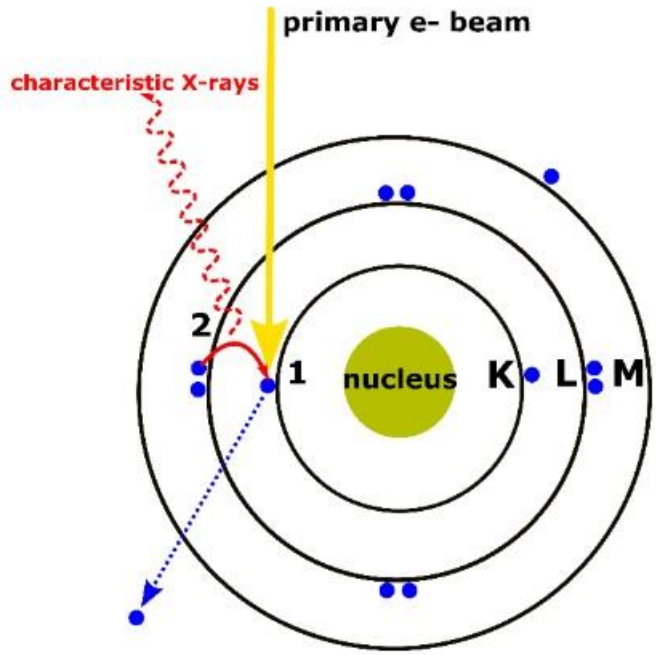

Fig. 2.5: 1) The primary electron beam knocks off the electron in the atom of the material target creating a hole. 2) The position is filled by another electron from higher shell leading to emission of characteristic X-rays

2.4.2 Optical

2.4.2.1 Up-conversion/ Down-conversion luminescence and decay lifetime studies

For recording the UC luminescence of the samples, a Maya 2000 Pro-NIR spectrometer using 980 nm CW laser source on an optical bench was used along with Horiba model QM-8450-11 spectrometer. The image of latter has been provided in Fig. 2.6. Horiba QM-845O-11 was also used to study luminescence from the samples under UV excitation. This setup has an inbuilt variable power 980nm CW laser that was employed to study the power dependent luminescence for $KGdF_4:Yb^{3+}/Er^{3+}$ and $KGdF_4:Yb^{3+}/Tm^{3+}$ samples whereas a neutral density filter was deployed in conjugation with Maya 2000 Pro-NIR spectrometer to study power dependent UC luminescence for $KGdF_4:Yb^{3+}/Tb^{3+}$ UCNPs.

For photoluminescence decay measurements, mechanical chopper (12 Hz), lock-in amplifier, digital storage oscilloscope and a monochromator (Acton SP 2300) were employed.

Fig. 2.6: Horiba model QM-8450-11 spectrometer

2.4.3 Magnetic Characterization

Electron paramagnetic resonance (EPR) studies were performed using a Bruker model EMX MicroX setup at microwave frequency of 9.665 GHz with power being set as 6.371 mW. The image of the setup is provided in Fig. 2.7.

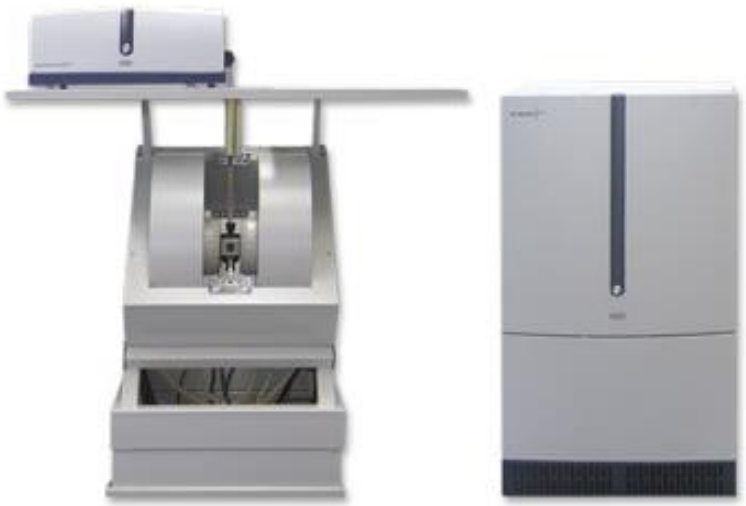

Fig. 2.7: Bruker EMX MicroX EPR setup

EPR is the only technique that detects unpaired electrons unambiguously. Also, EPR can identify the paramagnetic species that are present in the host lattice. Since EPR samples are very sensitive to local environments, this technique helps ion understanding the molecular structure near the unpaired electron.

EPR is a magnetic resonance technique very similar to NMR (Nuclear Magnetic Resonance). However, instead of measuring the nuclear transitions in the sample, transitions of unpaired electrons in an applied magnetic field are detected. The electron has “spin”, which gives it a magnetic property known as a magnetic moment. When an external magnetic field is applied, the paramagnetic electrons can either orient in a direction parallel or antiparallel to the direction of the magnetic field thereby creating two distinct energy levels for the unpaired electrons. Measurements can be noted as these electrons are driven between the two levels. At first, more electrons will be present in the lower energy level (i.e., parallel to the field) than in the upper level (antiparallel). By using a fixed frequency of microwave irradiation some of the electrons in the lower energy level are excited to the upper energy level. In order for the transition to occur, an external magnetic field at a specific strength must be supplied, such that the energy level separation between the lower and upper states is exactly matched by the microwave frequency. The condition where the magnetic field and the microwave frequency match to produce an EPR resonance (or absorption) is known as the resonance condition.

Chapter 3: Morphological and Luminescence Studies on $KGdF_4:Yb^{3+}/Tb^{3+}$ Up-Conversion Nanophosphors

$KGdF_4$ up conversion nanophosphors doped with varying concentrations of Ytterbium (Yb^{3+}) and co-doped with Terbium (Tb^{3+}) ions were synthesized using a wet chemical route. Morphological studies like XRD and TEM were carried out on the as prepared nanoparticles. The size of the UCNPs was found to be of the order of 6-8nm using Debye Scherrer Formula. Under 980nm CW laser excitation, the as prepared UCNPs emit intense Up-Converted green light at 545nm ($^5D_4 \rightarrow {}^7F_5$). The energy transfer for this transition between the sensitizer (Yb^{3+}) and activator (Tb^{3+}) ions during the Up-conversion (UC) process was found to be through Cooperative Energy Transfer (CET) mechanism. UC emission was also observed from $^5D_3$ to $^7F_3$ level of Tb^{3+} ions whose intensity was found to be increasing with Yb^{3+} ion concentration due to non-radiative energy transfer up-conversion (ETU) from a single excited Yb^{3+} ion, which is not involved in CET. The experimental lifetimes of 545nm emission under 980nm excitation for the as prepared UCNPs was observed to be in the range of 0.1-0.4ms. Relatively higher experimental lifetimes and ability to emit intense visible green emission under NIR excitations allow us to contemplate that these UCNPs can be the prospective host lattices that could be used for the present day bio-imaging and targeted drug delivery applications. The results of this study have been published in **Materials Chemistry and Physics, 219 (2018) 13-21**

3.1 Introduction:

The field of UCNPs has seen tremendous advances in recent decade. These nanoparticles find their usage in three dimensional display technologies [97], solar cells [98,99], bio-imaging [27,100] and targeted drug delivery [101,102]. Conventional methods employed in bio-photonic applications use organic dyes and quantum dots that have many shortcomings [103,104]. Bio-imaging is carried out through the development of fluorescent nanoparticles that are conjugated with certain specific biomolecules that produce detectable fluorescent signals under excitation from an external energy source. These signals are then used for understanding the dynamics of the biological interactions at molecular level. Now, as a general requirement, the fluorescent probe must be nontoxic, biocompatible, resistant to photo bleaching and should possess high fluorescent efficiency with physical and chemical stability. Conventional organic dyes used for bio-labeling and bio-imaging, despite having the aforementioned properties, have their fair share of drawbacks. They are susceptible to photo bleaching and chemical degradation along with having a narrow absorption and broad emission spectra which limits their detection. With advances in nanotechnology, quantum dots were developed which, despite having good photo stability and broad UV absorption and narrow emission, find less usage due to inherent cytotoxicity and chemical instability. Above all, the excitation of these bio labels involves the usage of high energy UV/X-Ray radiation which has serious disadvantages such as low light penetration depth, damage or even death of biomolecules due to long time irradiation and low signal to noise ratio (SNR) due to auto fluorescence from biological samples in UV short wavelength regions [13,105]. Therefore it is highly essential to develop efficient fluorescent probes that take into due consideration of the above mentioned drawbacks. Recent research developments in the area of RE doped fluoride based UCNPs show promising results. Up-conversion is a nonlinear optical process in which low energy NIR radiation is converted into high energy visible radiation. Development of such

RE doped UCNPs has immense advantages such as improved SNR due to absence of auto-fluorescence, deeper NIR light penetration and less damage to biological samples. Also, these are cost effective, non-toxic and exhibit high physical and chemical photo stability. RE doped $ALnF_4$ ($A=Na^+$, K^+; $Ln=Y^{3+}$, Gd^{3+}, La^{3+}, Lu^{3+}) have gained so much of importance due to their ability to exhibit emission in the visible region under NIR excitation. Since they are fluoride based, they have low phonon energies that help in increasing the luminescence intensity by reducing the non-radiative energy losses. Also, they are averse to photo bleaching and have a high SNR [13,106,107].

In this chapter synthesis of potassium gadolinium fluoride ($KGdF_4$) UCNPs doped with Yb^{3+} ions (5%, 10%, 15% and 20 mol%) and co-doped with Tb^{3+} ions (3 mol%) via wet chemical route [92] has been reported. These particles have a size less than 9nm. The motivation behind developing this compound was to explore some other alkali ion based lattices apart from Na^+ ones that could open up myriad possibilities in the studies on UC spectra and its energy transfer dynamics. The presence of gadolinium (Gd^{3+}) in this host lattice only adds a new dimension for the prospective usage of this lattice as nanoprobes for imaging purposes due to the fact that Gd^{3+} is paramagnetic and has immense scope in Magnetic Resonance Imaging (MRI) applications as a T1/T2 contrasting agent [88]. Thus RE ions doped $KGdF_4$ lattice is a multifunctional single phase compound (i.e., exhibiting paramagnetism and up-/down-conversion). The $KGdF_4$ lattice is relatively less explored. Yang et al. reported hydrothermal synthesis of Ln^{3+} co-doped $KGdF_4$ via hydrothermal route that yielded UCNPs of nearly 12nm size [108]. Now, Wang et al. had already reported that CaF_2:Yb^{3+}/Er^{3+} lattice having a size less than 10nm has a more efficient UC emission than the conventional $NaYF_4$: Yb^{3+}/Er^{3+} lattice having larger sizes [109]. This was another reason to explore and study another fluoride based lattice with the particle size less than 10nm. This synthesis technique resulted in UCNPs having

sizes less than 9nm. Such small sizes of UCNPs are well suited for their usage as imaging probes [110].

3.2 Experimental:

For the experiments, $Gd(acac)_3.xH_2O$ [Alfa Aesar,99.99%,1 mol%] and KF [Fisher Scientific, 4mol%] were used. For doping, $YbCl_3$ [5,10,15 and 20mol%] [Sigma Aldrich, 99.99%] and $TbCl_3$ [3mol%] [Sigma Aldrich, 99.99%] were used. Each of the reactants were separately dissolved in 10ml of methanol [Sisco Research Laboratories]. The Gd^{3+} solution was added drop wise to KF solution first, followed by adding RE solutions drop wise at 65^0C. This combined solution was stirred magnetically for three and a half hours [14, 20-21]. The resulting solution was centrifuged at 13,000rpm and washed with methanol thrice. Powder XRD patterns were recorded using PANalytical X-Ray diffractometer employing Cu K_α(λ=1.5418 Å). UC studies were carried out using Maya 2000 Pro-NIR spectrometer using 980nm CW laser source. Luminescence studies under UV excitation were carried out using Shimadzu RF 5301c spectrometer. For PL decay measurements, mechanical chopper (12 Hz), lock-in amplifier, digital storage oscilloscope and a monochromator (Acton SP 2300) were employed.

3.3 Results and Discussion:

3.3.1 Morphological Studies

3.3.1.1 XRD and TEM Analysis

Fig. 3.1(a) shows the XRD patterns of an un-doped $KGdF_4$ and $KGd_{(100-x-y)}F_4:Yb^{3+}$(x=5,10,15 and 20%)/$Tb^{3+}$(y=3%) samples. The XRD patterns shown in Fig. 3.1(a) are not matching well with the standard data (JCPDS=033-1007) of orthorhombic $KGdF_4$, rather they are matching well with cubic $NaGdF_4$ data (JCPDS=27-0697) [110,111]. This means that $KGdF_4$ samples are exhibiting similar cubic phase as that of $NaGdF_4$ [110–112]. The space group of $KGdF_4$ as

compared with the standard JCPDS (27-0697) data was found out to be Fm3m. It is seen that the diffraction peaks are slightly shifted towards the lower degree which is caused by substitution of smaller radii Na^{+} ions by the larger radii K^{+} ions in the fluoride host lattice [111,112]. The sizes of the as prepared samples were calculated using the Debye-Scherrer equation and were found to be in the range of 6-8nm. The estimated cubic lattice parameter for an un-doped sample is a=5.731 Å and for $KGdF_4:Yb^{3+}$ (x%)/Tb^{3+} (3%) (x=5, 10,15 and 20%) samples respectively are a=5.724, 5.710, 5.710 and 5.704 Å . The decrease in the lattice parameters with increase in Yb^{3+} concentration can be justified as sites of Gd^{3+} ions having larger ionic radii are being selectively replaced by the Yb^{3+} ions [113]. Fig. 3.1(b) shows the TEM image recorded for $KGdF_4:Yb^{3+}$(20%)/Tb^{3+}(3%) sample. As seen in the image, the particles are agglomerated and the average grain size was estimated to be nearly 6nm which is approximately equal to the results from XRD analysis.

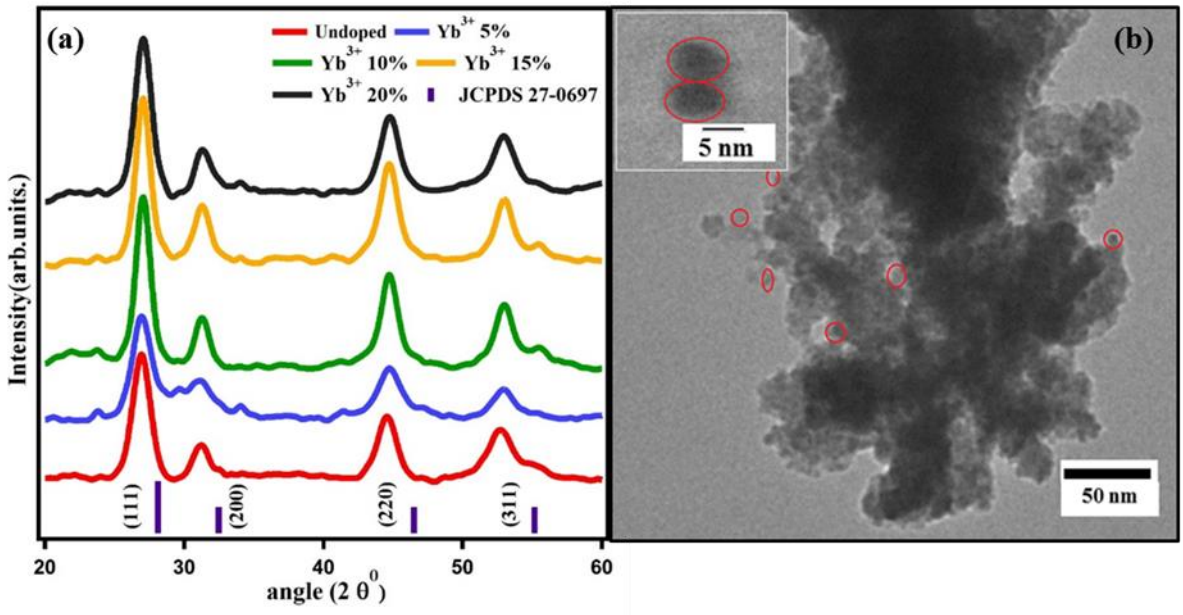

Fig. 3.1: (a) XRD analysis of an un-doped $KGdF_4$ and doped $KGdF_4:Yb^{3+}$(x=5, 10, 15 and 20%)/Tb^{3+} (3%) samples. Data peaks of standard JCPDS 27-0697 are also given for reference (b) TEM Image of $KGdF_4:Yb^{3+}$ (20%)/Tb^{3+} (3%) sample.

3.3.2 Photoluminescence (PL) Studies

3.3.2.1 Optimization of Tb^{3+} ion concentration in $KGdF_4$ Lattice

To check for the optimum concentration of Tb^{3+} ion that would give maximum emission intensity for PL studies on the as prepared $KGdF_4$ lattice, certain $KGdF_4$ lattices with varying concentrations of Tb^{3+} ions (1%, 2%, 3% and 3.5%) were prepared. Under 384 nm excitation, the emission spectra for all the samples were recorded and plotted as shown in Fig. 3.2. It was seen that, concentration quenching occurred in the sample containing 3.5 mol% of Tb^{3+} i.e., $KGdF_4$:Tb^{3+} (3%) sample emitted with maximum intensity. Therefore, for the purpose of research studies, it was decided to prepare $KGdF_4$ host lattices keeping concentration of Tb^{3+} fixed at 3 mol% and varying the concentration of sensitizer Yb^{3+} to study the effects on the energy transfer mechanisms.

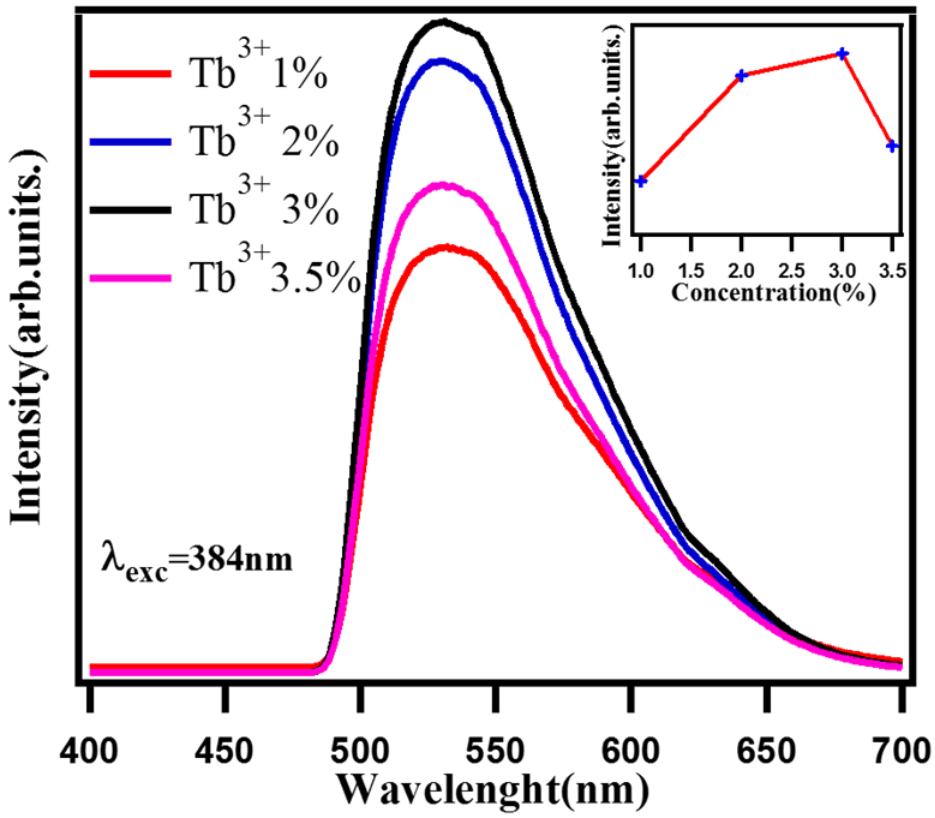

Fig. 3.2: Optimization of Tb^{3+}: emission spectra recorded under 384nm excitation

3.3.2.2 NIR Up-Conversion studies

Fig. 3.3 shows the UC spectra of the as prepared samples under 980nm CW laser excitation at 1 Watt of power. All the samples under investigation are exhibiting 3 peaks due to transition from $^5D_4$ level centered at around 545nm ($^5D_4 \rightarrow {}^7F_5$), 584nm ($^5D_4 \rightarrow {}^7F_4$) and 622nm ($^5D_4 \rightarrow {}^7F_3$) and one peak at 472nm ($^5D_3 \rightarrow {}^7F_3$). Among them, the green emission observed at 545nm is the most intense one. The intensities of the peaks are seen increasing with increase in the concentration of sensitizer Yb^{3+} ions [114]. UC Emission was also observed from higher $^5D_3$ level. The intensity of such transition is very small and is hardly visible for lower doping concentration of sensitizer ion but increases with increasing concentration of Yb^{3+} ions. Also, the UC band at 545nm exhibits some splits. This is the outcome of the crystal field splitting of the transition due to high crystallinity of the host lattice and successful substitution of Yb^{3+} and Tb^{3+} ions in the Gd^{3+} sites of the host lattice [115].

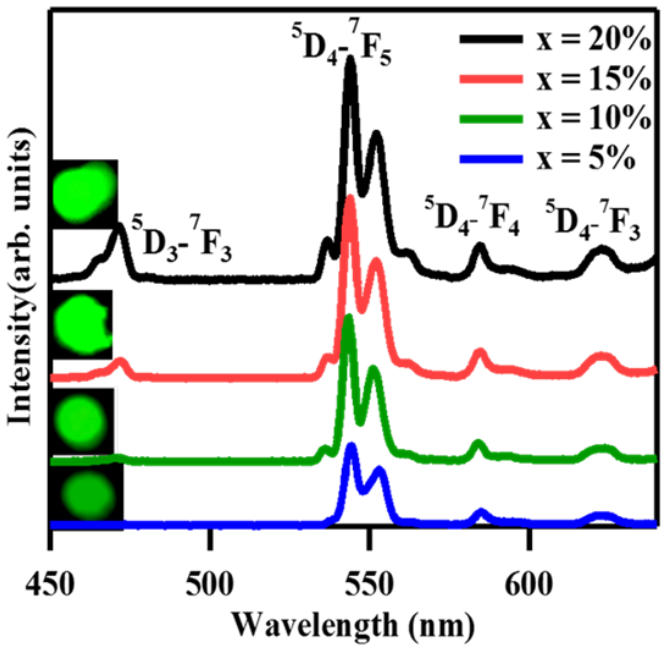

Fig. 3.3: UC Spectra of $KGdF_4$:Yb^{3+} (x=5, 10, 15 and 20%)/Tb^{3+} (3%) samples under 980nm excitation. Inset pictures show the actual photographs of intense green luminescence from the as prepared samples

3.3.2.3 Power dependence studies

To check the power dependence of the intensity of the transitions, the samples were excited under 980nm CW laser by varying the power of the laser source. Fig. 3.4 shows the UC spectra at varying powers for $KGdF_4:Yb^{3+}$(x=5, 10, 15 and 20%)/Tb^{3+} (3%) samples.

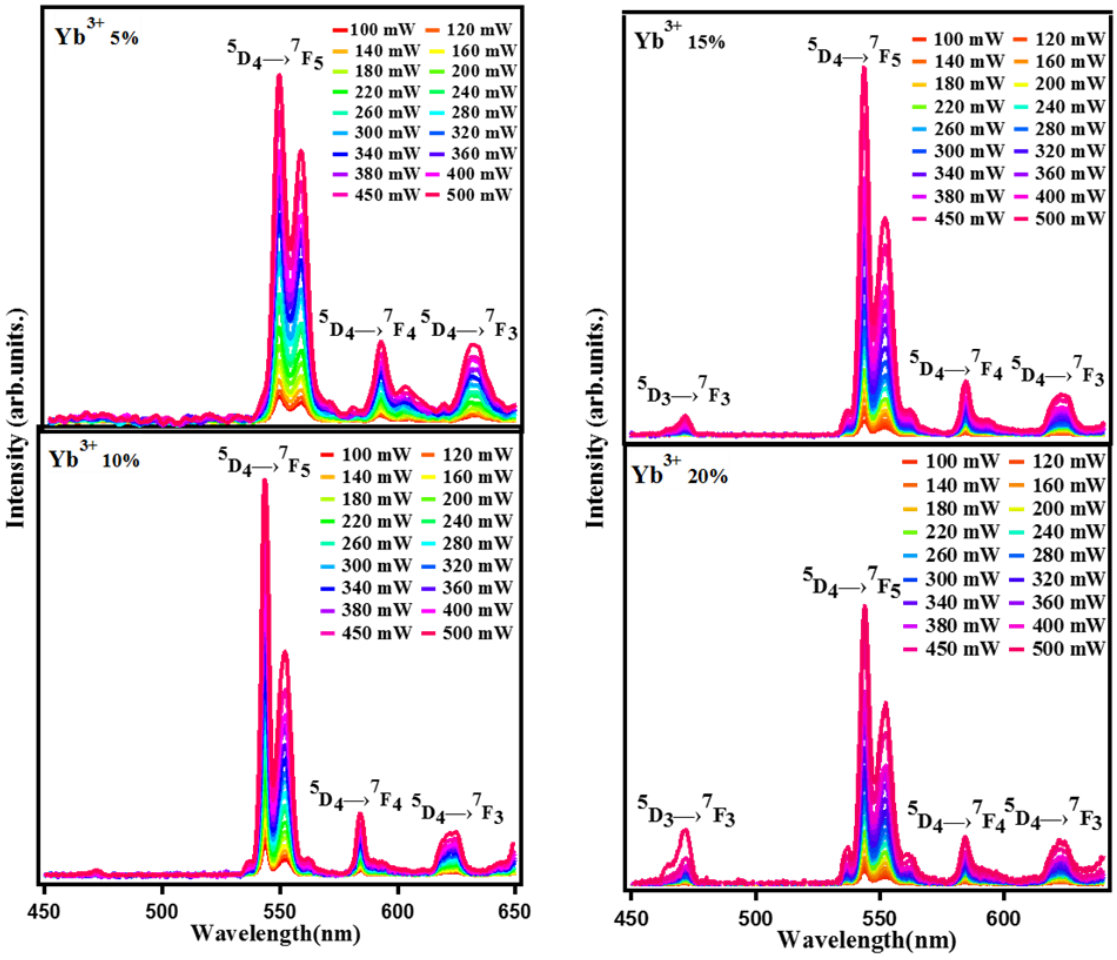

Fig. 3.4: UC Spectra of $KGdF_4:Yb^{3+}$ (x=5, 10, 15 and 20%)/Tb^{3+} (3%) samples under varying powers of 980nm CW laser source.

For the $^5D_4 \rightarrow {}^7F_5$ transition, the power dependence of the intensity for each sample was noted and plotted on a double logarithmic scale to understand the mechanism of energy transfer involved via population of the $^5D_4$ energy level of Tb^{3+} ions [116]. The data points obey the power law i.e.

$$I_{UC}=(I_{IN})^{n} \quad (3.1)$$

where I_{UC} is the up-conversion intensity and I_{IN} is the incident pump power. The exponential "n" here is the number of NIR photons absorbed by Yb^{3+} ions which subsequently transfer the energy to Tb^{3+} ions thereby generating visible photons by de-excitation to ground state. Fig. 3.5 shows the log I vs log P plots for the samples. It can be seen that the slope for each of the plots is close to 2. So we can deduce that NIR excitation under 980nm laser giving 545nm green emission is a two photon excitation process. Some of the observed slopes are less than 2 because of the energy loss that takes place when the NIR photons enter the crystals along with non-luminous relaxation that causes a difference between the absorbed and emitted energy [115].

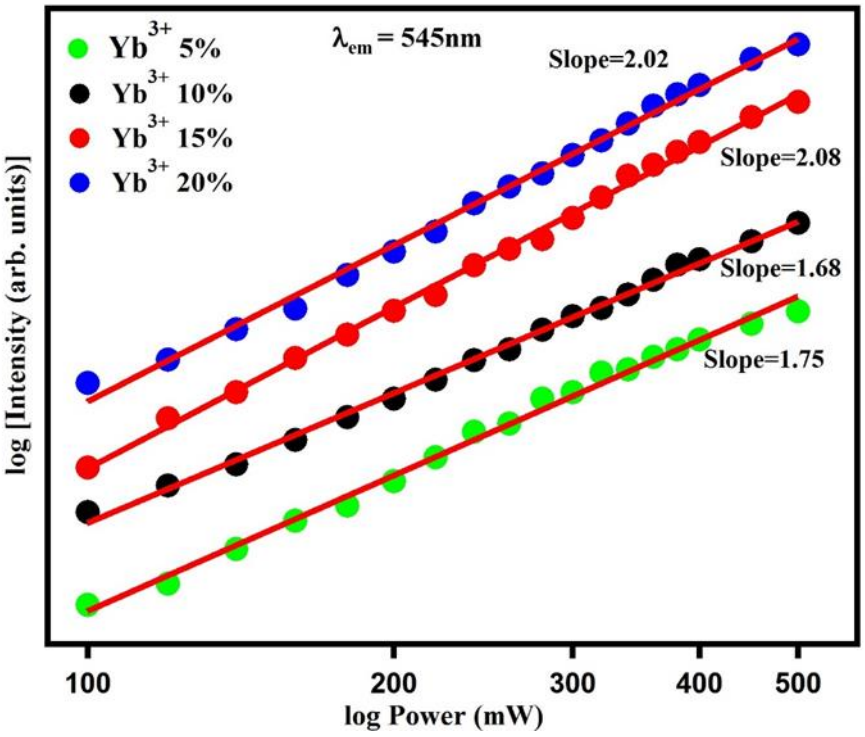

Fig. 3.5: Power Dependence of $KGdF_4:Yb^{3+}$ (x=5, 10, 15 and 20%)/Tb^{3+} (3%) samples: log I vs log P graph recorded for green transition of Tb^{3+} ions in the lattice under 980nm excitation

There is no energy level in Tb^{3+} that matches the excited $^2F_{5/2}$ level in Yb^{3+}. Cooperative Energy Transfer (CET) is the proposed energy transfer mechanism here because of the fact that the energy gap between the $^5D_4$ and $^7F_6$ levels of Tb^{3+} is nearly double the separation between $^2F_{7/2}$ and $^2F_{5/2}$ levels in Yb^{3+} ions. Two NIR pump photons (980nm) excite two Yb^{3+} ions from ground state $^2F_{7/2}$ level to excited $^2F_{5/2}$ level. These two Yb^{3+} ions form a virtual state by interacting with each other cooperatively. This is followed by an emission of a photon at 488nm wavelength [117]. Now the $^5D_4$ state of Tb^{3+} ion nearly matches with this virtual state of Yb^{3+} ions i.e., they lie at around 21,000cm^{-1} (nearly 488nm). The energy transfer takes place from a pair of excited Yb^{3+} ions to neighboring one Tb^{3+} ion thereby populating the $^5D_4$ level and producing the visible $^5D_4 \rightarrow {}^7F_J$ (J=5,4,3) luminescent transitions. The energy transfer processes and mechanism are expressed as follows: $Tb^{3+}(^7F_6) + Yb^{3+}(^2F_{5/2}) + Yb^{3+}(^2F_{5/2}) \rightarrow Tb^{3+}(^5D_4) + Yb^{3+}(^2F_{7/2}) + Yb^{3+}(^2F_{7/2})$.

A single Yb^{3+} ion that is not taking part in CET can excite a Tb^{3+} ion from $^5D_4$ state to $^5D_1$ state through excited state absorption (ESA) and/or a non-radiative energy transfer up-conversion (ETU). This process can be summed as: $Tb3^+(^5D_4) + Yb^{3+}(^2F_{5/2}) \rightarrow Tb^{3+}(^5D_1) + Yb^{3+}(^2F_{7/2})$.

This excited Tb^{3+} ion then relaxes to the $^5D_3$ metastable state non-radiatively leading to the observed weak transition peak at $^5D_3 \rightarrow {}^7F_3$. The intensity of this transition was seen to be increasing with increase in the concentration of Yb^{3+} ions as is evident from the experimental data and figures. This observation confirms the fact that, ETU is involved in population of the $^5D_3$ level [116]. Fig. 3.6 shows the schematic energy level diagram and possible energy transfer processes.

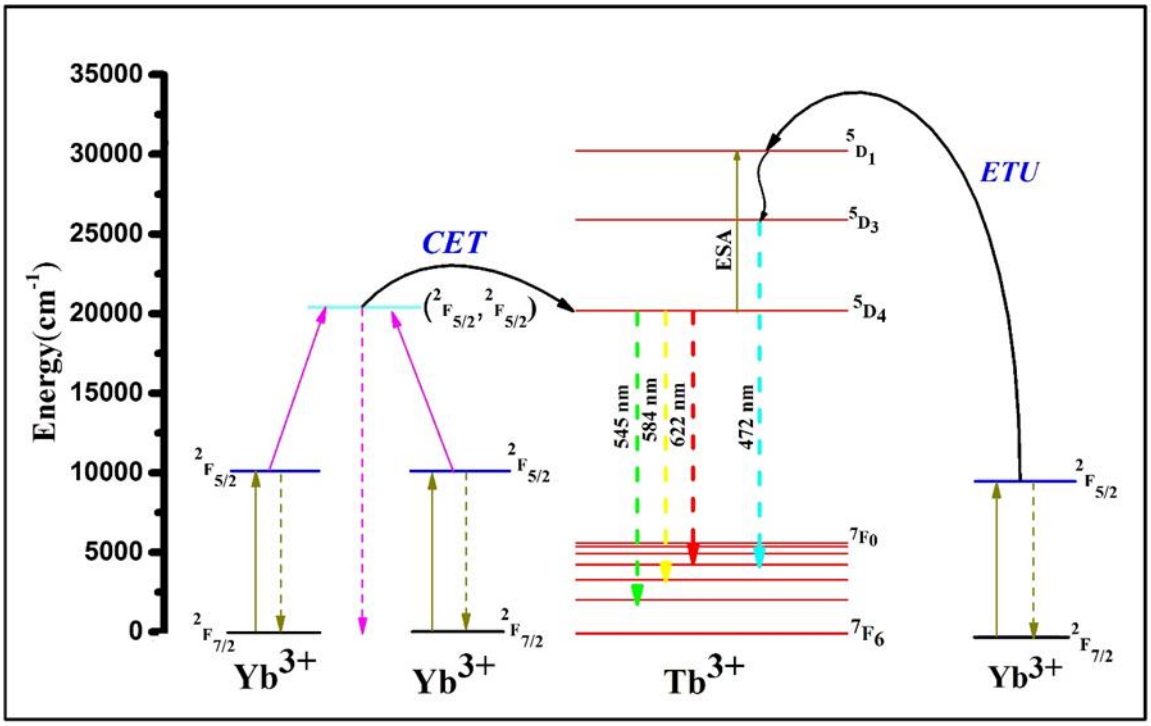

Fig. 3.6: Schematic energy level diagram for the possible energy transfer mechanism between Yb^{3+} and Tb^{3+} ions during UC process.

3.3.2.4 Decay Kinetics

Fig. 3.7 shows the decay kinetics corresponding to the $^5D_4 \rightarrow {}^7F_5$ transition for the as prepared $KGdF_4$ samples. The decay curves were well fitted to a double exponential function [114,118]

$$y = A_1 * exp(-x/t_1) + A_2 * exp(-x/t_2) + y_0 \qquad (3.2)$$

The decay can be fitted to a single exponential function if there are no interactions present between RE ions that emit. But if ion-ion interactions are present along with energy transfer, then the resulting emission consists of two components i.e., slow and fast decay components. Since the curves fitted well to a double exponential function, it can be concluded that there is a different non-radiative decay for the lanthanide ion. These ions might be at the surface of the particles or near to it or in the core of the particles. It might be possible that there exist more than one site where the dopant ion can be accommodated in the $KGdF_4$ lattice. The decay time

decreases from 0.387 ms (Yb^{3+} =5%) to 0.076 ms (Yb^{3+}=20%). This quenching of the $^5D_4$ level could be caused due to the increased Tb^{3+}-Yb^{3+} interactions as due to increase in concentration of Yb^{3+} ions, more ions are in close proximity of each other. In other words, there exists a probability of backward energy transfer from Tb^{3+} to Yb^{3+} (down conversion). Such high lifetimes of $^5D_4$ level of Tb^{3+} ions in milliseconds makes these UCNPs suitable for usage in display devices and lighting applications [114].

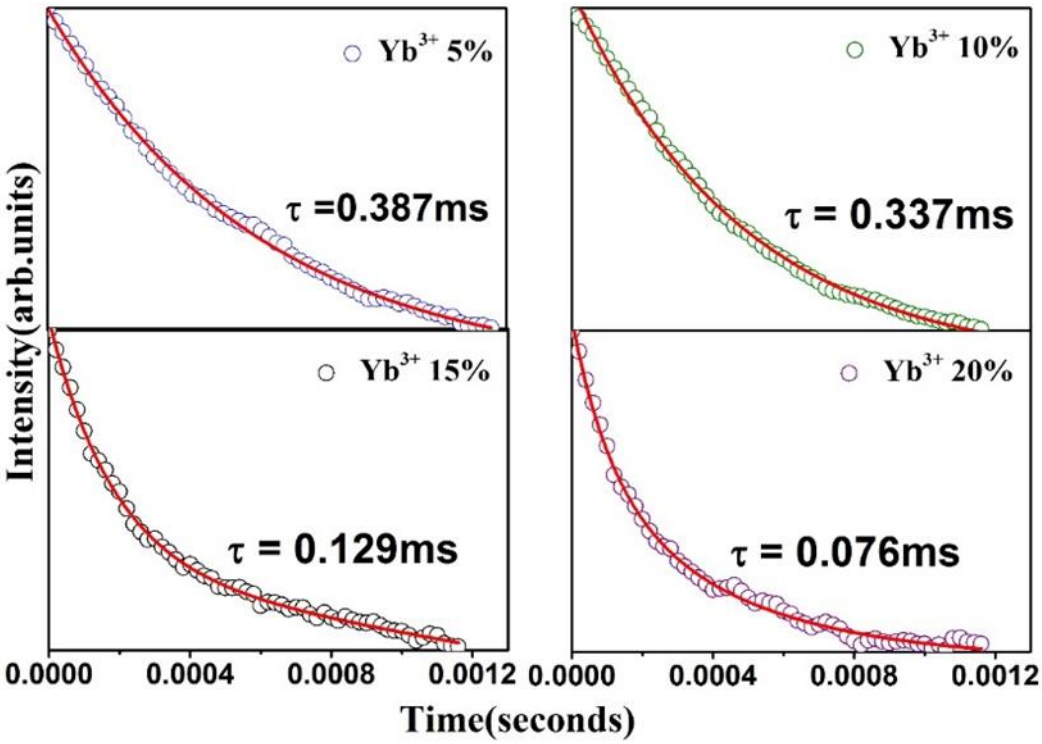

Fig. 3.7: Decay curves along with the function fitting of as prepared samples at 545nm emission under 980nm CW laser excitation

3.3.2.5 Photoluminescence Studies under UV excitation

The excitation spectra of $KGdF_4$:Yb^{3+}(10%)/Tb^{3+}(3%) sample at emission wavelength λ_{em}=545nm is shown in Fig. 3.8(a). There is a peak at 272nm which can be attributed to intra $4f^8$ transition from the $^7F_6 \rightarrow {}^5I_8$ levels [116,119]. Uneven mixing of the 5d wave function into

the 4f function is the cause for these transitions. Due to this reason, some amount of opposite parity function is produced thereby resulting in some partially allowed intra-configurational transitions [55].

Emission spectra under UV excitation (λ_{exc}=292nm) of the as prepared samples were recorded and presented in Fig. 3.8(b). The results show three broad peaks corresponding to $^5D_3 \rightarrow {}^7F_3$ (468nm), $^5D_4 \rightarrow {}^7F_6$ (490nm) and $^5D_4 \rightarrow {}^7F_5$ (545nm). The $^5D_4 \rightarrow {}^7F_5$ transition is the strongest among all the transitions because of the fact that is has the highest probability to occur (for electric and magnetic dipole induced transitions) [114,120]. The intensity of $^5D_3$ transition is weak for lower doping Yb^{3+} ions but increases with increasing the concentrations of the same. Due to intense green emission under UV excitation, these particles can also be used as fluorescent probes for various photonic applications [18,46].

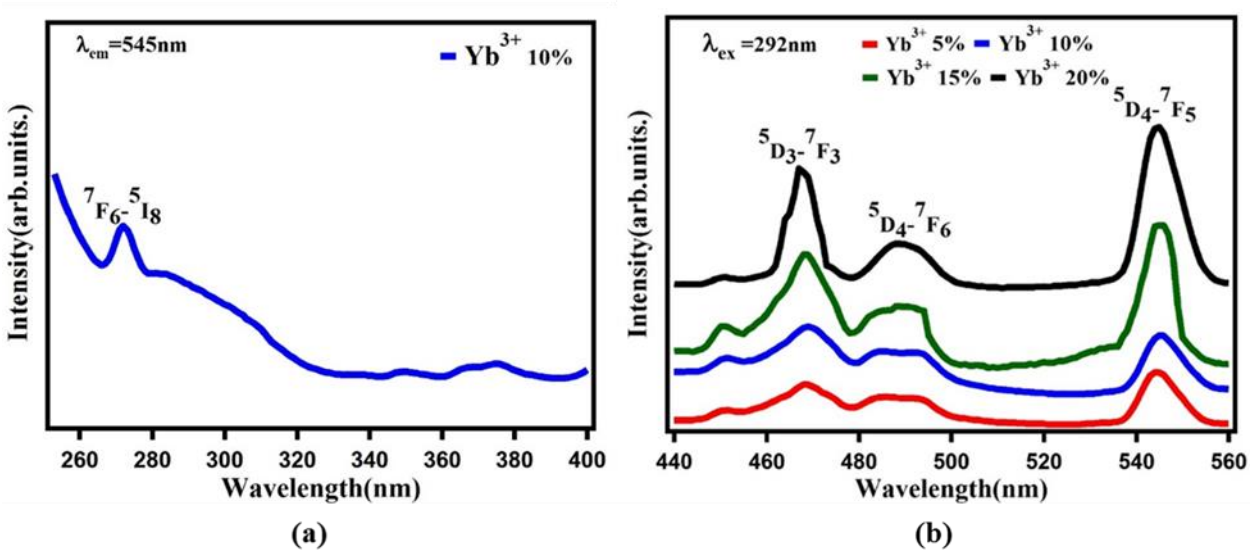

Fig. 3.8: (a) Excitation Spectra at 545nm emission wavelength for $KGdF_4:Yb^{3+}$ (10%)/Tb^{3+} (3%) (b) Emission Spectra of $KGdF_4:Yb^{3+}$ (x=5, 10, 15 and 20%)/Tb^{3+} (3%) samples under 292nm UV excitation

The Commission Internationale de L'Eclairage (CIE) chromaticity diagram for the 545nm emission under 980nm excitation is given in Fig. 3.9. It is clear from the CIE diagram that the

coordinates lie in the intense green region. The CIE Coordinates along with the decay lifetimes of the samples at 545nm emission under 980nm CW laser excitation are given in Table 3.1.

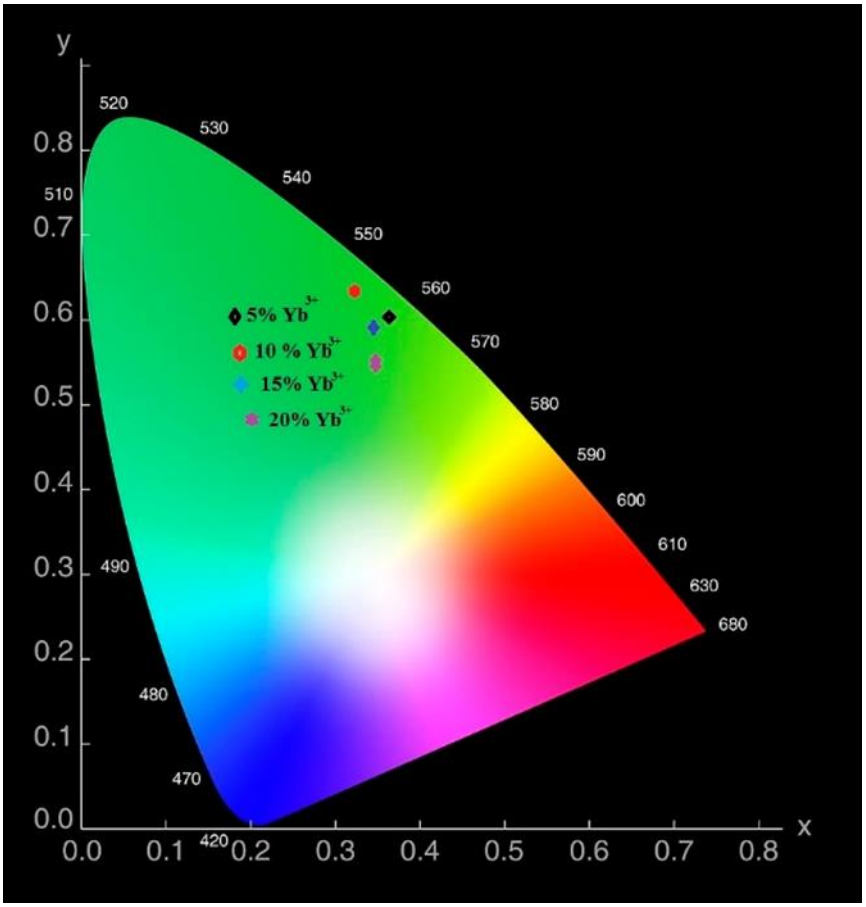

Fig. 3.9: CIE Chromaticity Diagram for NIR UC studies on $KGdF_4:Yb^{3+}$ (x=5, 10, 15 and 20%)/Tb^{3+} (3%) samples

Table 0.1: Lifetimes and CIE Coordinates of the as prepared $KGdF_4$ samples for UC Studies under 980nm excitation

Concentration of Yb^{3+}	CIE Chromaticity Coordinates		Lifetime(ms)
	X	Y	
5%	0.37	0.71	0.387
10%	0.34	0.63	0.337
15%	0.35	0.59	0.129
20%	0.34	0.54	0.076

3.4 Conclusions:

Cubic phase un-doped and $KGd_{(100-x-y)}F_4:Yb^{3+}$(x=5,10,15 and 20%)/$Tb^{3+}$(y=3%) were prepared using a wet chemical route . XRD results show that the samples form in a cubic crystalline phase of cubic $NaGdF_4$ having a size in the range of 6-8nm. NIR and UV luminescent studies were carried out on the samples. The samples show intense green emission centered at around 545nm due to $^5D_4 \rightarrow {}^7F_5$ transition of Tb^{3+} ion. To explain the up-conversion processes in the as prepared samples, CET and ETU processes have been proposed as the possible energy transfer mechanisms between Yb^{3+} and Tb^{3+} ions. Decay kinetics of the samples were also studied for $^5D_4 \rightarrow {}^7F_5$ transition of Tb^{3+} under 980nm excitation. Since the as prepared samples have high lifetimes and also emit intense visible green emission under NIR excitation, we propose RE ion doped $KGdF_4$ UCNP as a prospective host lattice for usage as fluorescent probes in bio-photonic applications along with other various lighting and display applications.

Chapter 4: A study on up-conversion and energy transfer kinetics of $KGdF_4:Yb^{3+}/Er^{3+}$ nanophosphors

$KGdF_4$ up-conversion nanoparticles doped with ytterbium (Yb^{3+}) and co-doped with erbium (Er^{3+}) ions were prepared via wet chemical route. Morphological confirmation was achieved through high resolution transmission electron microscopy (HR-TEM) and EDAX studies. The size of the nanoparticles lie in the range of 5-7nm. The samples emit intense up-converted green light centered at 545nm ($^4S_{3/2}\rightarrow{}^4I_{15/2}$) under 980nm CW laser excitation. A red emission centered at around 650nm ($^4F_{9/2}\rightarrow{}^4I_{15/2}$) is also seen. Detailed study on up-conversion process showed involvement of energy transfer (ET) and ground/excited State absorption (ESA/GSA) processes between dopant ions. Decay kinetics of these UCNPs at 545nm emission under 980nm CW laser excitation were studied. These UCNPs exhibit lifetimes in the range of 0.909ms to 1.162ms. Inokuti- Hirayama (I-H) model was applied to establish the mechanism of energy transfer between the dopant ions. I-H model analysis proved that the interaction between Yb^{3+} and Er^{3+} ions is dipole-dipole in nature. Electron paramagnetic resonance (EPR) study was conducted to study the effect of having Gd^{3+} in the host lattice. The observed "g" values in the EPR spectra correspond to the characteristic "U" spectrum of gadolinium. Given their small sizes, ability to exhibit up-conversion and high lifetimes, we propose to utilize these UCNPs for bio-photonic applications. The results of this study have been published in **Journal of Molecular Structure 1205 (2020) 127647**

4.1 Introduction

As has been discussed in chapter 1, the idea of up-conversion (UC) was conceived by a Dutch physicist N. Bloembergen in 1959 when he proposed a device known as “infrared quantum counter” [1]. In this device, two or more low energy (NIR region) photons were absorbed by ions having a multi-energy level arrangement. This lead to the excitation of the ions from ground state to intermediate excited states and subsequently to higher excited states. Finally, such an excited ion could de-excite to the ground state by emitting a photon of higher energy (visible region). This whole process was termed as up-conversion consisting of a multi-photon absorption and anti-stokes emission process that was different from the kind of luminescence that was observed in conventional organic dyes and quantum dots [2]. Since the intermediate energy levels in up-conversion processes are real as compared to the simultaneous multi-photon absorption processes where the intermediate levels are virtual, the UC processes exhibit higher luminescence efficiencies [1,7].

Organic dyes and quantum dots are the traditional imaging tools used in the field of bio-imaging. However, as has been explained earlier, these particles are marred with many serious disadvantages like photo bleaching, chemical degradation, broad emission spectra and narrow absorption, high cytotoxicity and chemical instability [13] . Moreover the usage of high energy radiation for imaging purposes has some serious drawbacks. It results in a low light penetration depth of the excitation radiation, a weak signal to noise ratio (SNR), autoflourescence and above all, damage or possible death of the healthy tissue due to the use of high energy radiations like UV or X-rays [13,44,121,122].

RE ions doped UCNPs have since then taken the spotlight in the field of bio-imaging research and applications due to their ability to absorb NIR light and emit in visible regions via nonlinear optical process known as up-conversion. These particles exhibit the following

advantages that make them an ideal replacement for the conventional dyes used in the field of bio-imaging other bio-photonic applications: 1) high signal to noise ratio (SNR) 2) absence of autofluorescence 3) zero photo bleaching 4) zero toxicity 5) high chemical stability 6) no damage to healthy tissue due to the usage of low energy excitation source (NIR) 7) deeper penetration of NIR radiation as compared to high energy radiations like UV/X rays 8) cost effective [13,123–126]

In this chapter, cubic phase Potassium Gadolinium Fluoride ($KGdF_4$) UCNPs prepared via a wet chemical route have been reported. These UCNPs have been doped with Ytterbium (Yb^{3+}) and co-doped with Erbium (Er^{3+}) ions. Yb^{3+} ion has an extremely simple energy level scheme which is complemented by ladder like energy level scheme of activator Er^{3+} ion [13]. So these ions are well suited for energy transfer cum luminescence studies and were chosen as RE dopants in this work. Since Yb^{3+} ion acts as sensitizer absorbing incident NIR radiation and transferring the energy to Er^{3+} activator ions via up-conversion processes like energy transfer, excited state absorption/ground state absorption, more the number of Yb^{3+} ions, more will be the energy transfer to Er^{3+} ions leading to increase in intensity of 545nm emission. This is due to increase in the rate of electron transfer between the dopant ions. Therefore, rate of energy transfer depends on the concentrations of Yb^{3+} ions. Accordingly, a series of samples keeping the concentration of Er^{3+} fixed at 5mol% and varying the concentration of Yb^{3+} from 5mol% to 20mol% was prepared. As reported earlier, this is the first time that sub-10nm $KGdF_4$ UCNPs have been reported which were synthesised via a wet chemical route [93]. The presence of gadolinium in the host matrix of any up-conversion nanoparticle multiplies the scope of bio-imaging applications. Although gadolinium has no effect on luminescence properties of the material, the presence of paramagnetic Gd^{3+} renders these UCNPs favourable for usage in MRI applications as T1/T2 contrasting agents which make this UCNP lattice different from other conventional alkali fluoride lattices like $NaYF_4$. [127–131]. Also, as has

been discussed in chapter 1 that, Gd^{3+} ion in the host lattice plays a role of network former and allows to dissolve the dopant RE ions to the extremely high concentrations > 25wt%. From literature it is already known that the UC efficiency increases when the particle size is below 10nm as compared to the well reported conventional UC lattice $NaYF_4$ that has larger sizes [109]. The as prepared $KGdF_4$ UCNPs have advantages like small size (less than 10nm) along with the presence of an alkali metal ion that enhances the luminescence in the host lattice. This along with the possibility of exploiting the magnetic properties of gadolinium in MRI applications opens up lot of scope of research and development of these particles [18,132–134]. Therefore, the UCNPs reported here may act as ideal probes for bio-imaging and other bio-photonic applications.

4.2 Experimental

For the purpose of synthesizing the UCNPs, gadolinium acetylacetonate [Alfa Aesar, 99.99%,1 mol%] and potassium flouride [Fisher Scientific, 4mol%] were used. Ytterbium chloride hexahydrate [5, 10, 15 and 20mol%] [Sigma Aldrich, 99.99%] and erbium chloride hexahydrate [5mol%] [Sigma Aldrich, 99.99%] were used as RE dopants.10ml of methanol [Sisco research laboratories] was used as a solvent for each precursor. The Gd^{3+} solution and Yb^{3+} / Er^{3+} solutions were added to KF solution drop wise and then aged at 65^0C for three and a half hours under magnetic stirring [92,93]. After centrifuging at 13,000rpm, the sample was then dried in a vaccum oven at 55ºC for 15 hours.

HR-TEM was performed on a Tecnai G^2 20 transmission electron microscope operating at an accelerating voltage of 120kV in magnification range of 20000x to 50000x. SEM and EDAX studies were conducted using Oxford INCA 250 VEGA3 TESCAN scanning electron microscope at 5kx magnification under 15kV of accelerating voltage. UC studies and photoluminescence under UV excitation were carried out using Horiba model QM-8450-11

spectrometer. For PL decay measurements, TDS 3012C digital oscilloscope was used in unison with a 980nm CW laser. EPR was performed using a Bruker model EMX MicroX setup at microwave frequency of 9.665 GHz with power being set as 6.371 mW.

4.3 Results and Discussion

4.3.1 Morphological Analysis

4.3.1.1 HR–TEM analysis

Before moving ahead with the HR-TEM analysis, XRD for the as prepared samples was recorded as well. It was found out that the $KGdF_4:Yb^{3+}/Er^{3+}$ UCNPs have exactly the same phase as $KGdF_4:Yb^{3+}/Tb^{3+}$ phosphors which has been reported in the chapter 3 [93]. There was no change in peak positions or any change in phase with the addition of Er^{3+} ions in the host lattice. Also, not much change was observed between the values of crystallite sizes and lattice parameters of the as prepared samples and the $KGdF_4:Yb^{3+}/Tb^{3+}$ UCNPs that were reported earlier [93,112,113,135].

Fig. 4.1 shows HR-TEM image of $KGdF_4:Yb^{3+}$ (20%) / Er^{3+} (5%) sample. The nanoparticles are seen to be agglomerated. Inset shows the HR-TEM image at 20nm scale resolution. The particle size range estimated using ImageJ software tool was between 5-7nm which is confirmed by the Debye-Scherrer analysis as well since at nano scale, the crystallite size and particle size are equivalent.

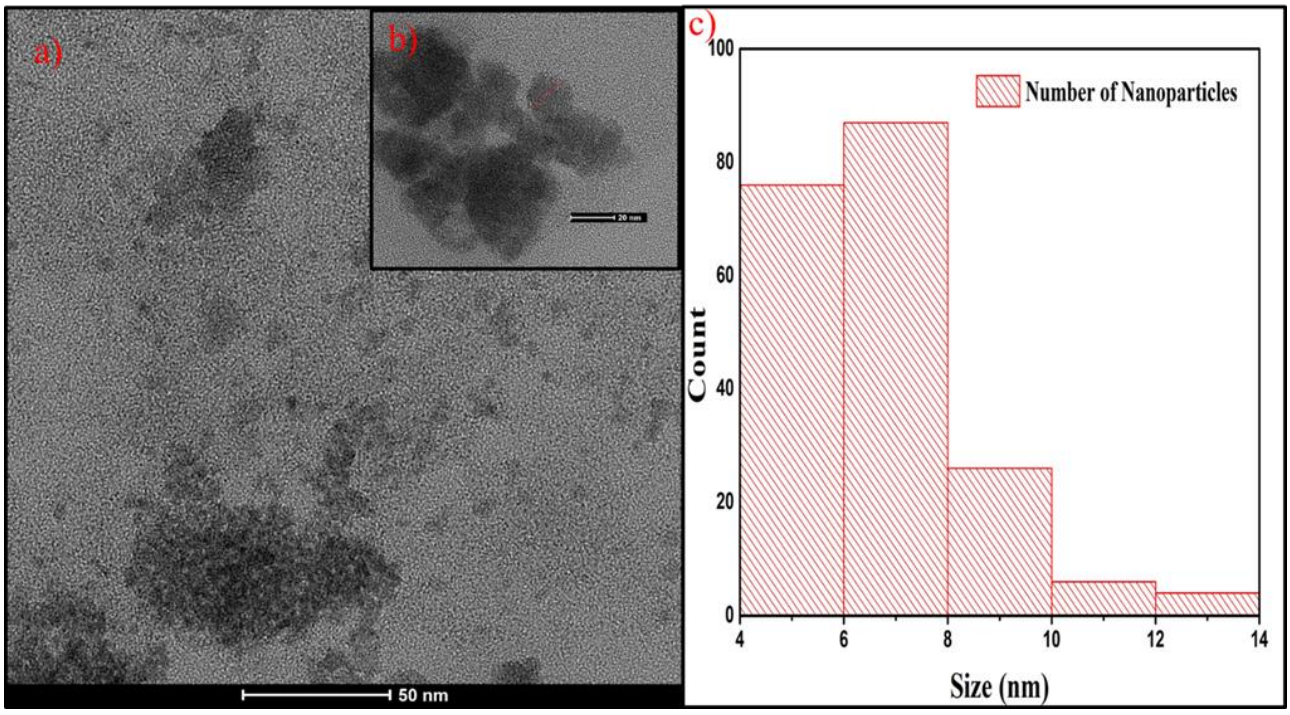

Fig. 4.1: (a) HR-TEM image of $KGdF_4$*:*Yb^{3+} *(20%)/* Er^{3+} *(5%)* sample (b) Inset shows the HR-TEM image of the sample at 20nm scale (c) Particle size distribution of the nanoparticles.

4.3.1.2 EDAX and SEM Studies

EDAX study was conducted on the UCNPs and is shown in Fig. 4.2. The SEM image and atomic and weight percent of atoms have also been added for reference. It can be clearly seen from that all the major constituents of the UCNPs i.e., K^+, Gd^{3+}, F^+, Yb^{3+}, Er^{3+} are present in the host lattice[136].

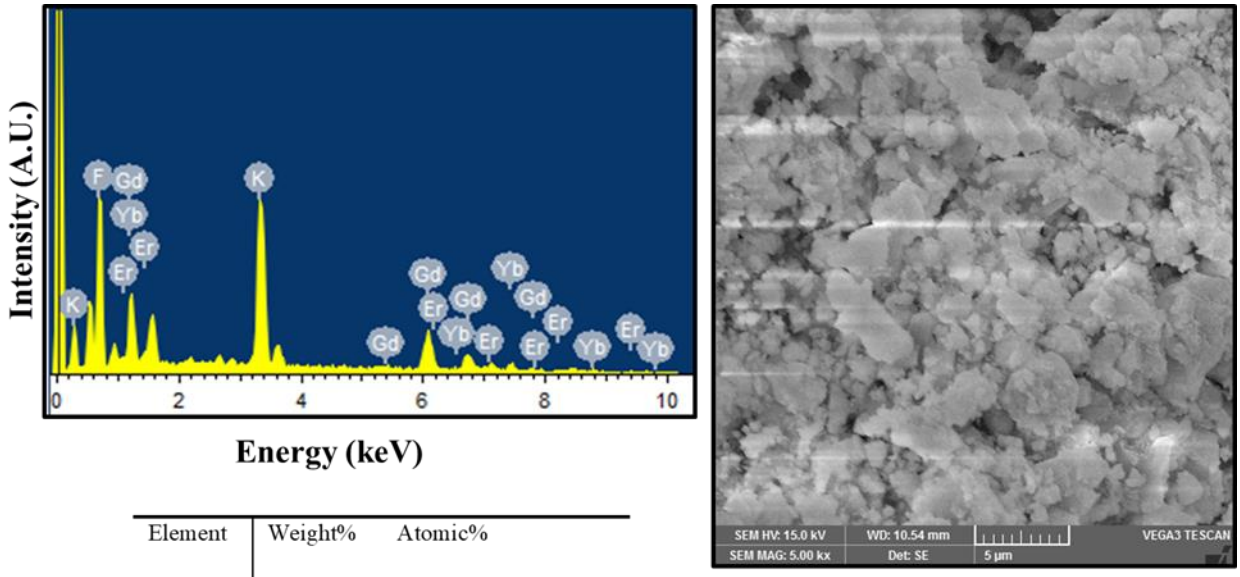

Element	Weight%	Atomic%
F K	28.56	65.46
K K	18.18	20.25
Gd L	33.31	9.22
Er M	4.83	1.26
Yb M	15.12	3.81
Totals	100.00	

Fig. 4.2: EDAX spectra showing constituent elements in the co doped $KGdF_4$ lattice

4.3.2 Photoluminescence Studies

4.3.2.1 Optimization of Er^{3+} ion concentration

A series of $KGdF_4$: Er^{3+} (x= 1, 2, 3, 4,5,6 and 7mol%) samples was prepared to check the optimum concentration of Er^{3+} needed for studying the UC mechanisms in co-doped samples of the host lattice. As seen in Fig. 4.3, under 450nm excitation, a sharp peak at nearly 545nm was seen. It was observed that peak intensity increased with the increment of Er^{3+} ions till 5mol% concentration after which concentration quenching occurred. Therefore Er^{3+} concentration at 5mol% was chosen as the required fixed concentration of the activator ion for luminescence studies.

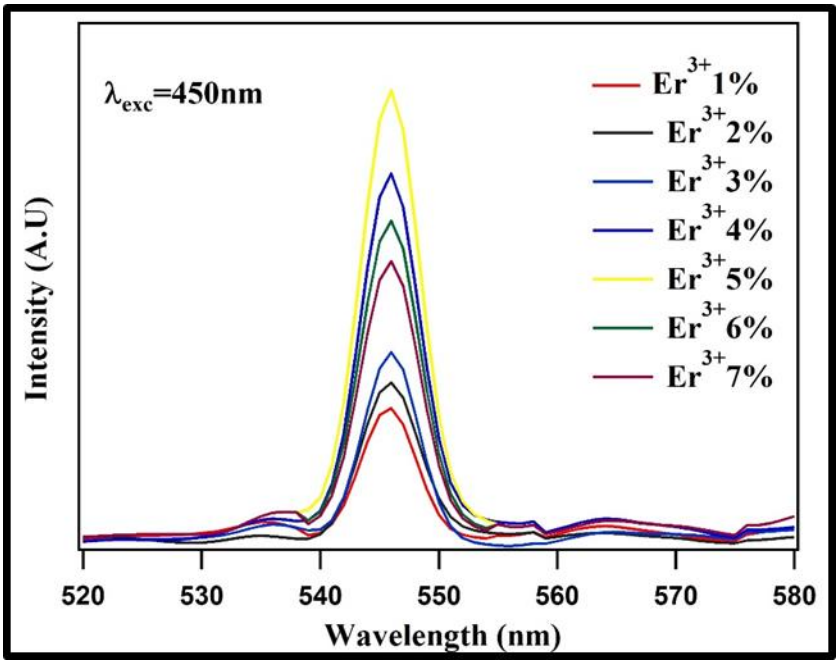

Fig. 4.3: Optimization of Er^{3+}: emission spectra recorded under 450nm excitation

4.3.2.2 Up–conversion spectral studies

The up-conversion luminescence spectra of $KGdF_4:Yb^{3+}$ (x=5, 10, 15, 20 mol%) / Er^{3+} (5%) under 980nm (NIR) CW laser excitation (1W power) are given in Fig. 4.4. Two intense bands corresponding to green (around 545nm) and red (around 650nm) regions are observed corresponding to the $^4S_{3/2} \rightarrow {}^4I_{15/2}$ and $^4F_{9/2} \rightarrow {}^4I_{15/2}$ transitions respectively. A less intense band at 470nm (blue region) corresponding to $^4F_{7/2} \rightarrow {}^4I_{15/2}$ transitions is also observed [137–140]. An increase in the intensity of the peaks in the green and red regions was observed with increasing concentrations of Yb^{3+} ions i.e., energy transfer from sensitizer Yb^{3+} ion to activator ion Er^{3+} was successful in the UC process resulting in the increment of excited Er^{3+} ions emitting in the visible region after relaxation to the ground states [118,141] This could be due to decrease in the inter-ionic distance between Yb^{3+} and Er^{3+} ions. This simply enhances the transfer of energy from sensitizer Yb^{3+} to activator Er^{3+} ions.

It was also seen that the peaks at 545nm and 650nm exhibited splitting. This is again due to the crystal field splitting effects in the host lattice due to high crystallinity and successful substitution of the RE ions in the Gd^{3+} lattice [93].

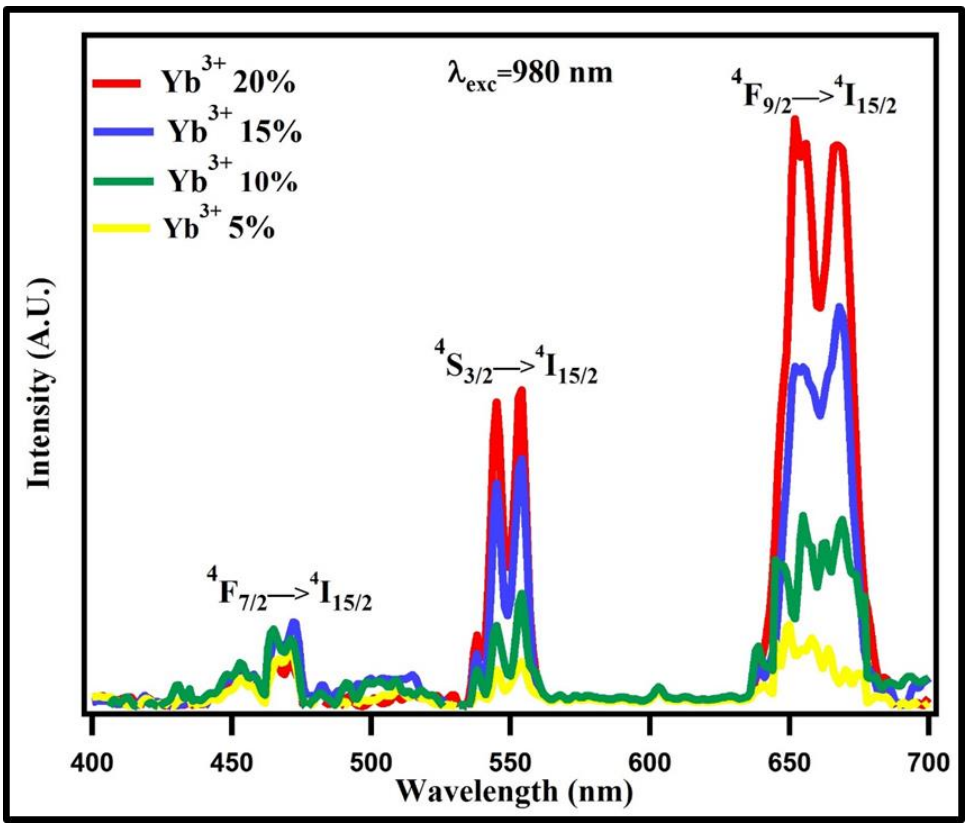

Fig. 4.4: UC spectra of the as prepared samples under 980nm CW laser excitation *(*1W power*)*

4.3.2.3 Power dependent UC studies and energy transfer mechanism

For studying the mechanism of energy transfer between sensitizer Yb^{3+} and activator Er^{3+} ions in the host lattice under 980nm excitation, $KGdF_4:Yb^{3+}$ (20%) / Er^{3+} (5%) sample was excited by variable power 980nm CW laser. According to literature, for an unsaturated up-conversion process, the photons needed to populate the excited upper state are given by the power law as enumerated by equation 3.1 in Chapter 3 [142].

The variations of intensity with varying power of 980nm CW laser for blue, green and red peaks were observed and the recorded spectra are shown in Fig. 4.5(a). A double logarithmic

plot between intensity and power was plotted for the sample under consideration and is shown in Fig. 4.5(b). For all the three emissions, the plots are linear with slopes being equal to 1.34, 1.61 and 1.85 for the blue, green and red emission peaks respectively. The slopes here are equal to the value of n as given in equation 3.1. Now for the observed blue, green and red emissions which are two photon processes, the value of n should be nearly equal to 2. In the present study, the values of n for all the three emissions came out to be less as compared to the expected values [143,144]. As theorized by Pollnau et al , this deficit in the values of n is due to the fact that UC and linear decay processes compete with each other to deplete the intermediate excited states [145].

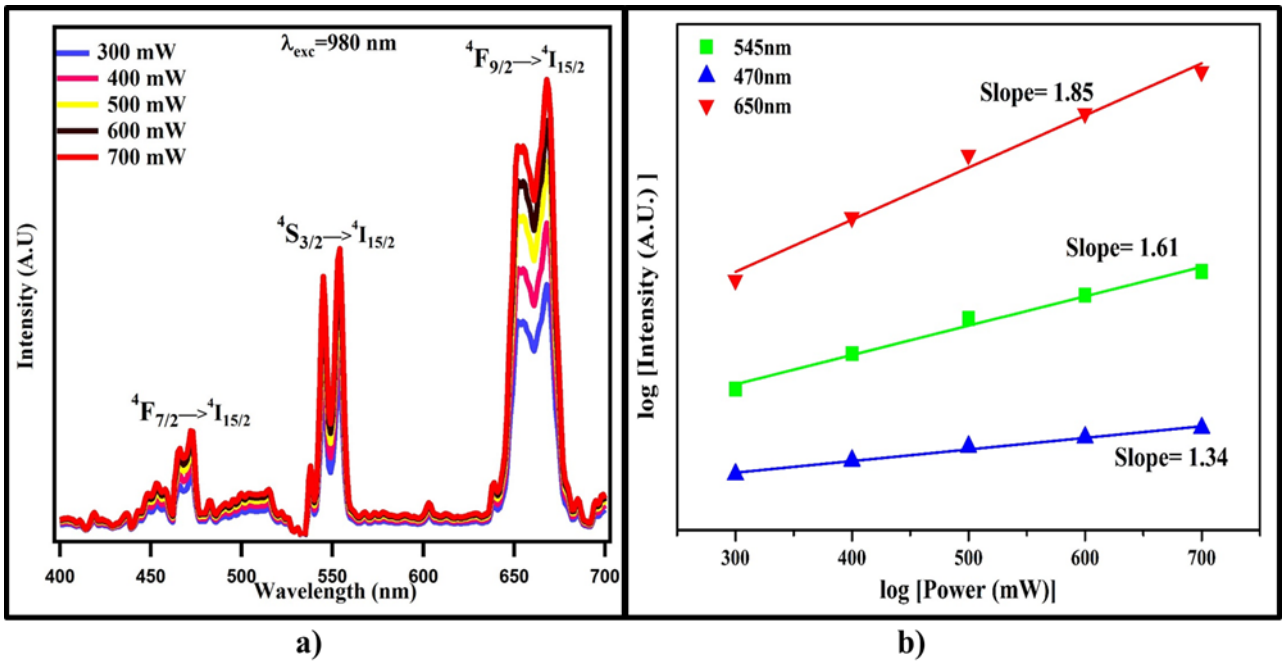

Fig. 4.5:(a)UC spectra of $KGdF_4$:Yb^{3+} *(20%)* / Er^{3+} *(5%)* sample under varying powers of 980nm CW laser (b) log I vs log P plots for blue, green and red emissions observed in the UC process.

The possible UC mechanism in $KGdF_4:Yb^{3+}/ Er^{3+}$ UCNPs is given in Fig.4.6. Yb^{3+} ion has two energy levels, one ground state at $^2F_{7/2}$ and another excited state at $^2F_{5/2}$. The excited state of Yb^{3+} i.e., $^2F_{5/2}$ has energy comparable to $^4I_{11/2}$ which is the excited state of Er^{3+} ion. The Yb^{3+} ion acts as a sensitizer and under 980nm excitation, transfer of energy takes place from Yb^{3+} to an Er^{3+} ion in ground state which in turn gets excited to the $^4I_{11/2}$ state. Now, another energy transfer between the Yb^{3+} ion ($^2F_{5/2}$) and an excited Er^{3+} ion ($^4I_{11/2}$) further excites the Er^{3+} ion to the upper $^4F_{7/2}$ excited state. The Er^{3+} ion relaxes both radiatively and non-radiatively from this state. The radiative relaxations give rise to the blue emission centered at around 470nm. Non-radiative relaxation to low lying $^4S_{3/2}$ state produces the green emission centered at around 545nm. The emission in red region at 650nm from the $^4F_{9/2}$ level takes place because of a non-radiative relaxation from the higher $^2H_{11/2}$ and $^4S_{3/2}$ states or by a relaxation from $^4I_{11/2}$ to $^4I_{13/2}$ followed by excitation of Er^{3+} ion from $^4I_{13/2}$ to $^4F_{9/2}$ via energy transfer from Yb^{3+} ($^2F_{5/2}$) ion [137,144]. All the energy transfer processes are given as follows:

$$^2F_{5/2}\,(Yb^{3+}) + {}^4I_{15/2}\,(Er^{3+}) \rightarrow {}^2F_{7/2}\,(Yb^{3+}) + {}^4I_{11/2}\,(Er^{3+})$$

$$^2F_{5/2}\,(Yb^{3+}) + {}^4I_{11/2}\,(Er^{3+}) \rightarrow {}^2F_{7/2}\,(Yb^{3+}) + {}^4F_{7/2}\,(Er^{3+})$$

$$^2F_{5/2}\,(Yb^{3+}) + {}^4I_{13/2}\,(Er^{3+}) \rightarrow {}^2F_{7/2}\,(Yb^{3+}) + {}^4F_{9/2}\,(Er^{3+})$$

The non-radiative relaxations involved in the UC process are given as follows:

$$^4F_{7/2}\,(Er^{3+}) \rightarrow {}^2H_{11/2}\,(Er^{3+})$$

$$^2H_{11/2}\,(Er^{3+}) \rightarrow {}^4S_{3/2}\,(Er^{3+})$$

$$^4S_{3/2}\,(Er^{3+}) \rightarrow {}^4F_{9/2}\,(Er^{3+})$$

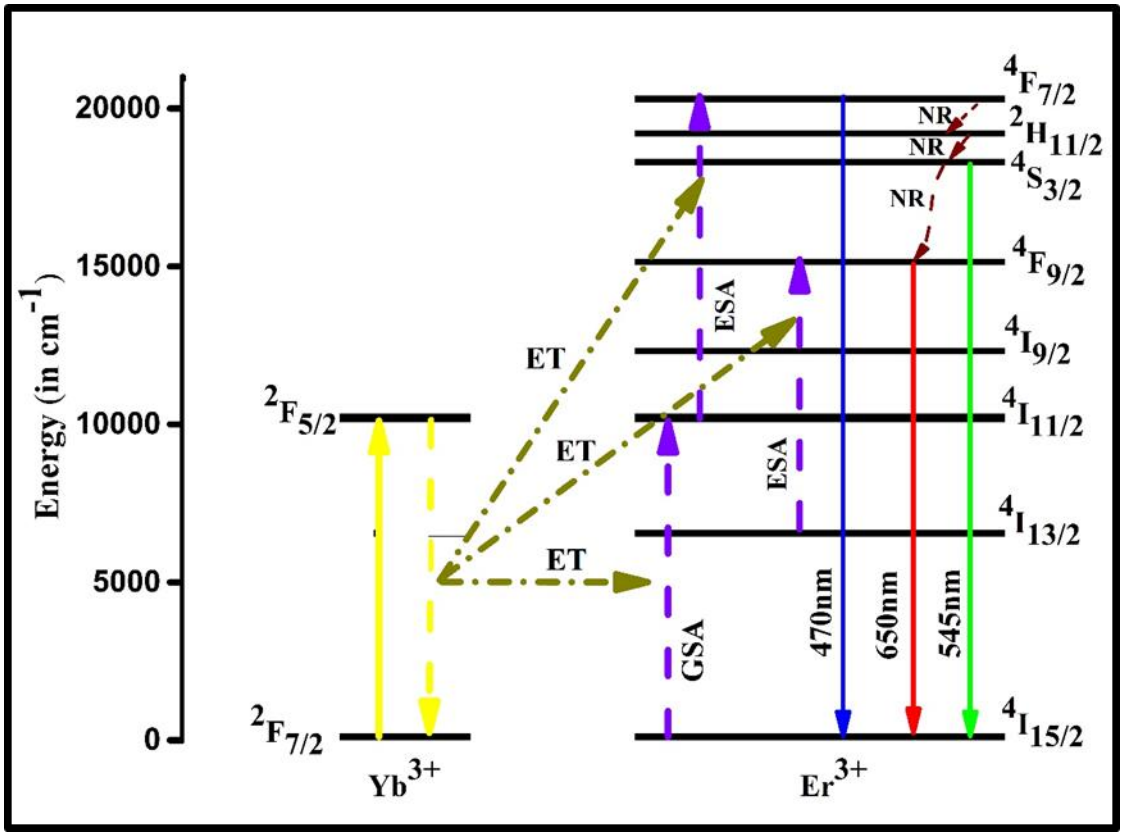

Fig. 4.6: A schematic diagram showing the possible energy transfer mechanism between Yb^{3+} and Er^{3+} ions in the UC process

4.3.2.4 Decay kinetics and Inokuti–Hirayama model analysis

Decay curves observed for the UC process i.e., 545nm emission under NIR excitation were plotted and are shown in Fig.4.7 (a). It was seen that the curves fitted well to a bi-exponential function as given by equation 3.2 in Chapter 3 [146]. This is due to predominant energy transfer and ion-ion interactions in the host lattice rendering the emission with both slow and fast components [118]. The decay times as calculated for the $KGdF_4:Yb^{3+}$ (x=5%, 10%, 15% and 20 %) / Er^{3+} (5%) are 1.162ms. 1.066ms, 1.045ms and 0.909ms respectively. There is a clear decrease in the decay times of the samples with the increment in Yb^{3+} concentration. This is due to the quenching of the $^4S_{3/2}$ level by increased Er^{3+}-Yb^{3+} interactions leading to backward transfer of energy from Er^{3+} ions to Yb^{3+} ions. This happens due to the presence of more Yb^{3+} ions in the neighborhood of Er^{3+} [93].

The nature of the energy transfer mechanism between dopant RE ions was studied by applying the Inokuti-Hirayama (I-H) model. According to this theory, the emission intensity is given as:

$$I(t) = Ioexp\left[-\frac{t}{\tau o} - Q(\frac{t}{\tau o})^{3/S}\right] \quad (3)$$

where t is attributed to the time after excitation and τo is the intrinsic decay time of the donors in the absence of acceptors. The value of S can either be 6, 8 or 10 depending upon whether the interactions are dipole-dipole or dipole-quadrupole or quadrupole-quadrupole in nature respectively[89,147]. Q is the energy transfer parameter given by the following relation:

$$Q = \frac{4\pi}{3}\Gamma\left(1 - \frac{3}{S}\right)NoRo^3 \quad (4)$$

Here Γ(x), for dipole-dipole interactions, is 1.77, for dipole-quadrupole interactions it is 1.43 and for quadrupole-quadrupole interactions, it is 1.3. N_0 is the concentration of rare earth ions and R_o is defined as the critical energy transfer distance between the donor and acceptor ions. The decay curves along with I-H fitting are shown in Fig. 4.7. (b). The curves fitted well for S=6 thereby confirming the dipole-dipole nature of energy transfer mechanism between Yb^{3+} and Er^{3+} ions.

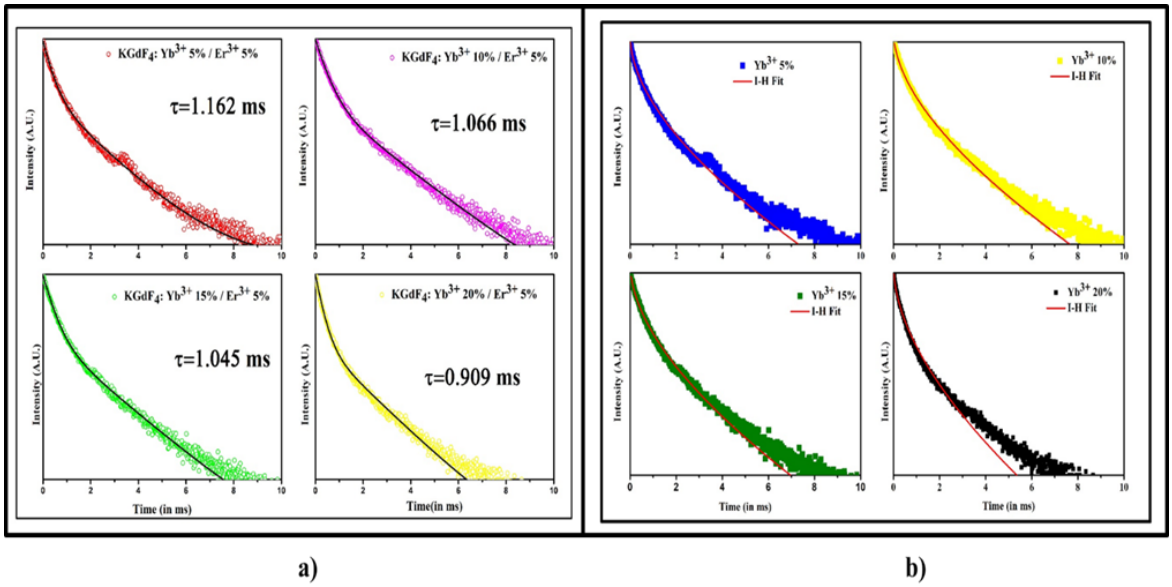

Fig. 4.7: (a) Decay curves of the as prepared samples observed at 545nm emission under 980nm CW laser excitation (b) Decay curves of 545nm emission with I-H Fitting under 980nm CW laser excitation

The values of Q and R_o were calculated and are presented in Table 4.1. It was observed that the value of Q increases with increasing concentration of Yb^{3+} ions. The values of R_0 on the other hand decrease with increasing concentrations of Yb^{3+} ions. A decrease in the distance between sensitizer and activator ions results in the increase in the transfer of energy between them i.e., increase in the value of Q which ultimately results in a faster decay [148–150].

Table 0.1**:** Calculated values of Energy Transfer Parameter Q and Critical Energy Transfer Distance R_o (in Å):

Concentration of Yb^{3+}	Q	R (Å)
5%	3.98	4.71
10%	4.28	4.21
15%	4.30	3.84
20%	4.48	3.61

An image showing the Commission Internationale de L'Eclairage (CIE) chromaticity diagram for the UC process is given in Fig. 4.8. CIE diagram indicates clearly that the calculated coordinates are lying in the green region [151]. The CIE coordinates and the decay lifetimes of the UCNPs for the UC process are given in Table 4.2.

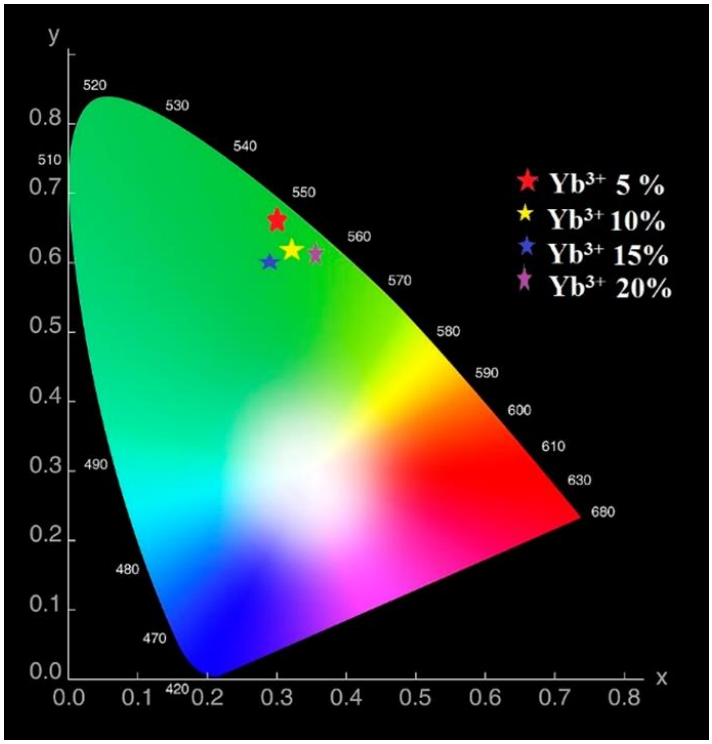

Fig. 4.8: CIE chromaticity diagram for the NIR UC process for the $KGdF_4:Yb^{3+}$ (5, 10, 15, 20%) / Er^{3+} (5%) samples

Table 0.2: Lifetimes and CIE Coordinates of the as prepared $KGdF_4$ samples for UC studies under 980nm CW laser excitation:

Concentration of Yb^{3+}	CIE Chromaticity Coordinates		Lifetime(ms)
	X	Y	
5%	0.315	0.654	1.162
10%	0.362	0.602	1.066
15%	0.334	0.598	1.045
20%	0.408	0.661	0.909

4.3.2.5 Down conversion studies

Fig. 4.9. (a) Shows the excitation spectra of $KGdF_4:Yb^{3+}(20\%) / Er^{3+}$ (5%) sample at emission wavelength 545nm. Four bands corresponding to the multiplets of $^4F_{5/2}$, $^4F_{3/2}$, $^4G_{11/2}$ and $^4G_{9/2}+^2G_{7/2}+^2K_{15/2}$ are seen [152]. The emission spectra of the as prepared samples under 322nm excitation are shown in Fig. 4.9. (b). Three peaks corresponding to $^4F_{7/2}\rightarrow{}^4I_{15/2}$ (470nm), $^2H_{11/2}\rightarrow{}^4I_{15/2}$ (523nm) and $^4S_{3/2}\rightarrow{}^4I_{15/2}$ (545nm) are observed. The intensity of the green emission of the sample having lowest Yb^{3+} doping i.e., 5mol% is the highest. The intensity is seen decreasing subsequently with increasing concentration of Yb^{3+} [153]. This can be possibly due to concentration quenching effect. With increasing number of Yb^{3+} ions around the Er^{3+} ions, some energy gets transferred backwards from Er^{3+} to Yb^{3+} ions thereby reducing the emission intensity of Er^{3+} ions.

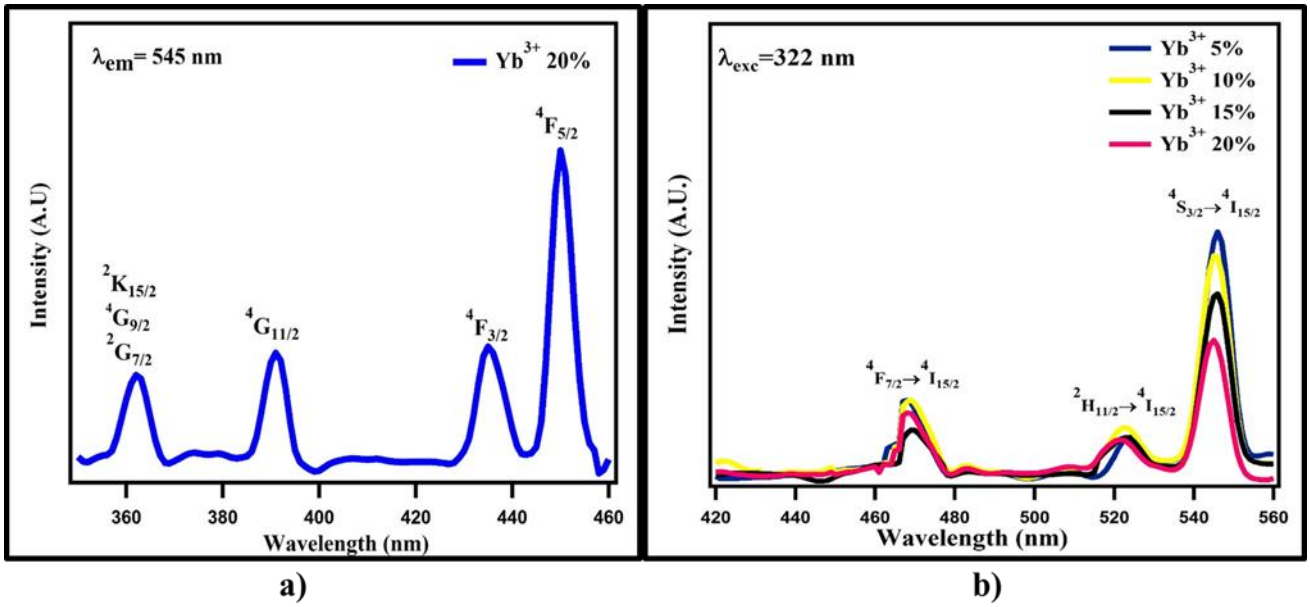

Fig. 4.9: (a) Excitation spectra of $KGdF_4:Yb^{3+}$ (20%) / Er^{3+} (5%) sample observed at 545nm emission wavelength. (b) Emission spectra of $KGdF_4:Yb^{3+}$ (5, 10, 15 and 20%) / Er^{3+} (5%) samples under 322nm UV excitation.

4.3.3 EPR Studies

Gadolinium ion has a fully polarized half-filled 4f shell. Due to the occupation of these 4f states according to Hund's rule, the magnetic moment involves a high spin derived contribution along with a zero angular momentum. Also, the effective spin S in this case is 7/2. The observed spectrum is a characteristic of S state RE ion involving a low symmetry site. Many studies have now established that the spectral properties depend on the relative magnitude of ligand field strength and Zeeman microwave frequency. If the ligand field strength is smaller than the Zeeman Frequency, then signals occur at g≈2.0. On the other hand if ligand field strength is larger than the Zeeman frequency then signals are observed in the range g>2.0. If both the Zeeman term and ligand field strength are comparable then there is zero field resonance. It has been observed that Gd^{3+} ion is either 6 or 8 coordinated and prefers a vitreous phase for accommodation over a crystalline state of higher symmetry [154].

The EPR spectra of $KGdF_4$: Yb^{3+} (20%) / Er^{3+} (5%) is shown in Fig. 4.10. The exhibited effective g values are observed at 2.29, 2.19, 2.16, 2.13, 1.93, 1.89, 1.84 and 1.81. The signals indicate a low site symmetry where the Gd^{3+} ions have substituted the K^+ ions in the lattice. Also, these signals can be attributed to fine structure transitions involving unequal spacing and intensities. The ionic radii of K^+ and Gd^{3+} ions are 0.138nm and 0.108nm respectively. So it can be assumed that Gd^{3+} ions occupy the K^+ sites leading a formation of cation vacancy either in the vicinity or far away. This helps in maintaining charge neutrality. These g values can be attributed to the g values of the "U" spectrum which are characteristic of gadolinium ions in amorphous materials signifying a weak field of cubic symmetry between gadolinium ions and host lattice. Gadolinium ions in these sites are subjected to a weak crystal field. Also, these sites are characterized by a coordination number more than six. Values of g between 2 and 6 have been reported by many authors in the available literature of glasses and phosphors. These values are consistent with the same [154–156].

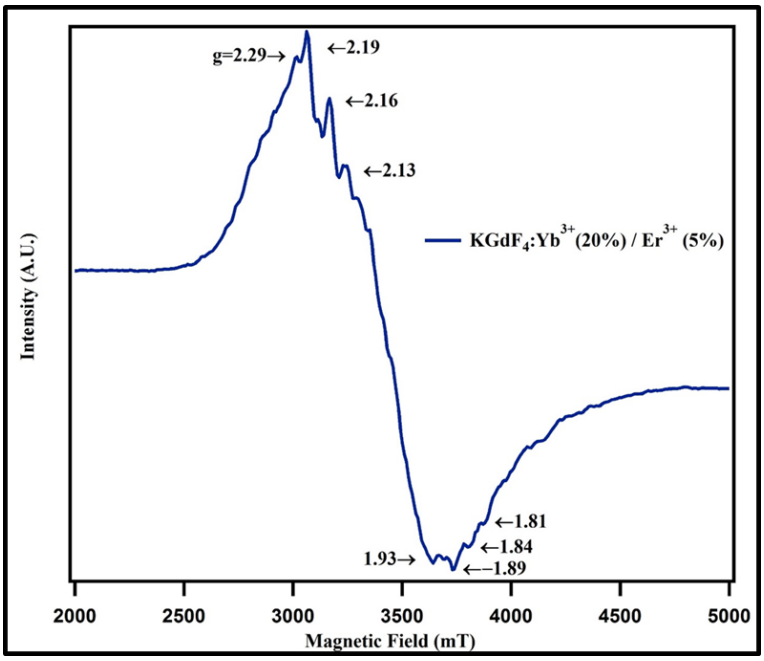

Fig. 4.10: EPR spectra of $KGdF_4$:Yb^{3+} *(20%)* / Er^{3+} *(5%)* sample. Corresponding g values are also marked for reference

It has been reported that the EPR spectra of disordered materials doped with RE ions is highly anisotropic and depends on site to site ligand-field variations. The g values of 6.0, 2.87 and 2.0 have been considered as the results of gadolinium ions dispersed in cubic, octahedral or tetrahedral sites with moderate distortion. The locations of Gd^{3+} ions are unusual due to the fact that they tend to occupy locations having higher coordination numbers. Tamboli et al. have reported effective g values of 6.11, 3.94, 2.65 and 1.99 but have not defined the site symmetry of the Gd^{3+}ions [157]. Mohapatra et al. have reported effective g values of 6.0, 2.8, and 2.0. They have analysed them to be due to octahedral or cubic sites of a weak crystal field [158]. Rada et al. have reported effective g values of 6.0, 2.87 and 2 and designated them as strong, intermediate and weak cubic fields of symmetry respectively [159].

4.4 Conclusions

Sub-10nm cubic phase $KGdF_4:Yb^{3+}/Er^{3+}$ UCNPs were prepared via a wet chemical route. Morphological studies like HR-TEM and EDAX were performed on UCNPs. PL studies like up-conversion, decay kinetics and down conversion were performed. Under 980nm CW laser excitation, the samples exhibit up-conversion emitting intense green light centred at around 545nm arising from the $^4S_{3/2} \rightarrow {}^4I_{15/2}$ transition. Decay lifetimes of the samples vary from 1.162 to 0.909ms for Yb^{3+} 5mol% to 20mol% concentration respectively. Application of I-H model in studying the energy transfer dynamics revealed that the interaction between the sensitizer and activator ions is dipole-dipole in nature. Under UV excitation, the samples exhibited the phenomenon of down conversion as well having bands in the blue and green regions of the spectrum. EPR study detailed out the effect of having a paramagnetic ion like Gd^{3+} on the lattice symmetry. The observed g values belong to the “U” spectrum and can be associated with a weak cubic symmetry field between Gd^{3+} and the host lattice. Since the as prepared samples exhibit intense up-conversion/down conversion under NIR/UV excitation along with

having high lifetimes, it is proposed that these samples be utilized for bio-photonic applications and in w-LEDs/ solid state lighting (SSL) applications as well.

Chapter 5: Up-conversion luminescence and EPR properties of $KGdF_4:Yb^{3+}/Tm^{3+}$ Nanophosphors

Synthesis of $KGdF_4:Yb^{3+}/Tm^{3+}$ up-conversion nanoparticles (UCNPs) via wet chemical route has been reported. HR-TEM, EDAX and EPR studies were performed on the samples. The samples emit intense blue light centered at 472nm ($^1G_4 \rightarrow {}^3H_6$) under 980nm CW laser excitation. Energy transfer (ET), ground/excited state absorption (ESA/GSA) and cooperative energy transfer (CET) were established as the possible energy transfer mechanisms in the up-conversion (UC) process. Since these UCNPs, synthesized by a much cost effective route, have sizes comparable at cellular level and exhibit the ability of up-conversion, it is proposed to utilize these UCNPs for prospective bio-photonic applications. The results of this study have been published in **Optik, 208 (2020) 164538**

5.1 Introduction:

A non-linear process in which a sequential absorption of two or more photons of low energy (in NIR region) results in the emission of photons of high energy (lying in visible or UV region) is termed as up-conversion [160]. Lanthanide based materials have attracted significant attention in the field of up-conversion research due to their unique ladder-like abundant energy levels that lead to the intra-4f or 5d transitions. Apart from this, lanthanide based materials possess excellent properties like large anti-Stokes shifts, excellent photostabilities, sharp emission bands and high lifetimes [161–163]. This phenomenon of up-conversion has been applied successfully to develop new host materials to be used as imaging probes in bio-imaging applications despite the fact that a lot many organic dyes, fluorescent proteins and quantum dots have been developed for the same purpose [164–166].

Bio-imaging uses difference in light transmission, reflection and photoluminescence to provide a better contrast between the region to be imaged and the surrounding area and is the best used technique to visualise the details at cellular level [167,168]. Aforementioned conventional tools like dyes, proteins and quantum dots have been used for the purpose of imaging but then, these probes have some serious disadvantages like autofluorescence, low signal to noise ratio (SNR), photobleaching along with having low chemical stability and high toxicity [50,169,170]. Moreover, as has been discussed in the previous chapter 1, usage of high energy radiation (UV or other short wavelength radiation) for excitation of these probes results in poor penetration depth of the radiation and above all, damage or even death of the tissue that is being imaged and the surrounding tissues due to exposure to such high energy radiation [13,50].

This is where up-conversion comes into play. Lanthanide based up-conversion lattices have been developed to tackle the challenges posed by the conventional imaging probes. These up-conversion nanoparticles (UCNPs) rely on the transitions taking place between actual existing states thus differing from a nonlinear multiphoton absorption process involving virtual states.

Therefore their luminescence efficiency is also quite high. Also, since they use a CW NIR laser for excitation rather than a femtosecond or ultrashort pulsed one, they are cost effective in their usage too [7,163,171]. Above all, these UCNPs possess high signal to noise ratio (SNR), high physical and chemical stability, no photobleaching, zero autofluorescence and a high penetration depth due to usage of low energy NIR radiation for excitation purposes. Also, since the excitation source is of low energy, there is zero damage to the tissue being imaged [17,101,102,172].

In this chapter, synthesis and luminescent studies on potassium gadolinium fluoride ($KGdF_4$) UCNPs doped with ytterbium (Yb^{3+}) and co-doped with thulium (Tm^{3+}) ions have been reported. Sub-10nm UCNPs were prepared via a wet chemical route as described in Chapter 2. [92,93]. As has been stated earlier, $KGdF_4$ was chosen as a prospective host lattice due to its ability to act as a multifunctional compound i.e., to exhibit both up-conversion and paramagnetism. These properties can be employed in the present day bio-imaging and MRI applications successfully [93,173,174]. Also, since these UCNPs have sizes below 10nm, they are well usable at cellular level and have better luminescence efficiencies as compared to other phosphors having larger sizes [109,175].It is therefore proposed to utilize these UCNPs as prospective alternatives to the conventional imaging probes in the field of bio-imaging and other bio-photonic applications.

5.2 Experimental:

$Gd(acac)_3.xH_2O$ [Alfa Aesar,99.99%,1 mol%] and KF [Fisher Scientific, 4mol%] along with $YbCl_3$ [5, 10, 15 and 20mol%] [Sigma Aldrich, 99.99%] and $TmCl_3$ [2mol%] [Sigma Aldrich, 99.99%] were used as precursors to prepare $KGdF_4$ UCNPs. Each of the reactants were separately dissolved in 10ml of methanol [Sisco Research Laboratories]. The Gd^{3+} solution along with Yb^{3+} and Tm^{3+} solutions were added drop wise to KF solution and then aged at 65^0C

for three and half hours under magnetic stirring [92,93]. The resulting mixture was centrifuged at 13,000 rpm, washed with methanol thrice and then dried in a vacuum oven at 55^{o}C for 15 hours.

Tecnai G^2 20 transmission electron microscope was used for capturing TEM/HR-TEM images. Oxford INCA 250 VEGA3 TESCAN scanning electron microscope was used to record SEM and EDAX images. Horiba Model QM-8450-11 spectrometer was used for recording luminescence under NIR excitation. A TDS 3012C digital oscilloscope was used to record decay curves under 980nm CW laser excitation. Bruker Model EMX MicroX setup was used to study EPR properties.

5.3 Results and Discussion

5.3.1 Morphological Studies

5.3.1.1 HR-TEM and EDAX analysis

Fig. 5.1. (a) shows the HR-TEM image of $KGdF_4:Yb^{3+}$ (20%) / Tm^{3+} (2%) sample. It is evident that there is agglomeration in the sample. Using ImageJ software tool, the sizes of the UCNPs were calculated and found to be in the range of 6-8nm. Fig. 5.1. (b) shows HR-TEM image of the same sample. Lattice planes are clearly seen in the image implying high crystallinity of the lattice. The value of d-spacing was calculated and the same is shown on the graph. The value d= 0.27nm corresponds to the (200) plane of the $KGdF_4$ lattice as shown in Fig. 5.1(b).

The XRD spectra of the as prepared UCNPs was also recorded but as has been discussed in chapter 4, the as prepared UCNPs possessed a crystalline structure similar to cubic $NaGdF_4$ only. The values of lattice parameters and crystallite sizes that were calculated for the as prepared samples did not show any observable difference from the ones that were reported in chapter 3 [93]. Therefore, it can be safely asserted that with the addition of Tm^{3+} ion in the $KGdF_4$ host lattice, no change in the phase of the host material is observed [93,108,110,135].

Fig. 5.1(c) shows EDAX spectra of $KGdF_4$: Yb^{3+}(20%)/Tm^{3+}(2%) sample. It is clearly evident from the figure that all the constituent elements are present in the host material. The corresponding weight and atomic percentage is also given.

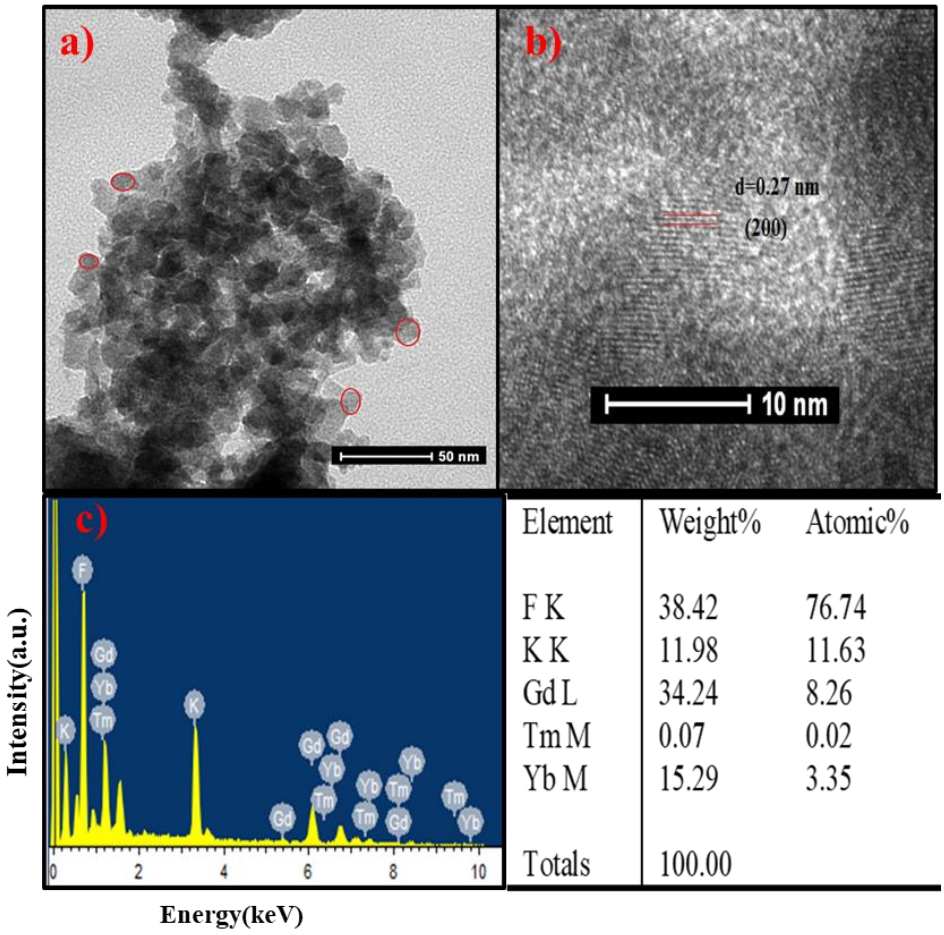

Element	Weight%	Atomic%
F K	38.42	76.74
K K	11.98	11.63
Gd L	34.24	8.26
Tm M	0.07	0.02
Yb M	15.29	3.35
Totals	100.00	

Fig. 5.1: (a) HR-TEM image of $KGdF_4$:Yb^{3+} (20%)/ Tm^{3+} (2%) sample (b) HR-TEM image with the calculated d-spacing and corresponding (hkl) plane (c) EDAX spectra of $KGdF_4$:Yb^{3+} (20%) / Tm^{3+} (2%) sample

5.3.2 Photoluminescence Studies

5.3.2.1 Optimisation of Tm^{3+} activator ion

Fig. 5.2 shows the emission spectra of singly doped $KGdF_4$:Tm^{3+} (x=1%, 2%, 3%, 4%, 5%) UCNPs under 280nm excitation. A sharp band at 472nm corresponding to $^1G_4 \rightarrow {}^3H_6$ transition is seen the intensity of which increases till 2% Tm^{3+} concentration and then decreases showing

concentration quenching. Therefore, for the purpose of further luminescence studies, 2mol% concentration of Tm^{3+} was chosen as the optimised concentration and samples with varying Yb^{3+} concentration were prepared to study the UC process and energy transfer mechanisms.

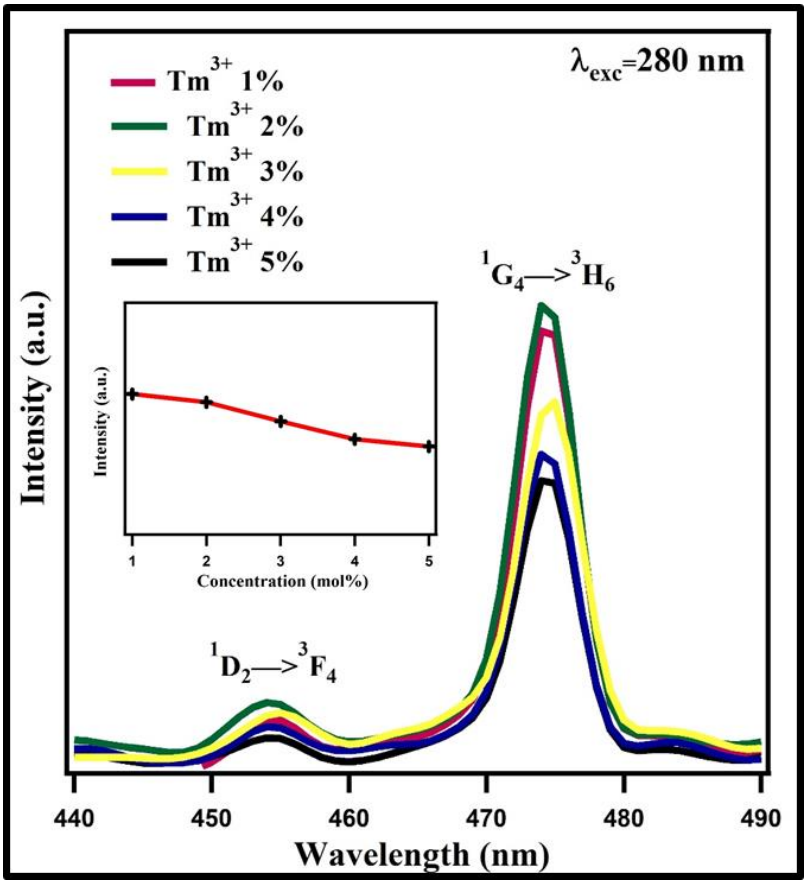

Fig. 5.2: Optimisation of Tm^{3+}: Emission spectra of singly doped $KGdF_4:Tm^{3+}$ (x=1%, 2%, 3%, 4%, 5%) UCNPs under 280nm excitation.

5.3.2.2 UC luminescence studies and energy transfer mechanism

Under 980nm CW laser excitation (power 1W), the as prepared samples exhibit the phenomenon of up-conversion. Intense blue emission centred at around 453nm and 472nm is seen corresponding to $^1D_2 \rightarrow {}^3F_4$ and $^1G_4 \rightarrow {}^3H_6$ transitions respectively. Emission in the red region has also been observed centred at around 650nm and 695nm/700nm corresponding to $^1G_4 \rightarrow {}^3F_4$ and $^3F_{2,3} \rightarrow {}^3H_6$ transitions respectively [110,176–179]. The UC spectra under 980nm

excitation is shown in Fig. 5.3. Inset shows the Commission Internationale de L'Eclairage (CIE) chromaticity coordinates for the UC spectra of the as prepared samples. The intensity of the bands was found to be increasing with increase in concentration of the Yb^{3+} ions. This shows successful energy transfer from the sensitizer to the activator ions. This might be due to decrease in inter-ionic distance between Yb^{3+} and Tm^{3+} which facilitates the transfer of energy from $Yb^{3+} \rightarrow Tm^{3+}$ ions.

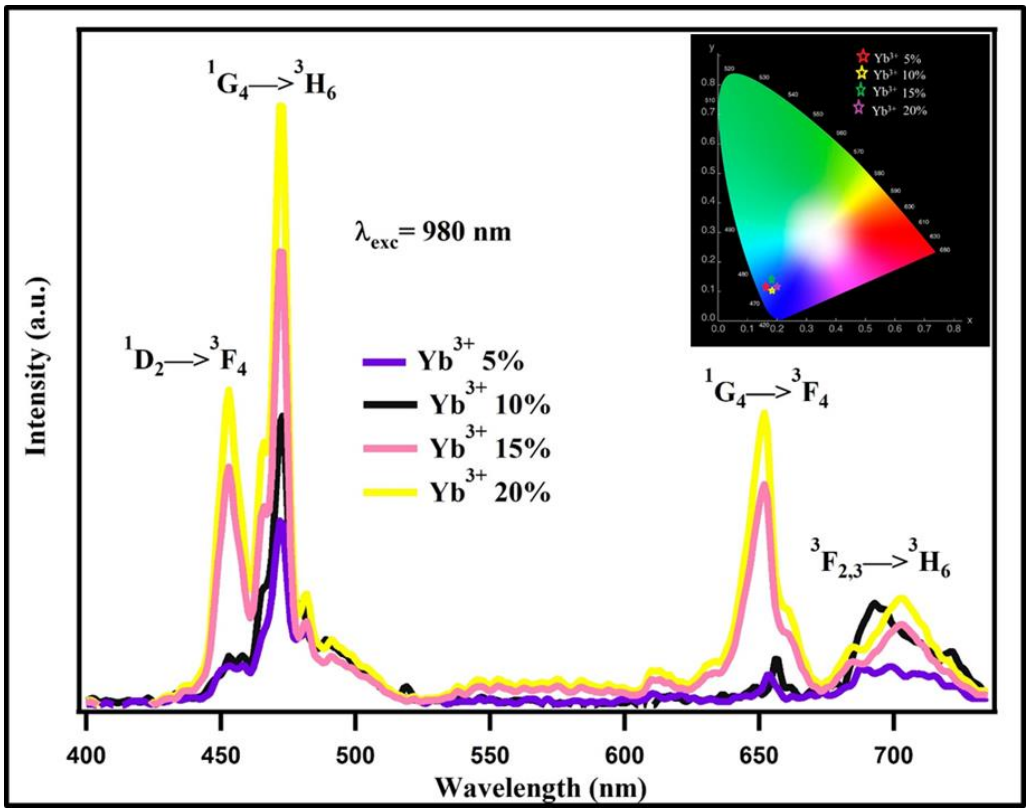

Fig. 5.3: UC spectra of $KGdF_4$: Yb^{3+}(x%)/Tm^{3+} (2%) [x= 5, 10, 15 and 20%] under 980nm CW laser excitation (1W power)

To study the number of NIR photons involved in the up-conversion process, UC spectra under varying powers of 980nm CW laser excitation were studied. Fig. 5.4(a) shows the UC spectra of $KGdF_4$:Yb^{3+} (20%) / Tm^{3+} (2%) samples under varying powers of 980nm CW laser. Fig. 5.4 (b) shows a double logarithmic plot of intensity versus power for all the four bands observed for the same sample. Now, the intensity of visible emission under NIR excitation is

related as the power law enumerated in equation 3.1 in Chapter 3 [180]. Therefore, the slopes of such plots give the required number of photons absorbed for UC emission process.

Now, the values of n for the blue emission at 453nm and 472nm are 2.12 and 2.67 respectively whereas for red emission, the values of n are 1.78 and 1.92 for 650nm and 695nm/700nm transitions. But the expected values for n should be 4 for 453nm emission, 3 for 472/650nm emission and 2 for 695/700nm emissions. This deviation from the values of n reported in literature can be attributed to saturation effect [178,180]. The above relation is valid for low excitation powers. At high excitation powers, the UC process will saturate. The UC process is a non-linear process and exposure to infinite excitation can lead to unsustainability of its non-linear behavior.

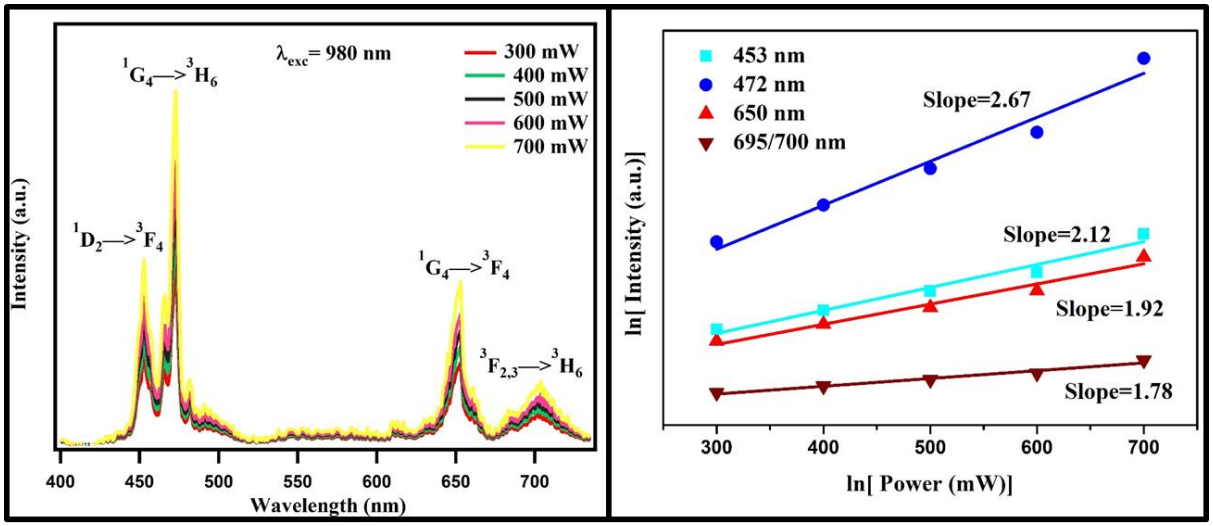

Fig. 5.4: (a) UC spectra of $KGdF_4:Yb^{3+}$ (20%) / Tm^{3+} (2%) sample under varying powers of 980nm CW laser (b) log I vs log P plots for the observed blue and red emissions in the UC process.

Fig. 5.5 shows the schematic energy level diagram showing the various excitation and emission processes involved in the UC process. The Tm^{3+} ions do not absorb the 980nm radiation properly thereby resulting in poor emission. The Yb^{3+} ions on the other hand have a large

absorption cross section for 980nm radiation. On exciting the sample by a 980nm CW laser, the Yb^{3+} ions get promoted from the ground state $^2F_{7/2}$ to the excited state $^2F_{5/2}$. These excited Yb^{3+} ions then transfer their energy to Tm^{3+} ions in ground state $^3H_6$ and promotes them to an upper excited state $^3H_5$ via ground state absorption (GSA). The $^3H_5$ state has short lifetime so the excited Tm^{3+} ions in this state relax to $^3F_4$ state non-radiatively. The ions in this state absorb another 980nm photon and get promoted to $^3F_2$ level via excited state absorption (ESA) process. Some of the ions relax to the lower $^3H_4$ level via the intermediate $^3F_3$ level. Radiative transitions from the $^3F_2$ and $^3F_3$ give rise to the 695nm/700nm emissions. Some of the Tm^{3+} ions in the $^3H_4$ level then absorb another 980nm photon and get excited to the $^1G_4$ level through another ESA process. Radiative transitions from $^1G_4$ state to lower states give rise to the emissions observed at 472nm and 650nm. It is seen that 3 photons are required to populate the $^1G_4$ level. This is known as sequential sensitization. The Tm^{3+} ions in the $^1G_4$ level can absorb another 980nm photon and gets promoted to the $^1D_2$ level via another ESA process. The radiative transitions from this level give rise to the emission at 453nm. Another mechanism is via a cooperative energy transfer (CET) where two excited Yb^{3+} ions in the $^2F_{5/2}$ state interact with each other via dipole-dipole mechanism to form a coupled virtual cluster that is nothing but a virtual excited state. Energy from this state is then transferred to a Tm^{3+} ion in the ground state $^3H_6$ to promote it to the $^1G_4$ level [181,182].

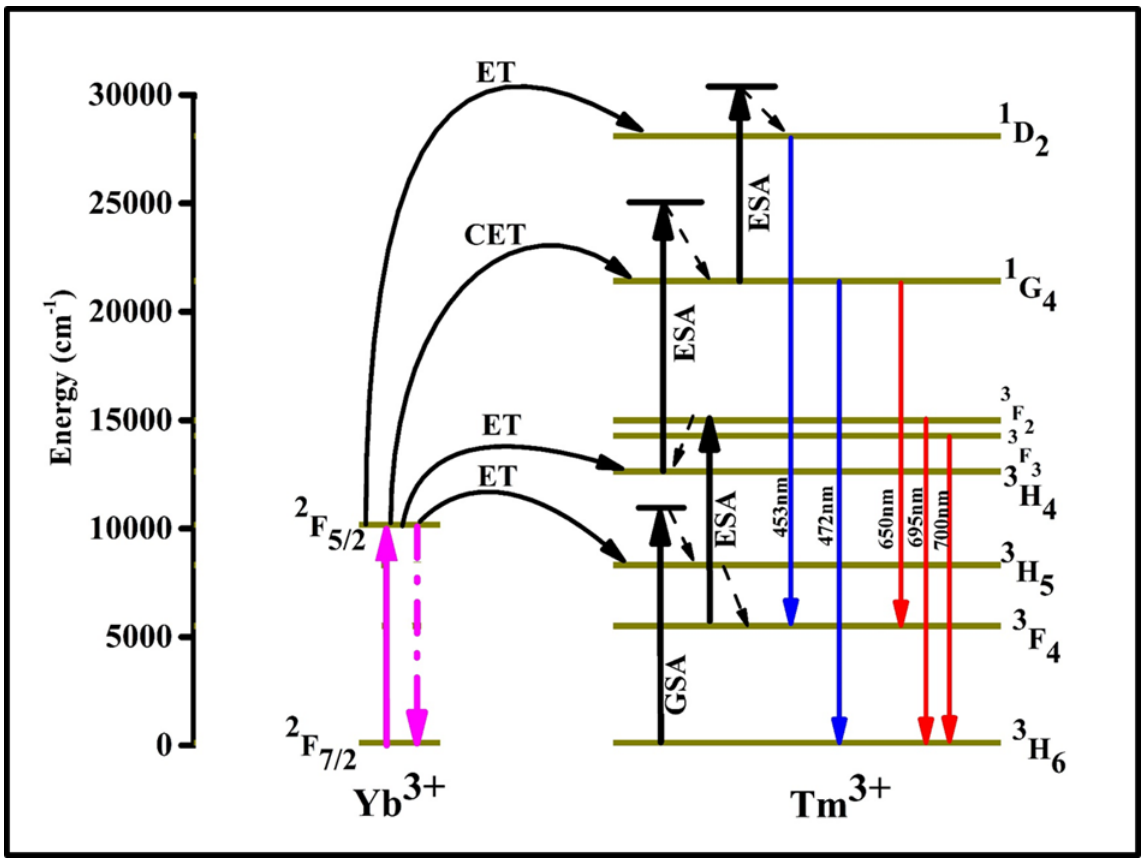

Fig. 5.5: A schematic diagram showing the possible energy transfer mechanisms between Yb^{3+} and Tm^{3+} ions in the UC process

5.3.2.3 Decay kinetics and CIE coordinates

Decay profiles of all the samples at 472nm emission under 980nm CW laser excitation were plotted and are shown in Fig. 5.6. It has been observed that the decay curves are well fitted to a bi-exponential function as given in equation 3.2 in Chapter 3 [89]:

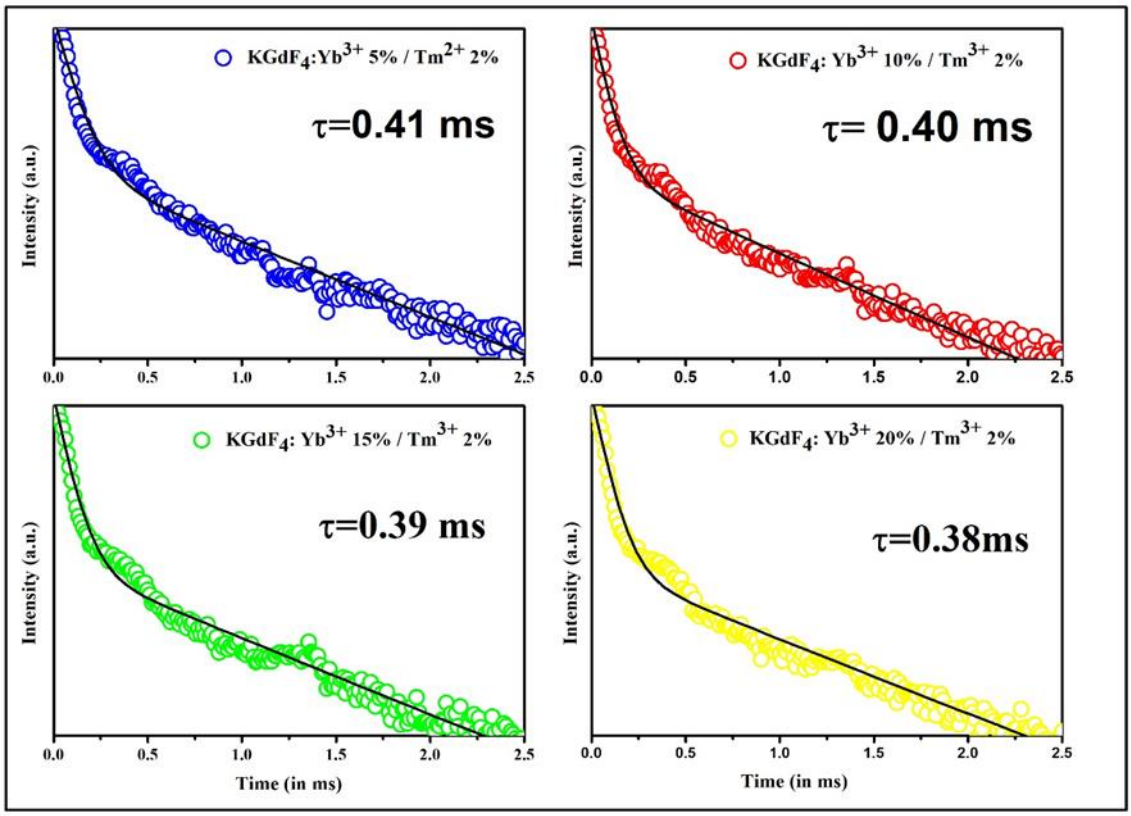

Fig. 5.6: Decay curves of the as prepared samples with functional fitting observed at 472nm emission under 980nm CW laser excitation

This deviation from the single exponential nature can be attributed to the fact that there are ion-ion interactions present in the host lattice along with predominant energy transfers which lead to both slow and fast decay components in the emission as discussed in chapter 3 [93]. The decay times for the samples were found to be 0.41ms, 0.40ms, 0.39ms and 0.38ms for $KGdF_4$: Yb^{3+} (x) / Tm^{3+} (2%); x= 5%, 10%, 15% and 20% respectively. It was seen that the decay times decrease with increase in the concentration of Yb^{3+} ions. This is due to the quenching of $^1G_4$ level of Tm^{3+} due to increase in back energy transfer from $Tm^{3+} \rightarrow Yb^{3+}$ ions. The decay times of the samples along with CIE coordinates are given in Table 5.1.

Table 0.1: Decay times and CIE Coordinates of as prepared $KGdF_4$ UCNPs for UC Studies under 980nm excitation

Concentration of Yb^{3+}	CIE Chromaticity Coordinates		Lifetime (ms)
	X	Y	
5%	0.178	0.112	0.41
10%	0.186	0.105	0.40
15%	0.216	0.262	0.39
20%	0.192	0.117	0.38

5.3.3 EPR Studies

The EPR spectra of the $KGdF_4:Yb^{3+}$ (20%) / Tm^{3+} (2%) sample is shown in Fig. 5.7. The observed g values are shown in the plot itself. The Gd^{3+} ion belongs to the $4f^7$ configuration having zero angular momentum and $^8S_{7/2}$ as its ground state. The observed g values resemble the g values of the "U" spectrum associated with Gd^{3+} ions present in tetrahedral, octahedral or cubic sites with moderate distortions [183,184]. These values are consistent with the values reported in literature. If the Zeeman frequency is larger than the ligand field strength, then it gives a signal at $g \approx 2.0$. If the ligand field strength is larger or comparable to the Zeeman field, then signals are observed in the range $g > 2.0$ [154]. For Gd^{3+}, the observed g values should lie between 2-6. In the present case, due to the anisotropic nature of gadolinium in the UCNPs, some of the g values were less than 2. All these g values can be attributed to weak cubic symmetry fields between the Gd^{3+} ions and the host lattice of the UCNPs [185].

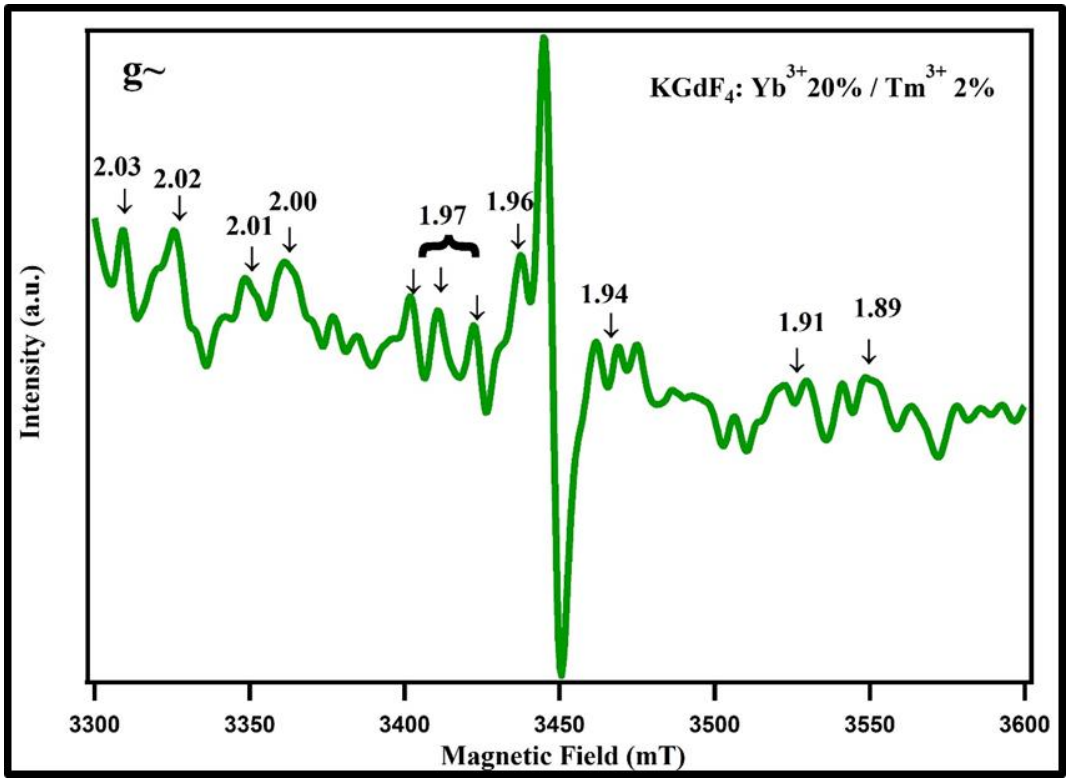

Fig. 5.7: EPR spectra of $KGdF_4:Yb^{3+}$ (20%) / Tm^{3+} (2%) sample. Corresponding g values are marked for reference

5.4 Conclusions

Cubic phase $KGdF_4$: Yb^{3+}(x%)/Tm^{3+} (2%) [x= 5, 10, 15 and 20%] UCNPs were prepared via a wet chemical route. These UCNPs were subjected morphological studies like HR-TEM and EDAX. The sizes of these UCNPs lie in the range of 6-8nm. Luminescence studies like up-conversion were performed. It was observed that the samples are capable of exhibiting the phenomenon of up-conversion as an intense blue emission centred at around 472nm ($^1G_4 \rightarrow {}^3H_6$) under 980nm CW laser excitation was seen. Emission in the red region was also observed corresponding to 650nm ($^1G_4 \rightarrow {}^3F_4$) and 700nm ($^3F_{2,3} \rightarrow {}^3H_6$). The decay profiles showed that the samples have relatively high lifetimes lying in the range of 0.41-0.38ms. EPR studies were performed to study the effects of Gd^{3+} in the host lattice. The observed g values were found to be associated with "U" spectrum which is a characteristic of Gd^{3+} ion. Due to the extremely

small size of these UCNPs (making them usable at cellular level) and the fact that these particles emit intense up-converted light under NIR excitation along with having high lifetimes, these particles can be an exciting replacement of conventional imaging probes in the field of bio-imaging and other bio-photonic applications.

CHAPTER 6: CONCLUSIONS AND FUTURE SCOPE

This chapter summarises the work that has been carried out in developing and characterising RE doped $KGdF_4$ UCNPs. Important results and discussions have been highlighted as well. Lastly, future scope of this work has been discussed in detail as these UCNPs hold immense potential for usage in biological applications.

Potassium Gadolinium Fluoride ($KGdF_4$) UCNPs doped with sensitizer ytterbium (Yb^{3+}) and various activators like erbium (Er^{3+}), terbium (Tb^{3+}) and thulium (Tm^{3+}) were synthesized via a wet chemical route. This synthesis technique yielded cubic phase $KGdF_4$ UCNPs. The interesting thing to note here is that phase of as prepared UCNPs is matching well cubic phase of $NaGdF_4$ nanoparticles. Wet chemical synthesis technique is efficient, cheap and easy-going that yields highly pure sub-10nm cubic phase UCNPs which has not been reported earlier. Host lattices containing alkali metal ions possess low phonon energies thereby giving good luminescence efficiency as has been reported in literature. A potassium based lattice was chosen as potassium systems are less explored when compared with sodium and lithium. It has been established that alkali metal ions enhance the up-conversion efficiency of the host lattice and it has been shown that K^+ ion has the maximum enhancing effect. Therefore the presence of potassium ion in the host lattice provides ideal environment for an efficient and maximum energy transfer therefore satisfying the criteria to develop efficient UC host lattices. As has been highlighted earlier, paramagnetic gadolinium (Gd^{3+}) was added to the host lattice to render these UCNPs favourable for usage in MRI applications as T1/T2 contrasting agents .This makes this UCNP lattice different from other conventional alkali fluoride lattices like $NaYF_4$. Gd^{3+} ion in the host lattice also plays a role of network former and allows to dissolve the dopant rare earths to the extremely high concentrations.

HR-TEM analysis shows highly crystalline UCNP lattice. The UNCPs are circular in shape although they tend to agglomerate due to lack of appropriate surface modifications. XRD and HR-TEM analysis show that the particle sizes of these UCNPs are less than 10nm. The UC efficiency is found to increase when the particle size is below 10nm as compared to the well reported conventional UC lattice $NaYF_4$ that has large sizes. So, these $KGdF_4$ UCNPs are expected to show greater luminescence intensity. EDAX analysis proved successful integration of all the precursor elements in the host lattice.

UC studies highlighted the ability of these UCNPs to emit strong visible emission under 980nm NIR laser excitation. In-depth analysis was conducted to study the energy transfer mechanisms between Yb^{3+} sensitizer and activators like Er^{3+}, Tm^{3+} and Tb^{3+} during the UC process via power-dependent UC studies. Inokuti-Hirayama model was also used to establish the dipole-dipole nature of energy transfer in $KGdF_4:Yb^{3+}/Er^{3+}$ lattice. The UCNPs exhibit high lifetimes which is an added advantage making them useful for future applications in solid state lighting or w-LEDs. These samples are also capable of exhibiting down-conversion as is evident from the strong luminescence these UCNPs emit under UV excitation.To study the effect of gadolinium on the lattice symmetry, EPR studies were also carried out on the as prepared UCNPs. The observed g values belong to the "U" spectrum and can be associated with a weak cubic symmetry field between Gd^{3+} and the host lattice.

Future Scope

- To surface modify $KGdF_4$ UCNPs using available organic reagents.
- To coat the samples with oleic acid, folic acid, polyethylene glycol etc. to so as to render them usable at a cellular level. The presence of organic functional groups like folic acid will allow for testing these samples for targeted imaging and drug delivery applications.
- To use common dyes like rhodamine-b, sodium fluorescein etc. for testing whether or not such samples can be used for differential cell imaging especially of plant cells.
- To study morphological and luminescent properties of $KCeF_4$, KYF_4 and $KLaF_4$ lattices and expand the immense scope of research in this field.
- To synthesize and study RE-$KGdF_4$@$KGdF_4$ core shell UCNPs since core-shell UCNPs are known to exhibit higher luminescence efficiency.

REFERENCES

[1] N. Bloembergen, Solid State Infrared Quantum Counters, Phys. Rev. Lett. 2 (1959) 84-85 https://doi.org/10.1103/PhysRevLett.2.84

[2] C. Zhang, L. Sun, Y. Zhang, C. Yan, Rare earth upconversion nanophosphors: Synthesis, functionalization and application as biolabels and energy transfer donors, J. Rare Earths. 28 (2010) 807–819. https://doi.org/10.1016/S1002-0721(09)60206-4.

[3] X. Li, F. Zhang, D. Zhao, Highly efficient lanthanide upconverting nanomaterials: Progresses and challenges, Nano Today. 8 (2013) 643–676. https://doi.org/10.1016/j.nantod.2013.11.003.

[4] J.F. Loo, Y. Chien, F. Yin, S. Kong, H. Ho, K. Yong, Upconversion and downconversion nanoparticles for biophotonics and nanomedicine, Coord. Chem. Rev. 400 (2019) 213042. https://doi.org/10.1016/j.ccr.2019.213042.

[5] L.N. Nanoparticles, M. Nyk, D. Wawrzynczyk, K. Parjaszewski, M. Samoc, Spectrally Resolved Nonlinear Optical Response of Upconversion, (2011) 16849–16855.

[6] M. Haase, H. Schäfer, Upconverting Nanoparticles Angewandte, (2011) 5808–5829. https://doi.org/10.1002/anie.201005159.

[7] A. Francois, Upconversion and anti-stokes processes with f and d ions in solids, Chem. Rev. 104 (2004) 139–173.

[8] J. Yao, C. Huang, C. Liu, M. Yang, Talanta Upconversion luminescence nanomaterials : A versatile platform for imaging , sensing , and therapy, Talanta. 208 (2020) 120157. https://doi.org/10.1016/j.talanta.2019.120157.

[9] D.R. Gamelin, H.U. Gudel, Upconversion Processes in Transition Metal and Rare Earth

Metal Systems, in: H. Yersin (Ed.), Transit. Met. Rare Earth Compd. Excit. States, Transitions, Interact. II, Springer Berlin Heidelberg, Berlin, Heidelberg, 2001: pp. 1–56. https://doi.org/10.1007/3-540-44474-2_1.

[10] M. Oheim, D.J. Michael, M. Geisbauer, D. Madsen, R.H. Chow, Principles of two-photon excitation fluorescence microscopy and other nonlinear imaging approaches , Adv. Drug Deliv. Rev. 58 (2006) 788–808. https://doi.org/10.1016/j.addr.2006.07.005.

[11] L.R. Dalton, A.W. Harper, R. Ghosn, W.H. Steier, M. Ziarj, H. Fetterman, Y. Shi, R. V Mustacich, K.J. Shea, Synthesis and Processing of Improved Organic Second-Order Nonlinear Optical Materials for Applications in Photonics,Chem. Mater. 7 (1995) 1060–1081.

[12] F. Wang, X. Liu, Recent advances in the chemistry of lanthanide-doped upconversion nanocrystals, Chem. Soc. Rev. 38 (2009) 976–989. https://doi.org/10.1039/b809132n.

[13] M. Wang, G. Abbineni, A. Clevenger, C. Mao, S. Xu, Upconversion nanoparticles: Synthesis, surface modification and biological applications, Nanomedicine:NBM 7 (2011) 710–729. https://doi.org/10.1016/j.nano.2011.02.013.

[14] E. Hong, L. Liu, L. Bai, C. Xia, L. Gao, L. Zhang, Control synthesis , subtle surface modification of rare-earth-doped upconversion nanoparticles and their applications in cancer diagnosis and treatment, Mater. Sci. Eng. C. 105 (2019) 110097. https://doi.org/10.1016/j.msec.2019.110097.

[15] J.S. Chivian, W.E. Case, D.D. Eden, The photon avalanche: A new phenomenon in Pr^{3+} based infrared quantum counters, Appl. Phys. Lett. 35 (1979) 124–125. https://doi.org/10.1063/1.91044.

[16] N. Malik, T. Arfin, A.U. Khan, Graphene nanomaterials: chemistry and pharmaceutical

perspectives, Nanomaterials for Drug Delivery and Therapy, Elsevier Inc., 2019, pp. 373-402 https://doi.org/10.1016/b978-0-12-816505-8.00002-3.

[17] L.Q. Xiong, Z.G. Chen, M.X. Yu, F.Y. Li, C. Liu, C.H. Huang, Synthesis, characterization, and in vivo targeted imaging of amine-functionalized rare-earth up-converting nanophosphors, Biomaterials. 30 (2009) 5592–5600. https://doi.org/10.1016/j.biomaterials.2009.06.015.

[18] F. Liu, X. He, L. Liu, H. You, H. Zhang, Z. Wang, Conjugation of $NaGdF_4$ upconverting nanoparticles on silica nanospheres as contrast agents for multi-modality imaging, Biomaterials. 34 (2013) 5218–5225. https://doi.org/10.1016/j.biomaterials.2013.03.058.

[19] M.S. Ghamsari, Introductory Chapter: Nano-bioimaging—Past, Present, and Future, Intech, 2016, pp 1-9 http://dx.doi.org/10.5772/intechopen.74959

[20] R. Vadivambal, D.S. Jayas, Bio-Imaging Principles, Techniques, and Applications, CRC Press, Taylor and Francis Group, 2016.

[21] Y. Wang, Y. Li, F. Wei, Y. Duan, Optical Imaging Paves the Way for Autophagy Research, Trends Biotechnol. 35 (2017) 1181–1193. https://doi.org/10.1016/j.tibtech.2017.08.006.

[22] S. Huang, Y. Chen, B. Liu, F. He, P. Ma, X. Deng, Z. Cheng, J. Lin, Synthesis of magnetic and upconversion nanocapsules as multifunctional drug delivery system, J. Solid State Chem. 229 (2015) 322–329. https://doi.org/10.1016/j.jssc.2015.06.024.

[23] X. Mou, J. Wang, X. Meng, J. Liu, L. Shi, L. Sun, Multifunctional nanoprobe based on upconversion nanoparticles for luminescent sensing and magnetic resonance imaging, J. Lumin. 190 (2017) 16–22. https://doi.org/10.1016/j.jlumin.2017.05.006.

[24] H. Bin Na, J.H. Lee, K. An, Y. Il Park, M. Park, I.S. Lee, D.H. Nam, S.T. Kim, S.H.

Kim, S.W. Kim, K.H. Lim, K.S. Kim, S.O. Kim, T. Hyeon, Development of a T1 contrast agent for magnetic resonance imaging using MnO nanoparticles, Angew. Chem. Int. Ed. 46 (2007) 5397–5401. https://doi.org/10.1002/anie.200604775.

[25] H. Hifumi, S. Yamaoka, A. Tanimoto, D. Citterio, K. Suzuki, Gadolinium-based hybrid nanoparticles as a positive MR contrast agent, J. Am. Chem. Soc. 128 (2006) 15090–15091. https://doi.org/10.1021/ja066442d.

[26] M.A. Fortin, R.M. Petoral, F. Söoderlind, A. Klasson, M. Engströom, T. Veres, P.O. Käll, K. Uvdal, Polyethylene glycol-covered ultra-small Gd_2O_3 nanoparticles for positive contrast at 1.5 T magnetic resonance clinical scanning, Nanotechnology 18 (2007) 395501. https://doi.org/10.1088/0957-4484/18/39/395501.

[27] M. Nyk, R. Kumar, T.Y. Ohulchanskyy, E.J. Bergey, P.N. Prasad, High Contrast in Vitro and in Vivo Photoluminescence Bioimaging Using Near Infrared to Near Infrared Up-Conversion in Tm^{3+} and Yb^{3+} Doped Fluoride Nanophosphors, Nano Lett. 8 (2008) 3834-3838.

[28] A. Diaspro , M.A.M.J van Zandvoort , Super-Resolution Imaging in Biomedicine, CRC Press, Taylor & Francis Group, 2017.

[29] Y. Peeters, W. Vandenberg, S. Duwé, A. Bouwens, T. Lukes, C. Ruckebusch, T. Lasser, P. Dedecker, Correcting for photodestruction in super-resolution optical fluctuation imaging, Sci. Rep. 7 (2017) 10470. https://doi.org/10.1038/s41598-017-09666-4.

[30] R. Heintzmann, T. Huser, Super-Resolution Structured Illumination Microscopy, Chem. Rev. 117 (2017) 13890-13908 . https://doi.org/10.1021/acs.chemrev.7b00218.

[31] E. Hanssen, Cellular Imaging: Electron Tomography and Related Techniques, Springer International Publishing, 2018

[32] M. Hauser, M. Wojcik, D. Kim, M. Mahmoudi, W. Li, K. Xu, Correlative Super-Resolution Microscopy : New Dimensions and New Opportunities, Chem. Rev. 117 (2017) 7428-7456. https://doi.org/10.1021/acs.chemrev.6b00604.

[33] J. Demmerle, C. Innocent, A.J. North, G. Ball, M. Müller, A. Matsuda, I.M. Dobbie, Y. Markaki, L. Schermelleh, Strategic and practical guidelines for successful structured illumination microscopy, Nat. Protoc. 12 (2017) 988-1010. https://doi.org/10.1038/nprot.2017.019.

[34] J.L. Ponsetto , A. Bezryadina , F. Wei, K. Onishi , H. Shen , E. Huang , L. Ferrari , Q. Ma , Y. Zou , Z. Liu, Experimental Demonstration of Localized Plasmonic Structured Illumination Microscopy, ACS Nano 11 (2017) 5344-5350. https://doi.org/10.1021/acsnano.7b01158.

[35] S. So, M. Kim, D. Lee, D.M. Nguyen, J. Rho, Overcoming diffraction limit : From microscopy to nanoscopy, Appl. Spectrosc. Rev. 53 (2018) 290-317. https://doi.org/10.1080/05704928.2017.1323309.

[36] J.W.M. Bulte, M.M.J. Modo, Design and Applications of Nanoparticles in Biomedical Imaging, Springer International Publishing, 2017.

[37] S. Goel, C.G. England, F. Chen, W. Cai, Positron emission tomography and nanotechnology: A dynamic duo for cancer theranostics, Adv. Drug Deliv. Rev. 113 (2017) 157-176. https://doi.org/10.1016/j.addr.2016.08.001.

[38] A. Zebibula, N. Alifu, L. Xia, C. Sun, X. Yu, Ultrastable and Biocompatible NIR-II Quantum Dots for Functional Bioimaging, Adv. Funct. Mater. 28 (2018) 1703451. https://doi.org/10.1002/adfm.201703451.

[39] X. Wang, Y. Li, Monodisperse nanocrystals: General synthesis, assembly, and their

applications, Chem. Commun. (28) (2007) 2901–2910. https://doi.org/10.1039/b700183e.

[40] T. Jamieson, R. Bakhshi, D. Petrova, R. Pocock, M. Imani, A.M. Seifalian, Biological applications of quantum dots, Biomaterials. 28 (2007) 4717–4732. https://doi.org/10.1016/j.biomaterials.2007.07.014.

[41] J. Shen, L.D. Sun, C.H. Yan, Luminescent rare earth nanomaterials for bioprobe applications, Dalt. Trans. 9226 (2008) 5687–5697. https://doi.org/10.1039/b805306e.

[42] A.M. Smith, X. Gao, S. Nie, Quantum Dot Nanocrystals for In Vivo Molecular and Cellular Imaging, Photochem. Photobiol. 80 (2004) 377-385. https://doi.org/10.1562/2004-06-21-ir-209.1.

[43] W.C.W. Chan, S. Nie, Quantum dot bioconjugates for ultrasensitive nonisotopic detection, Science 281 (1998) 2016–2018. https://doi.org/10.1126/science.281.5385.2016.

[44] Q.Q. Dou, H.C. Guo, E. Ye, Near-infrared upconversion nanoparticles for bio-applications, Mater. Sci. Eng. C. 45 (2015) 635–643. https://doi.org/10.1016/j.msec.2014.03.056.

[45] Z. Li, H. Yuan, W. Yuan, Q. Su, F. Li, Upconversion nanoprobes for biodetections, Coord. Chem. Rev. (2017) 1–14. https://doi.org/10.1016/j.ccr.2017.06.025.

[46] J. Shen, L. Zhao, G. Han, Lanthanide-doped upconverting luminescent nanoparticle platforms for optical imaging-guided drug delivery and therapy, Adv. Drug Deliv. Rev. 65 (2013) 744–755. https://doi.org/10.1016/j.addr.2012.05.007.

[47] L.C. Ong, K. Gnanasammandhan, S. Nagarajan, Y. Zhang, Upconversion : road to El Dorado of the fluorescence world,Luminescence 25 (2010) 290–293.

https://doi.org/10.1002/bio.1229.

[48] L. Cheng, K. Yang, M. Shao, S.T. Lee, Z. Liu, Multicolor In Vivo Imaging of Upconversion Nanoparticles with Emissions Tuned by Luminescence Resonance Energy Transfer, J. Phys. Chem. C (2011) 2686–2692.

[49] A. Verma, V.M. Rotello, Surface recognition of biomacromolecules using nanoparticle receptors, Chem. Commun. (3)(2005) 303–312. https://doi.org/10.1039/b410889b.

[50] Y. Pu, J. Leng, D. Wang, J. Wang, N.R. Foster, J. Chen, Recent progress in the green synthesis of rare-earth doped upconversion nanophosphors for optical bioimaging from cells to animals, Chinese J. Chem. Eng. 26 (2018) 2206–2218. https://doi.org/10.1016/j.cjche.2018.03.005.

[51] J.M.F. Van Dijk, M.F.H. Schuurmans, On the nonradiative and radiative decay rates and a modified exponential energy gap law for 4f-4f transitions in rare-earth ions, J. Chem. Phys. 78 (1983) 5317–5323. https://doi.org/10.1063/1.445485.

[52] S. Heer, K. Kömpe, H. Güdel, M. Haase, Highly Efficient Multicolour Upconversion Emission in Transparent Colloids of Lanthanide-Doped $NaYF_4$ Nanocrystals, Adv. Mater. 16 (2004) 2102–2105. https://doi.org/10.1002/adma.200400772.

[53] H. Mai, Y. Zhang, R. Si, Z. Yan, L. Sun, L. You, C. Yan, High-Quality Sodium Rare-Earth Fluoride Nanocrystals : Controlled Synthesis and Optical Properties, J. Am. Chem. Soc. 128 (2006) 6426–6436. https://doi.org/10.1021/ja060212h.

[54] L. Liang, H. Wu, H. Hu, M. Wu, Q. Su, Enhanced blue and green upconversion in hydrothermally synthesized hexagonal $NaY_{1-x}Yb_xF_4:Ln^{3+}$ (Ln^{3+} = Er^{3+} or Tm^{3+}), J. Alloys Compd. 368 (2004) 94–100. https://doi.org/10.1016/j.jallcom.2003.07.010.

[55] G.Blasse, B.C. Grabmaier, A General Introduction to Luminescent Materials, in:

Luminescent Materials, Springer -Verlag Berlin Heidelberg, 1994, pp. 1–9.

[56] H.X. Mai, Y.W. Zhang, L.D. Sun, C.H. Yan, Highly efficient multicolor up-conversion emissions and their mechanisms of monodisperse $NaYF_4$:Yb,Er core and core/shell-structured nanocrystals, J. Phys. Chem. C. 111 (2007) 13721–13729. https://doi.org/10.1021/jp073920d.

[57] L. Guo, Y. Wang, Y. Wang, J. Zhang, P. Dong, W. Zeng, Structure, enhancement and white luminescence of multifunctional $Lu_6O_5F_8$:20%Yb^{3+},1%Er^{3+}(Tm^{3+}) nanoparticles via further doping with Li^+ under different excitation sources, Nanoscale 5 (2013) 2491-2504. https://doi.org/10.1039/c2nr33577h.

[58] Y. Li, X. Li, Z. Xue, M. Jiang, S. Zeng, M^{2+} Doping Induced Simultaneous Phase / Size Control and Remarkable Enhanced Upconversion Luminescence of $NaLnF_4$ Probes for Optical-Guided Tiny Tumor Diagnosis, Adv. Healthc. Mater. 6 (2017) 1601231. https://doi.org/10.1002/adhm.201601231.

[59] G. Yi, G. Chow, Colloidal LaF_3 : Yb,Er, LaF_3 : Yb, Ho and LaF_3 : Yb,Tm nanocrystals with multicolor upconversion fluorescence, J. Mater. Chem. 15 (2005) 4460–4464. https://doi.org/10.1039/b508240d.

[60] G. Yi, H. Lu, S. Zhao, Y. Ge, W. Yang, Synthesis , Characterization , and Biological Application of Size-Controlled Nanocrystalline $NaYF_4$:Yb,Er Infrared-to-visible Up-conversion Phosphors, Nano Letters 4 (2004) 2191-2196.

[61] Y. Zhang, X. Sun, R. Si, L. You, C. Yan, Single-Crystalline and Monodisperse LaF_3 Triangular Nanoplates from a Single-Source Precursor, J. Am. Chem. Soc. 127 (2005) 3260–3261. https://doi.org/10.1021/ja042801y.

[62] J. Boyer, F. Vetrone, L.A. Cuccia, J.A. Capobianco, Q.C. Hb, I. National, D. Recherche,

Synthesis of Colloidal Upconverting $NaYF_4$ Nanocrystals Doped with Er^{3+}, Yb^{3+} and Tm^{3+}, Yb^{3+} via Thermal Decomposition of Lanthanide Trifluoroacetate Precursors, J. Am.Chem. Soc. 128 (2006) 7444–7445.

[63] K. Nigoghossian, S. Ouellet, J. Plain, Y. Messaddeq, D. Boudreau, S.J. Ribeiro, Upconversion nanoparticle-decorated gold nanoshells for near-infrared induced heating and thermometry, J. Mater. Chem. B 5 (2017) 7109-7117. https://doi.org/10.1039/C7TB01621B.

[64] Y. Sun, Y. Chen, L. Tian, Y. Yu, X. Kong, J. Zhao, H. Zhang, Controlled synthesis and morphology dependent upconversion luminescence of $NaYF_4$:Yb, Er nanocrystals, Nanotechnology. 18 (2007) 275609. https://doi.org/10.1088/0957-4484/18/27/275609.

[65] P. Du, A.M. Deng, L. Luo, J.S. Yu, Simultaneous phase and size manipulation in $NaYF_4$:Er^{3+}/Yb^{3+} upconverting nanoparticles for a non-invasion optical thermometer, New J. Chem. 41 (2017) 13855–13861. https://doi.org/10.1039/c7nj03165c.

[66] F. Wang, D.K. Chatterjee, Z. Li, Y. Zhang, X. Fan, M. Wang, Synthesis of polyethylenimine/$NaYF_4$ nanoparticles with upconversion fluorescence, Nanotechnology. 17 (2006) 5786–5791. https://doi.org/10.1088/0957-4484/17/23/013.

[67] M. Wang, J.L. Liu, Y.X. Zhang, W. Hou, X.L. Wu, S.K. Xu, Two-phase solvothermal synthesis of rare-earth doped $NaYF_4$ upconversion fluorescent nanocrystals, Mater. Lett. 63 (2009) 325–327. https://doi.org/10.1016/j.matlet.2008.10.028.

[68] M. Wang, C.C. Mi, J.L. Liu, X.L. Wu, Y.X. Zhang, W. Hou, F. Li, S.K. Xu, One-step synthesis and characterization of water-soluble $NaYF_4$:Yb,Er/Polymer nanoparticles with efficient up-conversion fluorescence, J. Alloys Compd. 485 (2009) 24–27. https://doi.org/10.1016/j.jallcom.2009.05.138.

[69] J. Zhao, Y. Sun, X. Kong, L. Tian, Y. Wang, L. Tu, J. Zhao, H. Zhang, Controlled synthesis, formation mechanism, and great enhancement of red upconversion luminescence of $NaYF_4$:Yb^{3+}, Er^{3+} nanocrystals/submicroplates at low doping level, J. Phys. Chem. B. 112 (2008) 15666–15672. https://doi.org/10.1021/jp805567k.

[70] X. Chen, W. Wang, X. Chen, J. Bi, L. Wu, Z. Li, X. Fu, Microwave hydrothermal synthesis and upconversion properties of $NaYF_4$:Yb^{3+}, Tm^{3+} with microtube morphology, Mater. Lett. 63 (2009) 1023–1026. https://doi.org/10.1016/j.matlet.2009.01.075.

[71] H. Park, G. Yeol, M. Kim, K. Kim, C. Lee, S. Park, W. Kim, Thin film fabrication of upconversion lanthanide-doped $NaYF_4$ by a sol-gel method and soft lithographical nanopatterning, J. Alloys Compd. 728 (2017) 927–935. https://doi.org/10.1016/j.jallcom.2017.09.076.

[72] Z. Liang, X. Wang, W. Zhu, P. Zhang, Y. Yang, C. Sun, Upconversion Nanocrystals Mediated Lateral-Flow Nanoplatform for In Vitro Detection, ACS Appl. Mater. Interfaces 9 (2017) 3497-3504. https://doi.org/10.1021/acsami.6b14906.

[73] L.P. Qian, D. Yuan, G.S. Yi, G.M. Chow, Critical shell thickness and emission enhancement of $NaYF_4$:Yb,Er/$NaYF_4$/silica core/shell/shell nanoparticles, J. Mater. Res. 24 (2009) 3559–3568. https://doi.org/10.1557/jmr.2009.0432.

[74] L. Wang, W. Zhao, W. Tan, Bioconjugated silica nanoparticles: Development and applications, Nano Res. 1 (2008) 99–115. https://doi.org/10.1007/s12274-008-8018-3.

[75] Z. Li, Y. Zhang, Monodisperse silica-coated polyvinyl-pyrrolidone/$NaYF_4$ nanocrystals with multicolor upconversion fluorescence emission, Angew. Chem. Int. Ed. 45 (2006) 7732–7735. https://doi.org/10.1002/anie.200602975.

[76] Z. Li, Y. Zhang, S. Jiang, Multicolor core/shell-structured upconversion fluorescent nanoparticles, Adv. Mater. 20 (2008) 4765–4769. https://doi.org/10.1002/adma.200801056.

[77] H. Lu, G. Yi, S. Zhao, D. Chen, L.H. Guo, J. Cheng, Synthesis and characterization of multi-functional nanoparticles possessing magnetic, up-conversion fluorescence and bio-affinity properties, J. Mater. Chem. 14 (2004) 1336–1341. https://doi.org/10.1039/b315103d.

[78] C. Mi, J. Zhang, H. Gao, X. Wu, M. Wang, Y. Wu, Y. Di, Z. Xu, C. Mao, S. Xu, Multifunctional nanocomposites of superparamagnetic (Fe_3O_4) and NIR-responsive rare earth-doped up-conversion fluorescent ($NaYF_4$:Yb,Er) nanoparticles and their applications in biolabeling and fluorescent imaging of cancer cells, Nanoscale. 2 (2010) 1141-1148. https://doi.org/10.1039/c005273f.

[79] G.S. Yi, G.M. Chow, Synthesis of hexagonal-phase $NaYF_4$:Yb,Er and $NaYF_4$:Yb,Tm nanocrystals with efficient up-conversion fluorescence, Adv. Funct. Mater. 16 (2006) 2324–2329. https://doi.org/10.1002/adfm.200600053.

[80] Z. Chen, H. Chen, H. Hu, M. Yu, F. Li, Q. Zhang, Z. Zhou, T. Yi, C. Huang, Versatile synthesis strategy for carboxylic acid-functionalized upconverting nanophosphors as biological labels, J. Am. Chem. Soc. 130 (2008) 3023–3029. https://doi.org/10.1021/ja076151k.

[81] L.I.U. Zhengyi, G.S. Yi, G.G.M. Chow, Core / Shell / Shell Nanoparticles with Significant Enhancement of Upconversion Fluorescence, Chem. Mater. 19 (2007) 341–343. https://doi.org/10.1021/cm062447y.

[82] L. Wang, R. Yan, Z. Huo, L. Wang, J. Zeng, J. Bao, X. Wang, Q. Peng, Y. Li, Fluorescence resonant energy transfer biosensor based on upconversion-luminescent

nanoparticles, Angew. Chem. Int. Ed. 44 (2005) 6054–6057. https://doi.org/10.1002/anie.200501907.

[83] D.K. Chatterjee, A.J. Rufaihah, Y. Zhang, Upconversion fluorescence imaging of cells and small animals using lanthanide doped nanocrystals, Biomaterials. 29 (2008) 937–943. https://doi.org/10.1016/j.biomaterials.2007.10.051.

[84] S.F. Lim, R. Riehn, W.S. Ryu, N. Khanarian, C.K. Tung, D. Tank, R.H. Austin, In vivo and scanning electron microscopy imaging of upconverting nanophosphors in Caenorhabditis elegans, Nano Lett. 6 (2006) 169–174. https://doi.org/10.1021/nl0519175.

[85] S. Sinha, M.K. Mahata, H.C. Swart, A. Kumar, K. Kumar, Enhancement of upconversion, temperature sensing and cathodoluminescence in the K^+/Na^+ compensated $CaMoO_4:Er^{3+}/Yb^{3+}$ nanophosphor, New J. Chem. 41 (2017) 5362–5372. https://doi.org/10.1039/c7nj00086c.

[86] A. Maurya, A. Bahadur, A. Dwivedi, A.K. Choudhary, T.P. Yadav, P.K. Vishwakarma, S.B. Rai, Optical properties of Er^{3+}, Yb^{3+} co-doped calcium zirconate phosphor and temperature sensing efficiency: Effect of alkali ions (Li^+, Na^+ and K^+), J. Phys. Chem. Solids. 119 (2018) 228–237. https://doi.org/10.1016/j.jpcs.2018.04.004.

[87] H.N. Luitel, R. Chand, T. Torikai, M. Yada, T. Watari, Highly efficient NIR-NIR upconversion in potassium substituted $CaMoO_4:Tm^{3+}$, Yb^{3+}phosphor for potential biomedical applications, RSC Adv. 5 (2015) 17034–17040. https://doi.org/10.1039/c4ra12436g.

[88] Q. Ju, D. Tu, Y. Liu, R. Li, H. Zhu, J. Chen, Z. Chen, M. Huang, X. Chen, Amine-functionalized lanthanide-doped $KGdF_4$ nanocrystals as potential optical/magnetic multimodal bioprobes, J. Am. Chem. Soc. 134 (2012) 1323–1330.

https://doi.org/10.1021/ja2102604.

[89] S. Kaur, A.S. Rao, M. Jayasimhadri, Color tunability and energy transfer studies of Dy^{3+}/Eu^{3+} co-doped calcium aluminozincate phosphor for lighting applications, Mater. Res. Bull. 116 (2019) 79–88. https://doi.org/10.1016/j.materresbull.2019.04.022.

[90] S. Kaur, N. Deopa, A. Prasad, R. Bajaj, A.S. Rao, Intense green emission from Tb^{3+} ions doped zinc lead alumino borate glasses for laser and w-LEDs applications, Opt. Mater. 84 (2018) 318-323. https://doi.org/10.1016/j.optmat.2018.07.020.

[91] N. Deopa, A.S. Rao, Photoluminescence and energy transfer studies of Dy^{3+} ions doped lithium lead alumino borate glasses for w-LED and laser applications, J. Lumin. 192 (2017) 832–841. https://doi.org/10.1016/j.jlumin.2017.07.052.

[92] S. Ahmad, G.V. Prakash, R. Nagarajan, Hexagonally ordered $KLaF_4$ host: Phase-controlled synthesis and luminescence studies, Inorg. Chem. 51 (2012) 12748–12754. https://doi.org/10.1021/ic301566e.

[93] A. Prasad, A.S. Rao, M. Gupta, G.V. Prakash, Morphological and luminescence studies on $KGdF_4:Yb^{3+}/Tb^{3+}$ up-conversion nanophosphors, Mater. Chem. Phys. 219 (2018) 13–21. https://doi.org/10.1016/j.matchemphys.2018.07.056.

[94] B.D. Cullity, Elements of Diffraction, Addison-Wesley Publishing Company Inc., 1978.

[95] J.J.Hren, J. I. Goldstein, D.C. Joy, Introduction to Analytical Electron Microscopy, Springer Science+Business Media LLC,New York, 1979

[96] H.H. Rose, Optics of high-performance electron microscopes, Sci. Technol. Adv. Mater. 9 (2008) 14107. https://doi.org/10.1088/0031-8949/9/1/014107.

[97] F. Wang, Y. Han, C.S. Lim, Y. Lu, J. Wang, J. Xu, H. Chen, C. Zhang, M. Hong, X. Liu, Simultaneous phase and size control of upconversion nanocrystals through

lanthanide doping, Nature. 463 (2010) 1061–1065. https://doi.org/10.1038/nature08777.

[98] T. Trupke, A. Shalav, B.S. Richards, P. Wu, Efficiency enhancement of solar cells by luminescent up-conversion of sunlight, Sol. Energy Mater. Sol. Cells 90 (2006) 3327–3338. https://doi.org/10.1016/j.solmat.2005.09.021.

[99] K.W. Kramer, D. Biner, G. Frei, H.U. Gudel, M.P. Hehlen, S.R. Luthi, Hexagonal Sodium Yttrium Fluoride Based Green and Blue Emitting Upconversion Phosphors, Chem. Mater. 16 (2004) 1244–1251.

[100] J.C. Zhou, Z.L. Yang, W. Dong, R.J. Tang, L.D. Sun, C.H. Yan, Bioimaging and toxicity assessments of near-infrared upconversion luminescent $NaYF_4$:Yb,Tm nanocrystals, Biomaterials. 32 (2011) 9059–9067. https://doi.org/10.1016/j.biomaterials.2011.08.038.

[101] G. Tian, X. Zheng, X. Zhang, W. Yin, J. Yu, D. Wang, Z. Zhang, X. Yang, Z. Gu, Y. Zhao, TPGS-stabilized $NaYbF_4$:Er Upconversion nanoparticles for dual-modal fluorescent/CT imaging and anticancer drug delivery to overcome multi-drug resistance, Biomaterials. 40 (2015) 107–116. https://doi.org/10.1016/j.biomaterials.2014.11.022.

[102] D. Yang, X. Kang, P. Ma, Y. Dai, Z. Hou, Z. Cheng, C. Li, J. Lin, Hollow structured upconversion luminescent $NaYF_4$:Yb^{3+}, Er^{3+} nanospheres for cell imaging and targeted anti-cancer drug delivery, Biomaterials. 34 (2013) 1601–1612. https://doi.org/10.1016/j.biomaterials.2012.11.004.

[103] T. Konishi, M .Yamada, K. Soga, D. Matsuura, Y. Nagasaki, PEG based Surface Modification on Upconversion Nanophosphors for Bio-imaging under IR excitation, J. Photopolym. Sci. Tec. 19 (2006) 145–149.

[104] T. Konishi, K. Shimizu, Y. Saito, K. Soga, Surface modification of upconversion nanophoshors with poly(acrylic acid), J. Photopolym. Sci. Tec. 20 (2007) 11–15.

[105] W. Feng, X. Zhu, F. Li, Recent advances in the optimization and functionalization of upconversion nanomaterials for in vivo bioapplications, 5 (2013) e75-15. https://doi.org/10.1038/am.2013.63.

[106] R. Wang, X. Zhang, F. Liu, L. Xiao, Y. Chen, L. Liu, Upconversion mechanisms of Er^{3+} :$NaYF_4$ and thermal effects induced by incident photon on the green luminescence, J. Lumin. 175 (2016) 35–43. https://doi.org/10.1016/j.jlumin.2016.02.018.

[107] A. Sarakovskis, G. Krieke, G. Doke, J. Grube, L. Grinberga, M. Springis, Comprehensive study on different crystal field environments in highly efficient $NaLaF_4$:Er^{3+} upconversion phosphor, Opt. Mater. 39 (2015) 90–96. https://doi.org/10.1016/j.optmat.2014.11.004.

[108] L.W. Yang, Y.Y. Zhang, J.J. Li, Y. Li, J.X. Zhong, P.K. Chu, Magnetic and upconverted luminescent properties of multifunctional lanthanide doped cubic $KGdF_4$ nanocrystals, Nanoscale. 2 (2010) 2805–2810. https://doi.org/10.1039/c0nr00326c.

[109] G. Wang, Q. Peng, Y. Li, Upconversion Luminescence of Monodisperse CaF_2:Yb^{3+}/Er^{3+} Nanocrystals, J. Am. Chem. Soc. 131 (2009) 14200-14201.

[110] H.T. Wong, F. Vetrone, R. Naccache, H.L.W. Chan, J. Hao, J.A. Capobianco, Water dispersible ultra-small multifunctional $KGdF_4$:Tm^{3+},Yb^{3+} nanoparticles with near-infrared to near-infrared upconversion, J. Mater. Chem. 21 (2011) 16589–16596. https://doi.org/10.1039/c1jm12796a.

[111] C. Cao, H.K. Yang, B.K. Moon, B.C. Choi, J.H. Jeong, K.H. Kim, Synthesis, phase composition modification, and optical properties of Ce^{3+}/Tb^{3+} activated $KGdF_4$ and GdF_3 submicrocrystals, J. Solid State Chem. 187 (2012) 45–50. https://doi.org/10.1016/j.jssc.2011.12.041.

[112] C. Cao, H. M. Noh, B. K. Moon, B. C. Choi, J. H. Jeong, Synthesis and optical properties of Ce^{3+}/Tb^{3+} doped LaF_3, $KGdF_4$, and KYF_4 nanocrystals, J. Lumin. 152 (2014) 206–209. https://doi.org/10.1016/j.jlumin.2013.10.054.

[113] S. Das, A. Amarnath Reddy, S. Ahmad, R. Nagarajan, G. Vijaya Prakash, Synthesis and optical characterization of strong red light emitting $KLaF_4:Eu^{3+}$ nanophosphors, Chem. Phys. Lett. 508 (2011) 117–120. https://doi.org/10.1016/j.cplett.2011.04.029.

[114] S. Ahmad, S. Das, R. Nagarajan, G. Vijaya Prakash, Optical properties of Tb^{3+} doped $KLaF_4$ in cubic and hexagonal symmetries, Opt. Mater. 36 (2013) 396–401. https://doi.org/10.1016/j.optmat.2013.09.031.

[115] H. Huang, T. Wang, H. Zhou, D. Huang, Y. Wu, G. Zhou, J. Hu, J. Zhan, Luminescence, energy transfer, and up-conversion mechanisms of $Yb^{3+}$and Tb^{3+}co-doped $LaNbO_4$, J. Alloys Compd. 702 (2017) 209–215. https://doi.org/10.1016/j.jallcom.2017.01.246.

[116] M. Puchalska, E. Zych, M. Sobczyk, A. Watras, P. Deren, Cooperative energy transfer in Yb^{3+}-Tb^{3+} co-doped $CaAl_4O_7$ upconverting phosphor, Mater. Chem. Phys. 156 (2015) 220–226. https://doi.org/10.1016/j.matchemphys.2015.03.004.

[117] A. Bahadur, R.S. Yadav, R. V. Yadav, S.B. Rai, Multimodal emissions from Tb^{3+}/Yb^{3+}co-doped lithium borate glass: Upconversion, downshifting and quantum cutting, J. Solid State Chem. 246 (2017) 81–86. https://doi.org/10.1016/j.jssc.2016.11.004.

[118] S. Das, A.A. Reddy, G.V. Prakash, Strong green upconversion emission from Er^3 –Yb^{3+} co-doped $KCaBO_3$ phosphor, Chem. Phys. Lett. 504 (2011) 206–210. https://doi.org/10.1016/j.cplett.2011.02.004.

[119] R. Reisfeld, C.K. Jørgensen, Lasers and Excited States of Rare Earths, Springer Verlag

Berlin Heidelberg, 1977. https://doi.org/10.1007/978-3-642-66696-4.

[120] S. Shionoya, W.M. Yen, H. Yamamoto, Phosphor Handbook, CRC Press, Taylor and Francis Group, 2007.

[121] S. Hu, X. Wu, Z. Chen, P. Hu, H. Yan, Z. Tang, Z. Xi, Y. Liu, Uniform $NaLuF_4$ nanoparticles with strong upconversion luminescence for background-free imaging of plant cells and ultralow power detecting of trace organic dyes, Mater. Res. Bull. 73 (2016) 6–13. https://doi.org/10.1016/j.materresbull.2015.08.020.

[122] J. Liu, X. Tian, H. Chen, Y. Shao, G. Yang, D. Chen, Near-infrared to visible and near-infrared upconversion of monoclinic $Gd_2O_3:Yb^{3+}/Tm^{3+}$ nanoparticles prepared by laser ablation in liquid for fluorescence imaging, Appl. Surf. Sci. 348 (2015) 60–65. https://doi.org/10.1016/j.apsusc.2014.11.105.

[123] X. Zhai, P. Lei, P. Zhang, Z. Wang, S. Song, X. Xu, X. Liu, J. Feng, H. Zhang, Growth of lanthanide-doped $LiGdF_4$ nanoparticles induced by $LiLuF_4$ core as tri-modal imaging bioprobes, Biomaterials. 65 (2015) 115–123. https://doi.org/10.1016/j.biomaterials.2015.06.023.

[124] R. Lv, P. Yang, F. He, S. Gai, G. Yang, Y. Dai, Z. Hou, J. Lin, An imaging-guided platform for synergistic photodynamic/photothermal/chemo-therapy with pH/temperature-responsive drug release, Biomaterials. 63 (2015) 115–127. https://doi.org/10.1016/j.biomaterials.2015.05.016.

[125] L.C. Ong, L.Y. Ang, S. Alonso, Y. Zhang, Bacterial imaging with photostable upconversion fluorescent nanoparticles, Biomaterials. 35 (2014) 2987–2998. https://doi.org/10.1016/j.biomaterials.2013.12.060.

[126] T. Cao, Y. Yang, Y. Sun, Y. Wu, Y. Gao, W. Feng, F. Li, Biodistribution of sub-10nm

PEG-modified radioactive/upconversion nanoparticles, Biomaterials. 34 (2013) 7127–7134. https://doi.org/10.1016/j.biomaterials.2013.05.028.

[127] N. Wartenberg, P. Fries, O. Raccurt, A. Guillermo, D. Imbert, M. Mazzanti, A gadolinium complex confined in silica nanoparticles as a highly efficient T1/T2 MRI contrast agent, Chem. Eur. 19 (2013) 6980–6983. https://doi.org/10.1002/chem.201300635.

[128] J.Y. Park, M.J. Baek, E.S. Choi, S. Woo, J.H. Kim, T.J. Kim, J.C. Jung, S. Chae, Y. Chang, G.H. Lee, Paramagnetic ultrasmall gadolinium oxide Nanoparticles as advanced T1 MRI contrast agent: account for longitudnal relaxivity, optimal particle diameter and in vivo T1 MR images, ACS Nano. 3 (2009) 3663–3669.

[129] L. Moriggi, C. Cannizzo, E. Dumas, C.R. Mayer, A. Ulianov, L. Helm, Gold nanoparticles functionalized with gadolinium chelates as high-relaxivity MRI contrast agents, J. Am. Chem. Soc. 131 (2009) 10828–10829. https://doi.org/10.1021/ja904094t.

[130] F. Chen, W. Bu, S. Zhang, X. Liu, J. Liu, H. Xing, Q. Xiao, L. Zhou, W. Peng, L. Wang, J. Shi, Positive and negative lattice shielding effects Co-existing in Gd (III) ion doped bifunctional upconversion nanoprobes, Adv. Funct. Mater. 21 (2011) 4285–4294. https://doi.org/10.1002/adfm.201101663.

[131] D. Zhu, F. Liu, L. Ma, D. Liu, Z. Wang, Nanoparticle-based systems for T1-weighted magnetic resonance imaging contrast agents, Int. J. Mol. Sci. 14 (2013) 10591–10607. https://doi.org/10.3390/ijms140510591.

1.10 [132] Y. Deng, H. Wang, W. Gu, S. Li, N. Xiao, C. Shao, Ho^{3+} doped $NaGdF_4$ nanoparticles as MRI/optical probes for brain glioma imaging, J. Mater. Chem. B 2 (2014) 1521–1529. https://doi.org/10.1039/c3tb21613f.

[133] N.J.J. Johnson, W. Oakden, G.J. Stanisz, R.S. Prosser, F.C.J.M. Van Veggel, Size-Tunable , Ultrasmall $NaGdF_4$ Nanoparticles : Insights into Their T1 MRI Contrast Enhancement, Chem. Mater. 23 (2011) 3714–3722.

[134] F. Li, C. Li, X. Liu, Y. Chen, T. Bai, L. Wang, Z. Shi, S. Feng, Hydrophilic, upconverting, multicolor, lanthanide-doped $NaGdF_4$ nanocrystals as potential multifunctional bioprobes, Chemistry. 18 (2012) 11641–11646. https://doi.org/10.1002/chem.201201309.

[135] H.T. Wong, M.K. Tsang, C.F. Chan, K.L. Wong, B. Fei, J. Hao, In vitro cell imaging using multifunctional small sized $KGdF_4:Yb^{3+},Er^{3+}$ upconverting nanoparticles synthesized by a one-pot solvothermal process, Nanoscale. 5 (2013) 3465–3473. https://doi.org/10.1039/c3nr00081h.

[136] L. Wang, Y. Li, $Na(Y_{1.5}Na_{0.5})F_6$ Single-Crystal Nanorods as Multicolor Luminescent Materials, Nano Lett. 6 (2006) 1645–1649. https://doi.org/10.1021/nl060684u.

[137] D. Han, Y. Yang, F. Gu, Z. Wang, Tuning the morphology and upconversion fluorescence of CeO_2:Er/Yb nano-octahedra, J. Alloys Compd. 656 (2016) 524–529. https://doi.org/10.1016/j.jallcom.2015.10.002.

[138] Y. Zhang, L. Yao, D. Xu, H. Lin, S. Yang, Controlled synthesis and luminescence properties of β-$NaGdF_4:Yb^{3+}$, Er^{3+} upconversion nanoparticles, J. Cryst. Growth. 491 (2018) 116–119. https://doi.org/10.1016/j.jcrysgro.2018.03.042.

[139] C. Joshi, K. Kumar, S.B. Rai, Upconversion and anomalous power dependence in $Ca_{12}Al_{14}O_{33}$: Er^{3+}/Yb^{3+} single phase nanophosphor, J. Appl. Phys. 105 (2009) 1–8. https://doi.org/10.1063/1.3148294.

[140] X. Qiu, T. Lin, Multicolor Emission Tuning and Red / Green Ratio Enhancement of

Yb^{3+}/ Er^{3+} Codoped $KGdF_4$ Upconversion Nanoparticles, J. Nanomater. 2015 (2015) 361957.

[141] M. Su, Y. Zhou, K. Wang, D. Huang, W. Xu, Y. Cao, Effect of Yb^{3+} concentration on upconversion luminescence of AlON:Er^{3+} phosphors, J. Rare Earths. 33 (2015) 227–230. https://doi.org/10.1016/S1002-0721(14)60407-5.

[142] Q. Cheng, J. Sui, W. Cai, Enhanced upconversion emission in Yb^{3+} and Er^{3+} codoped $NaGdF_4$ nanocrystals by introducing Li^+ ions, Nanoscale. 4 (2012) 779–784. https://doi.org/10.1039/C1NR11365H.

[143] W. Yu, W. Xu, H. Song, S. Zhang, Temperature-dependent upconversion luminescence and dynamics of $NaYF_4$:Yb^{3+}/Er^{3+} nanocrystals: Influence of particle size and crystalline phase, Dalt. Trans. 43 (2014) 6139–6147. https://doi.org/10.1039/c3dt53562b.

[144] P. Ramasamy, P. Chandra, S.W. Rhee, J. Kim, Enhanced upconversion luminescence in $NaGdF_4$:Yb,Er nanocrystals by Fe^{3+} doping and their application in bioimaging, Nanoscale. 5 (2013) 8711–8717. https://doi.org/10.1039/c3nr01608k.

[145] M. Pollnau , H.U. Gudel, D.R. Gamelin, S.R. Luthi, M.P. Hehlen, Power dependence of upconversion luminescence in lanthanide and transition-metal-ion systems , Phys. Rev. B 61 (2000) 3337-3346.

[146] S. Kaur, A.S. Rao, M. Jayasimhadri, Spectroscopic and photoluminescence characteristics of Sm^{3+} doped calcium aluminozincate phosphor for applications in w-LED, Ceram. Int. 43 (2017) 7401–7407. https://doi.org/10.1016/j.ceramint.2017.02.129.

[147] N. Deopa, A.S. Rao, Spectroscopic studies of Sm^{3+} ions activated lithium lead alumino

borate glasses for visible luminescent device applications, Opt. Mater. 72 (2017) 31–39. https://doi.org/10.1016/j.optmat.2017.04.067.

[148] V. Uma, M. Vijayakumar, K. Marimuthu, G. Muralidharan, Luminescence and energy transfer studies on Sm^{3+}/ Tb^{3+} codoped telluroborate glasses for WLED applications, J. Mol. Struct. 1151 (2018) 266–276. https://doi.org/10.1016/j.molstruc.2017.09.053.

[149] A.S. Kumar, R.A. Kumar, R. Ranjan, Synthesis and optical characterization of Tm^{3+} doped $CaAl_4O_7$ for near – UV LED – based white light, J. Lumin. 182 (2017) 130–136. https://doi.org/10.1016/j.jlumin.2016.10.019.

[150] M. Vijayakumar, K. Marimuthu, Tailoring the luminescence of Eu^{3+} co-doped Dy^{3+} incorporated alumino fluoro-borophosphate glasses for white light applications, J. Lumin. 178 (2016) 414–424. https://doi.org/10.1016/j.jlumin.2016.06.016.

[151] S.P. Tiwari, M.K. Mahata, K. Kumar, V.K. Rai, Enhanced temperature sensing response of upconversion luminescence in ZnO-$CaTiO_3$: Er^{3+}/Yb^{3+} nano-composite phosphor, Spectrochim. Acta A 150 (2015) 623–630. https://doi.org/10.1016/j.saa.2015.05.081.

[152] W. Luo, J. Liao, R. Li, X. Chen, Determination of Judd-Ofelt intensity parameters from the excitation spectra for rare-earth doped luminescent materials, Phys. Chem. Chem. Phys. 12 (2010) 3276–3282. https://doi.org/10.1039/b921581f.

[153] L. Aarts, B.M.V.D. Ende, A. Meijerink, Downconversion for solar cells in $NaYF_4$:Er,Yb, J. Appl. Phys. 106 (2009). https://doi.org/10.1063/1.3177257.

[154] V. Singh, G. Sivaramaiah, J.L. Rao, R.S. Kumaran, P.K. Singh, T.S. Kim, L.K. Kim, Luminescence and EPR studies of ultraviolet light emitting $La_2Zr_2O_7$:Gd^{3+} phosphor powder, J Mater Sci: Mater Electron 26 (2015) 5195–5201. https://doi.org/10.1007/s10854-015-3051-y.

[155] V. Singh, G. Sivaramaiah, N. Singh, J.L. Rao, P.K. Singh, M.S. Pathak, D.A. Hakeem, EPR and PL studies on UVB-emitting gadolinium-doped $SrAl_{12}O_{19}$ phosphors, Optik 158 (2018) 1227–1233. https://doi.org/10.1016/j.ijleo.2017.12.185.

[156] V. Singh, G. Sivaramaiah, N. Singh, M.S. Pathak, J.L. Rao, H.D. Jirimali, V. Natarajan, Investigation of ultraviolet emitting Gd doped $Sr_2MgSi_2O_7$ phosphors,Optik 169 (2018) 397–402. https://doi.org/10.1016/j.ijleo.2018.05.036.

[157] S. Tamboli, B. Rajeswari, S.J. Dhoble, Investigation of UV-emitting Gd^{3+} -doped $LiCaBO_3$ phosphor, Luminescence 31 (2016) 551–556. https://doi.org/10.1002/bio.2994.

[158] M. Mohapatra, B. Rajeswari, N.S. Hon, R.M. Kadam, M.S. Keskar, V. Natarajan, An electron spin resonance and photoluminescence investigation of the effect of annealing temperature on Gd-doped $La_2Zr_2O_7$ nano-ceramics, Ceram. Int. 41 (2015) 8761–8767. https://doi.org/10.1016/j.ceramint.2015.03.099.

[159] S. Rada, V. Dan, M. Rada, E. Culea, Gadolinium-environment in borate – tellurate glass ceramics studied by FTIR and EPR spectroscopy, J. Non. Cryst. Solids. 356 (2010) 474–479. https://doi.org/10.1016/j.jnoncrysol.2009.12.011.

[160] L. Sun, R. Wei, J. Feng, H. Zhang, Tailored lanthanide-doped upconversion nanoparticles and their promising bioapplication prospects, Coord. Chem. Rev. 364 (2018) 10–32. https://doi.org/10.1016/j.ccr.2018.03.007.

[161] J. Feng, H. Zhang, Hybrid materials based on lanthanide organic complexes: A review, Chem. Soc. Rev. 42 (2013) 387–410. https://doi.org/10.1039/c2cs35069f.

[162] R. Li, Z. Ji, J. Dong, C.H. Chang, X. Wang, B. Sun, M. Wang, Y.P. Liao, J.I. Zink, A.E. Nel, T. Xia, Enhancing the imaging and biosafety of upconversion nanoparticles through

phosphonate coating, ACS Nano. 9 (2015) 3293–3306. https://doi.org/10.1021/acsnano.5b00439.

[163] J. Zhou, Z. Liu, F. Li, Upconversion nanophosphors for small-animal imaging, Chem. Soc. Rev. 41 (2012) 1323–1349. https://doi.org/10.1039/c1cs15187h.

[164] D. Deng, Y. Chen, J. Cao, J. Tian, Z. Qian, S. Achilefu, Y. Gu, High-quality $CuInS_2$/ZnS quantum dots for in vitro and in vivo bioimaging, Chem. Mater. 24 (2012) 3029–3037. https://doi.org/10.1021/cm3015594.

[165] D.M. Shcherbakova, A.A. Shemetov, A.A. Kaberniuk, V. V. Verkhusha, Natural Photoreceptors as a Source of Fluorescent Proteins, Biosensors, and Optogenetic Tools, Annu. Rev. Biochem. 84 (2015) 519-550 . https://doi.org/10.1146/annurev-biochem-060614-034411.

[166] J. Fan, M. Hu, P. Zhan, X. Peng, Energy transfer cassettes based on organic fluorophores: Construction and applications in ratiometric sensing, Chem. Soc. Rev. 42 (2013) 29–43. https://doi.org/10.1039/c2cs35273g.

[167] D. Jaque, C. Richard, B. Viana, K. Soga, X. Liu, J. G. Solé, Inorganic nanoparticles for optical bioimaging, Adv. Opt. Photonics 8 (2016) 1-103. https://doi.org/10.1364/AOP.8.000001.

[168] F. Cai, D. Wang, M. Zhu, S. He, Pencil-like imaging spectrometer for bio-samples sensing, Biomed. Opt. Express. 8 (2017) 5427. https://doi.org/10.1364/boe.8.005427.

[169] Y. Pu, F. Cai, D. Wang, J.X. Wang, J.F. Chen, Colloidal Synthesis of Semiconductor Quantum Dots toward Large-Scale Production: A Review, Ind. Eng. Chem. Res. 57 (2018) 1790–1802. https://doi.org/10.1021/acs.iecr.7b04836.

[170] J. Shen, T. Zhang, Y. Cai, X. Chen, S. Shang, J. Li, Highly fluorescent N,S-co-doped

carbon dots: Synthesis and multiple applications, New J. Chem. 41 (2017) 11125–11137. https://doi.org/10.1039/c7nj00505a.

[171] J. Qian, Z. Zhu, A. Qin, W. Qin, L. Chu, F. Cai, H. Zhang, Q. Wu, R. Hu, B.Z. Tang, S. He, High-order non-linear optical effects in organic luminogens with aggregation-induced emission, Adv. Mater. 27 (2015) 2332–2339. https://doi.org/10.1002/adma.201500141.

[172] Q. Chen, C. Wang, L. Cheng, W. He, Z. Cheng, Z. Liu, Protein modified upconversion nanoparticles for imaging-guided combined photothermal and photodynamic therapy, Biomaterials. 35 (2014) 2915–2923. https://doi.org/10.1016/j.biomaterials.2013.12.046.

[173] G.K. Das, B.C. Heng, S.C. Ng, T. White, J.S.C. Loo, L. D'Silva, P. Padmanabhan, K.K. Bhakoo, S.T. Selvan, T.T.Y. Tan, Gadolinium oxide ultranarrow nanorods as multimodal contrast agents for optical and magnetic resonance imaging, Langmuir. 26 (2010) 8959–8965. https://doi.org/10.1021/la904751q.

[174] L. Zhou, Z. Gu, X. Liu, W. Yin, G. Tian, L. Yan, S. Jin, W. Ren, G. Xing, W. Li, X. Chang, Z. Hu, Y. Zhao, Size-tunable synthesis of lanthanide-doped Gd_2O_3nanoparticles and their applications for optical and magnetic resonance imaging, J. Mater. Chem. 22 (2012) 966–974. https://doi.org/10.1039/c1jm13758a.

[175] X. Bai, H. Song, G. Pan, Y. Lei, T. Wang, X. Ren, S. Lu, B. Dong, Q. Dai, L. Fan, Size-dependent upconversion luminescence in Er^{3+}/Yb^{3+} -codoped nanocrystalline yttria: Saturation and thermal effects, J. Phys. Chem. C. 111 (2007) 13611–13617. https://doi.org/10.1021/jp070122e.

[176] S.K. Ray, Y.K. Kshetri, T. Yamaguchi, T.H. Kim, S.W. Lee, Characterization and multicolor upconversion emission properties of $BaMoO_4$: Yb^{3+},Ln^{3+}(Ln = Tm, Ho, Tm/Ho) microcrystals, J. Solid State Chem. 272 (2019) 87–95.

https://doi.org/10.1016/j.jssc.2019.01.033.

[177] Q. Nie, X.J. Li, S. Dai, T. Xu, Z. Jin, X. Zhang, Energy transfer and upconversion luminescence in Tm^{3+}/Yb^{3+} co-doped lanthanum-zinc-lead-tellurite glasses, J. Lumin. 128 (2008) 135–141. https://doi.org/10.1016/j.jlumin.2007.06.001.

[178] F. Pandozzi, F. Vetrone, J.C. Boyer, R. Naccache, J.A. Capobianco, A. Speghini, M. Bettinelli, A Spectroscopic Analysis of Blue and Ultraviolet Upconverted Emissions from $Gd_3Ga_5O_{12}:Tm^{3+},Yb^{3+}$ nanocrystals, J. Phys. Chem. B 109 (2005) 17400-17405

[179] M.A. Hassairi, A. G. Hernández, M. Dammak, D. Zambon, G. Chadeyron, R. Mahiou, Tuning white upconversion emission in $GdPO_4$:Er/Yb/Tm phosphors, J. Lumin. 203 (2018) 707–713. https://doi.org/10.1016/j.jlumin.2018.07.024.

[180] S. Hu, X. Wu, Z. Tang, Z. Xi, Z. Chen, P. Hu, Y. Yu, H. Yan, Y. Liu, Upconversion $NaYF_4$ nanoparticles for size dependent cell imaging and concentration dependent detection of rhodamine B, J. Nanomater. 2015 (2015) 598734. https://doi.org/10.1155/2015/598734.

[181] R.S. Yadav, S.J. Dhoble, S.B. Rai, Enhanced photoluminescence in Tm^{3+}, Yb^{3+}, Mg^{2+} tri-doped $ZnWO_4$ phosphor: Three photon upconversion, laser induced optical heating and temperature sensing, Sensor Actuat B Chem. 273 (2018) 1425–1434. https://doi.org/10.1016/j.snb.2018.07.049.

[182] R. Yadav, S.K. Singh, R.K. Verma, S.B. Rai, Observation of multi-mode: Upconversion, downshifting and quantum-cutting emission in Tm^{3+} /Yb^{3+} co-doped Y_2O_3 phosphor, Chem. Phys. Lett. 599 (2014) 122–126. https://doi.org/10.1016/j.cplett.2014.03.025.

[183] V. Singh, G. Sivaramaiah, J.L. Rao, S.H. Kim, Luminescence and electron paramagnetic

resonance investigation on ultraviolet emitting Gd doped $MgAl_2O_4$ phosphors, J. Lumin. 143 (2013) 162–168. https://doi.org/10.1016/j.jlumin.2013.03.054.

[184] V. Singh, S. Kaur, A.S. Rao, N. Singh, M.S. Pathak, J.L. Rao, An Electron Paramagnetic Resonance and Photoluminescence Investigation of UVB Radiation Emitting Gadolinium-Activated $CaY_2Al_4SiO_{12}$ Garnet Compound, J. Electron. Mater. 48 (2019) 4092–4098. https://doi.org/10.1007/s11664-019-07175-w.

[185] V. Singh, G. Sivaramaiah, J.L. Rao, S.H. Kim, Luminescence and EPR studies of Gd^{3+} -activated strong UV-emitting $CaZrO_3$ phosphors prepared via solution combustion method, J. Electron. Mater. 43 (2014) 3486–3492. https://doi.org/10.1007/s11664-014-3091-8.